Scanning Probe Microscopy Investigations of Organic Transistors

Suzanne Thomas

A thesis submitted as partial fulfilment for the degree of
Doctor of Philosophy

School of Physics and Astronomy

September 2019

Abstract

Delays in obtaining medical results from laboratory testing facilities is a well recognised bottleneck in the medical community. Employing methods that utilise real-time electronic sensing could recover this potentially life-saving lost time. Such sensors have many applications within the medical field including detection of infectious diseases, biological or chemical weaponry, glucose sensors for diabetic patients, and many more. However we are approaching a time in human history when antibiotics may no longer be an effective way to treat bacterial infections, and as such we have chosen to pursue a bio-sensing device for antibiotic resistant enzymes.

Due to the rise of antibiotic resistance in so called super-bugs compounded with the well documented medical bottleneck that results in long waiting times for test results, there is a call for real time bio-sensing devices that can detect antibiotic resistance. Presented in this thesis is work towards a real time bio-sensing device designed to detect the enzyme TEM-1 beta-lactamase (TEM-1), an enzyme found in bacteria resistant to beta-lactam based antibiotics.

The work presented here begins from the base of the proposed device up, beginning with electrostatic characterisation and investigations of field-effect transistors (FET). Firstly an exploration of dinaptho[2,3-b:2',3'-f]thieno[3,2-b]thiophene (DNTT) based organic field-effect transistor (OFET) devices using scanning Kelvin probe microscopy (SKPM) to evaluate contact resistance and mobility of three device conformations. Using the skills developed from these experiments, SKPM was further applied to four organic semiconductor (OSC) and polymer blends. Although these devices behaved in a different manner to the DNTT devices, and therefore investigations of contact resistance and mobility were not possible, producing maps

of the magnitude of the gradient of the potential provided insight into the blending of the OSC and polymer in the device channel.

Using the experience gained working with atomic force microscopy (AFM) and SKPM, the second element of the proposed devices was explored. By covalently binding a detector protein to single wall carbon nanotubes (SWCNT), the electrostatics of the two become interlinked, i.e. changes to the protein result in a change to the whole carbon nanotube (CNT)-protein system [1]. This is proposed as the sensing mechanism of the bio-sensor with the FET base allowing measurements of these changes to be recorded. A series of experiments were conducted using various proteins to ensure binding to the carbon nano-materials, as well as monitoring changes in height, and orientation of the bound protein structures.

Finally the work culminates in the production, and preliminary testing, of a prototype bio-sensing device. CNTs were suspended across a nano-gap electrode device. The detector protein BLIP 41 azF was then covalently bound to the carbon nanotubes. Using a four point probe system to monitor changes in electrical characteristics, the analyte protein, TEM-1, was drop-cast onto the sensing device. While these tests proved inconclusive at this time it is hoped that further work will yield meaningful results.

Acknowledgements

What an adventure these past years have been. I have so many people to thank for keeping me going throughout. Thank you to my supervisors Martin Elliott, Emyr Macdonald, and Dafydd Jones. Your support and willingness to meet for a chat at anytime was a true asset to my work and I can wholeheartedly say that you made my PhD an enjoyable experience throughout.

Thank you to the EPSRC for the opportunity to undertake this PhD. A huge thanks to all of my collaborators. Dr Chang-Hyun Kim, for his patience when things went wrong, all of the bio-sciences, and pharmacy team, as well as the happy gents in the biological scanning labs. The support I have received from you all has been fantastic. I would also like to thank my collaborators from Imperial college London: for supplying the OTFT devices and helping de-mystify the results, as well as the group of Dr Matteo Palma: for supplying the carbon nanotube gated electrodes for bio-sensing.

To my partner Owain, thank you. You have been my rock during these past few years, despite temper tantrums, tears, and fears, you have stuck by me. I would have quit in the first few months had it not been for your love and support. I finally have a higher qualification than you! I hope you one up me soon, so we can be Drs together.

Sara-Jayne Gillgrass, what can I say. You are quite possibly the best pal a girl could wish for. Thank you for the coffee runs, the ranting, and all the vegan snacks! You made coming to work a delight. I will miss our chats, you are one in a million.

Adam Beachey, another top banana. Thank you for being an excellent lab buddy! Playing catch when we had no lab work to do, watching terrible Youtube videos over lunch (memories of which will haunt me forever), trips to Tesco for a meal deal, lager...cheap. Bro, you were an excellent bro.

There are so many others I need to thank, so here we go: Beth, Eben, Matt, Dani, the kickboxing girls (thanks for giving me an outlet for my aggression), Alex, Athraa,

Isam, Rangeen, Harley, Rachel, Andriy, Becki, Ben, Dave. I'm sure I have missed a few of you, but there is limited space and I am, at heart, lazy.

Finally, none of this would have been possible without the support of my wonderful family. Mum, thank you for always being there to hug, and provide cooking tips at anytime of day. I ring, you are always there. Your support has kept me strong my entire life, you are my rock. Dad, thank you for your endless financial advice. I may not read every money saving article you send me, but I appreciate the effort. You and Mum may not understand a word I am saying when I talk about my work, but you always ask how I am doing. I know how proud you are of me, mostly because you tell anyone who will listen. Rebecca, thank you for being an excellent sister! I hope to make the acknowledgements of your dissertation soon.

One last acknowledgement: to my cat - Poppy. Thank you for making typing this thesis so difficult, my keyboard must be very comfy.

List of Publications

Chang-Hyun Kim, Suzanne Thomas, Ji Hwan Kim, Martin Elliott, Emyr Macdonald, Myung-Han Yoon, *"Potentiometric Parameterization of Dinaptho[2,3-b:2',3'-f]thieno[3,2-b]thiophene Field-Effect Transistors with a Varying Degree of Nonidealities"*, Adv. Electron. Mater., 2018, 4, 1700514.

Athraa Zaki, Andrew M. Hartley, Samuel C. Reddington, Suzanne Thomas, Peter Watson, Antony J. Hayes, Andy V. Moskalenko, Monica F. Craciun, Emyr Macdonald, D. Dafydd Jones, Martin Elliott, *"Defined covalent assembly of protein molecules on graphene using a genetically encoded photochemical reaction handle"*, RSC Adv., 2018, 8, 5768-5775.

Suzanne K. Thomas, W. David Jamieson, Rebecca E. A. Gwyther, Benjamin J. Bowen, Adam Beachey, Harley L. Worthy, J. Emyr Macdonald, Martin Elliott, Oliver K. Castell, D. Dafydd Jones *"Site-Specific Protein Covalent Attachment to Nanotubes and Its Electronic Impact on Single Molecule Function"*, Bioconjugate Chem., 2019, 10.1021/acs.bioconjchem.9b00719.

Contents

List of Figures

Abbreviations	
AFM	Atomic force microscopy
SKPM	Scanning Kelvin probe microscopy
EFM	Electrostatic force microscopy
TIRFM	Total internal reflection fluorescence spectroscopy
SPM	Scanning probe microscopy
PSD	Position sensitive detector
OSC	Organic semiconductor
OFET	Organic field-effect transistor
OTFT	Organic thin-film transistor
FET	Field-effect transistor
TC	Top contact
BC	Bottom contact
BC-SAM	Bottom contact with self-assembled monolayer
HOMO	Highest occupied molecular orbit
LUMO	Lowest unoccupied molecular orbit
CPD	Contact potential difference
DNTT	dinaptho[2,3-b:2',3'-f]thieno[3,2-b]thiophene
PMMA	Poly(methyl methacrylate)
diF-TES-ADT	2,8-difluoro-5,11-bis(triethylsilylethynyl)anthradithiophene
PTAA	poly(triarylamine)
C_8-BTBT	2,7-dioctyl[1]-benzothieno3,2-b][1]benzothiophene
C_{16}IDT-BT	indacenodithiophene-benzothiadiazole
BCF	Tris(pentafluorophenyl)borane
PFBT	pentafluorobenzene thiol
Pt-Ir	Platinum Iridium
HOPG	Highly ordered pyrolytic graphite
SLG	Single layer graphene
FLG	Few layer graphene
CNT	carbon nanotube
SWCNT	Single wall carbon nanotube
sSWCNT	Semiconducting single wall carbon nanotube
CVD	Chemical vapour deposition
GIST	Gwangju Institute of Science and Technology
QMUL	Queen Mary University London
UHV	Ultrahigh vacuum
ROI	Region of interest
UV	Ultraviolet
LED	Light emitting diode
DI	de-ionised
ncAA	Non-canonical amino acid
azF	*p*-azido-L-phenylalanine
RNA	Ribonucleic acid
SDS	Sodium dodecyl sulfate
DTT	Dithiothreitol

Chapter 1

Introduction

1.1 Motivations

Development of high speed analytic devices for bio-sensing applications is desirable in the medical community, especially devices that can provide real time detection events [2, 3, 4, 5]. At present, for many laboratory procedures in medicine, it can take weeks to obtain results for potentially life threatening illnesses. This is a well recognised bottleneck in the medical field. One such area where real time detection would be particularly important is the rapidly increasing threat of antibiotic resistance [6, 7, 8, 9]. Antibiotics allow us to safely perform complex operations, replace organs and limbs, provide adequate food for a fast growing population, and sustain an ageing one. The rise in antibiotic resistance in bacteria threatens all of this, if our bodies cannot be assisted in fighting off these super-bugs, a simple scratch could become fatal. The rise in these so called super-bugs can be attributed in part to the overuse of antibiotics in not only human patients but in livestock as well [10]. Although cutting back on prescriptions of antibiotics to human patients will assist in slowing down the development of these super-bugs, it is necessary to develop methods to rapidly, and in real time, detect when a bacterium will be resistant to beta-lactam based antibiotics (the most commonly used antibiotics [11]) and when a more targeted and aggressive strategy is required.

The protein that is key to this mechanism is TEM-1 [12, 13], which binds to beta-lactamase-inhibitor proteins (BLIPs): more information on this mechanism can be found in section 3.4.3. The base of the proposed real time bio-sensing device is a field effect transistor (FET) device, with carbon nanotubes forming the channel. The detector protein, when covalently bound to the carbon nanotubes, will create a change in electrical characteristics of the device [14]. Similarly when the analyte is introduced to the system the binding of analyte to the bound detector protein will also create a measurable change to the electrical characteristics of the device [15].

To reach the project goal, investigations of FETs to examine methods for scanning and detecting analyte binding were performed. Firstly two types of organic FETs (OFETs) were investigated in order to obtain a broad overview of device treatment and scanning methods. These OFETs also allowed for investigation into contact resistance, channel mobility, and physical device conformation. Another step towards achieving a functioning bio-sensing device was to image proteins bound to carbon nano-structures. This allowed for the limitations of scanning and imaging methods to be probed, as well as the limitations and exploitable mechanisms of depositing proteins to bind to the nano-materials. The final step is to put this knowledge together, using a carbon nanotube based FET functionalised with covalently bound BLIP-II to detect the TEM-1 analyte.

1.2 Thesis outline

The second chapter outlines the experimental scanning techniques used. These methods can be separated into two categories: scanning probe microscopy methods (SPM), and the optical microscopy methods used to investigate fluorescence. SPM was widely used throughout this work, with atomic force microscopy (AFM) and scanning Kelvin probe microscopy (SKPM) playing the largest role. Another SPM method used to a lesser extent in this work is EFM-Phase. Each of these methods is powerful in its own way allowing the production of various data types for the characterisation of nano-materials. AFM produces topographical data, allowing an image to be built of the sample structure at the micro and nano-meter scale, as

well as phase shift data which is particularly useful for distinguishing soft proteins from hard carbon nano-structures. SKPM produces potential maps of the sample which allows for the investigation of local potential profiles for a sample. SKPM however has poor spatial resolution and as such a method to improve the image resolution whilst still recovering potential data was developed. This method uses adapted software to apply an AC bias to the tip in lift mode of scanning and was given the name EFM-Phase. This approach was found to be of limited usefulness for this project and hence it features only minimally. The second class of methods were the microscopy techniques used to image and characterise fluorescent proteins, specifically green fluorescent proteins (GFP), which act as an excellent base point for protein imaging. GFP has several benefits: it is robust, stable in ambient conditions, well documented, and easy to visualise. The first of these techniques is confocal microscopy which was employed for samples on an opaque background, specifically graphene on silicon. The second technique was total internal reflection fluorescence microscopy (TIRFM), which was utilised for samples on glass cover-slips, namely carbon nanotubes drop cast and dried onto the slip.

The third chapter presents the general background theory necessary for the experiments within. This chapter is comprised of a brief introduction to the materials used including: proteins, carbon nano-structures, and organic semiconducting materials. The chapter then moves on to introduce the fundamentals of FETs, followed by OFETs and finally carbon nano-material based FETs with specific attention given to the role of these devices in a sensing mechanism. Finally the mechanics and physics of contact resistance in OFETs, which has been extensively investigated, are introduced. It is hoped that this chapter should provide the reader with all the necessary background information to fully comprehend the work set out in this thesis.

The fourth chapter of this work contains the investigations into OFET devices. The work begins with the study of dinaptho[2,3-b:2',3'-f]thieno[3,2-b]thiophene (DNTT), as the thin film channel material for the first set of devices. The study aims to investigate the correlation between the physical device configuration with contact resistance and, as a consequence, charge carrier mobility. This was experimentally

performed by taking three distinct device configurations: top contact bottom gate (TC), bottom contact bottom gate (BC), and bottom contact bottom gate with a self-assembled monolayer (BC-SAM) and performing SKPM measurements across varied gate and source-drain biases. It was found that for the BC and BC-SAM devices the thin film growth resulted in defects forming in the channel material, a study of these defects was performed to investigate what effect the addition of the SAM resulted in. Parameter extraction using linear and saturation regime transfer data provided by Dr Chang-Hyun Kim in conjunction with SKPM data allowed the investigation of contact resistance in the three device configurations as well as a comparison of mobility not only across the three devices, but also the methods by which charge carrier mobility is calculated.

Chapter 4 continues with the second set of OFET devices. Whereas the DNTT transistors were purely organic semiconductor (OSC) based channel material, here two OSC:polymer blends are studied. Each blend has a pristine and a doped sample variant and the effect of the dopant on the material and device potential is studied. The same methods used for the DNTT transistors were not useful here and as such alternative methods of investigation were developed, namely using the magnitude of the gradient of the potential data from SKPM methods to produce a map of the sample and its local potential gradients. This proved particularly useful to visualise the blended channel material and the effect this had on channel resistance.

The investigation of potential data for various samples continues in chapter five where a higher resolution scanning technique for electrostatic measurements is presented. Throughout this chapter the investigation of various samples using this method are presented, but ultimately the arduous data recovery process and lack of reproducible results led to this method being discarded for the purview of this work.

Following this setback, in chapter six it was determined that efforts were better spent investigating protein binding to carbon nano-structures. This chapter begins with the investigation into the retained activity of GFP bound to graphene and carbon nanotubes using confocal and TIRF microscopy methods, this section is brief as it is based upon the work performed by other group members towards

the same goal and is not the main focus of this work. The next section outlines the effectiveness of AFM for the determination of changes to carbon nanotube bound proteins in which dimer proteins are chemically broken to form monomers and the change in height is measured. The work continues with GFP modified with the photo-chemical reaction handle responsible for binding to carbon nano-structures in various positions about the protein. This enables a comprehensive study of the use of AFM to determine protein orientation. Finally the BLIP is investigated, using AFM methods to determine initial binding to carbon nanotubes as well as the addition of the analyte TEM-1. A brief first study into the result of BLIP binding to carbon nanotubes on a carbon nanotube based FET, and the subsequent addition of the analyte protein, were performed using a probe station to obtain electrical measurements.

The final chapter of this work outlines the conclusions drawn from the studies within and the future work that may be undertaken.

Chapter 2

Experimental techniques

2.1 Introduction

In this chapter the experimental methods used within this thesis are introduced. The chapter begins with a brief outline of scanning probe microscopy methods including atomic force microscopy (AFM), scanning Kelvin probe microscopy (SKPM) and EFM-Phase methods. Both AFM and SKPM are used extensively within this work whereas EFM-phase methods are explored for experimental investigation, but were ultimately replaced by one or both of the other techniques. The chapter then continues on to introduce confocal microscopy and total internal reflection fluorescence microscopy (TIRFM) methods which are used to observe the fluorescent behaviour of the green fluorescent protein (GFP) covalently bound to carbon nanostructure substrates.

2.2 Scanning probe microscopy methods

2.2.1 Atomic force microscopy

Atomic force microscopy (AFM) is one of the most widely used techniques for observation and analysis of device topography. First developed in 1985 by Binnig, Quate

and Gerber[16]; AFM allows for the visualisation and characterisation of structures from the order of hundreds of micrometers down to angstroms in size as, although the lateral resolution of the AFM is poor ($\approx$ 30 nm) due to convolution, the vertical resolution is excellent (up to 0.1 nm) [17].

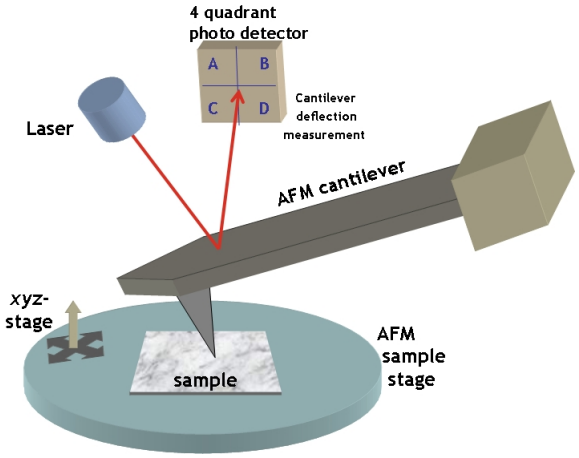

Figure 2.1: A representation of the experimental components and set up for atomic force microscopy scanning methods. [18]

The mechanics behind this powerful technique are relatively simple in design, a representation of which can be found in figure 2.1. An atomically sharp cantilever, usually micro-fabricated from Si or Si_3N_4 [19, 20, 21], is mounted into a specially designed holder such that the end of the cantilever, on which the sharp tip resides, can bend freely. The tip is brought into contact with the target surface using piezo-ceramic micro-manipulators allowing the tip-surface distance to be controlled with high precision. Once the tip has been engaged with the surface of the sample, it will begin scanning in a raster pattern, with successive lines referred to as trace and retrace scans[22].

In ambient conditions, the most widely used AFM technique is intermittent contact mode (also known as tapping mode) which minimises surface deformations caused by the tip in comparison to contact mode AFM. In intermittent contact mode the cantilever is driven to oscillate at close to its resonant frequency. As the tip comes into contact with the surface, interaction forces such as Van der Waals, electrostatic forces, and dipole-dipole interactions change the oscillation amplitude of the tip. A feedback loop is employed to adjust the height of the tip to keep the oscillation amplitude of the cantilever at a constant level during scanning. A large

oscillation amplitude is applied to the cantilever and as such the probe moves from being far from the surface (where there is no tip-sample interaction), through the attractive regime, into the repulsive regime and back, for each oscillation cycle [23, 24], this is shown in figure 2.2.

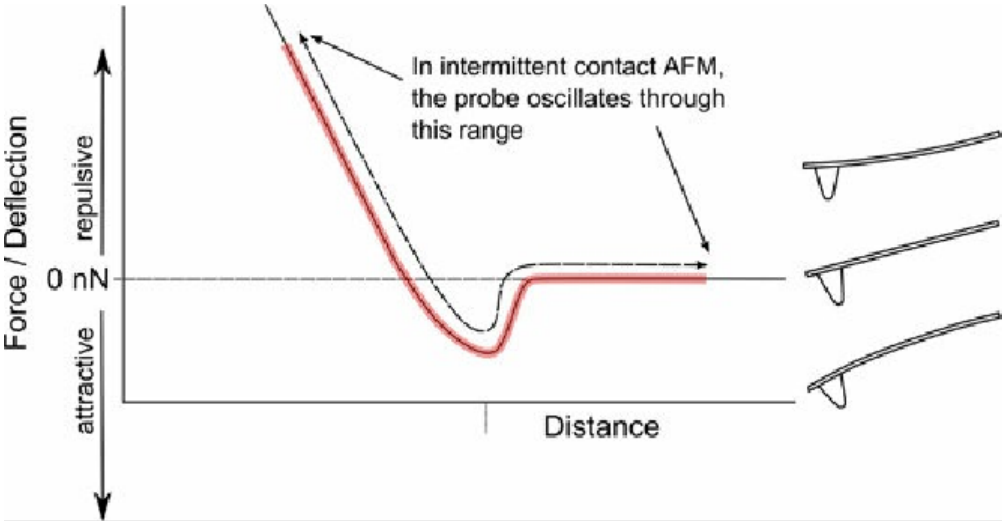

Figure 2.2: Intermittent contact operating regime. In this mode, the AFM probe's oscillation is large enough to move from the repulsive regime, through the attractive regime, and completely out of contact in each cycle. [23]

To produce an image from the collected data, a system must be in place to track the probe as it scans the sample surface. In the case of AFM an optical detection system is usually employed consisting of a laser beam that is focused onto the visible face of the cantilever which is coated with a reflective substance such as aluminium or gold. The laser light is reflected from the cantilever and onto a four-quadrant position-sensitive detector (PSD), which allows for tracking of the lateral and vertical motions of the probe during scanning. To ensure accurate measurements of cantilever deflections, the system requires both precise calibration of the aforementioned feedback loop as well as ensuring that the reflected laser beam is centred on the four-segment PSD (2.1) before scanning is initiated.

The phase shift between the tip response and the driving AC signal can also be mapped as well as the aforementioned topographical data. In tapping mode this data is acquired when the cantilever, given a particular drive frequency and drive amplitude, experiences a reduction in oscillation amplitude as is shown in figure 2.3. By analysing the phase shift in conjunction with the surface topography we can

gain valuable insight into the mechanical properties of the scanned region. This is especially useful for work involving biological samples mounted onto solid substrates (such as gold, graphene, silicon etc.) where the contrast in mechanical properties between sample and substrate can be greater than the contrast in height[25].

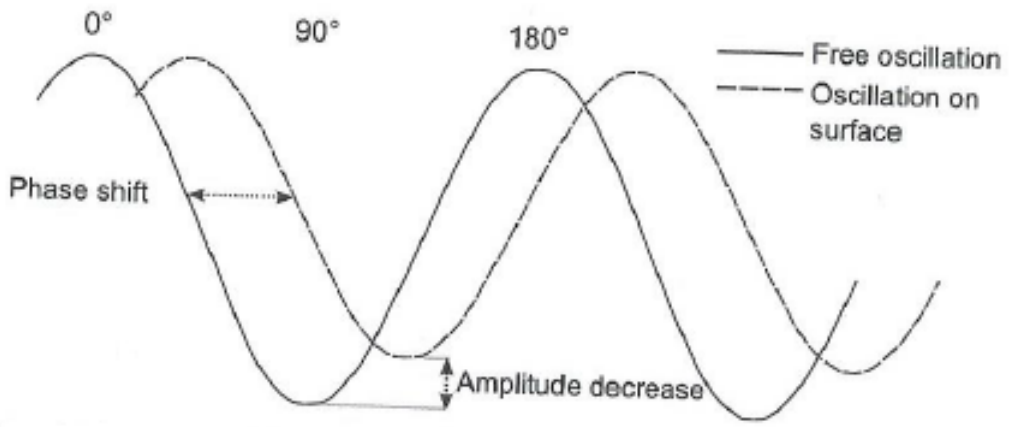

Figure 2.3: Illustration of the effect of intermittent contact on the cantilevers' oscillation. The free oscillation (solid) is modified when in contact with a surface (dashed) by a reduction in amplitude and a phase shift. [23]

There are some disadvantages to the intermittent contact method however. The tip is easily contaminated during scanning, particularly when scanning organic material or CNT's, where the tip can 'catch' on some of the material which presents as irregularities in images. This method is also unsuitable for surfaces that are not flat, i.e if the sample has a macroscopic tilt, as the piezoelectric ceramic cannot extend or retract the tip enough to keep in contact with the sample surface. Thus the sample must be mounted in such a way as to be as macroscopically flat as possible. Similar to the previous issue, AFM is unsuitable for imaging steep overhangs present on samples for the same reason, that the piezoelectric component controlling the retraction and extension of the tip has a limited range of motion.

2.2.2 Scanning Kelvin probe microscopy

Scanning Kelvin probe microscopy (SKPM), also known as surface potential microscopy, is a modified form of the AFM technique. SKPM also employs an oscillat-

ing cantilever whose movement across a sample surface is controlled via a feedback loop. Intermittent contact mode AFM is sensitive to local short-range van der Waals forces and measures the cantilever response to the local height of the surface. Whereas SKPM involves electrostatic interactions, which are long range, and measures changes in the local work function. These longer-range interactions are responsible for the poorer spatial resolution observed in SKPM however, it is difficult to avoid interactions between the surface region of the sample and the whole cantilever. SKPM methods require the use of specialised conducting metal tips, most commonly: platinum-iridium (Pt-Ir) tips which increases the conductivity of the cantilever tip, as well as requiring the sample surface to be conducting.

The operating methods of SKPM can be seen as AFM with two additional line scans. For intermittent contact mode AFM, the cantilever will make only two passes across the sample surface, a trace and a retrace, on the same line. To image the difference in surface potential, the tip must make four passes. Two of the line scans are identical to that of AFM methods (a trace and retrace completed in intermittent contact mode producing surface topography information), whereas the second pair of lines are performed with the tip lifted to a user-defined distance to avoid the van der Waals forces between tip and sample as shown in figure 2.4.

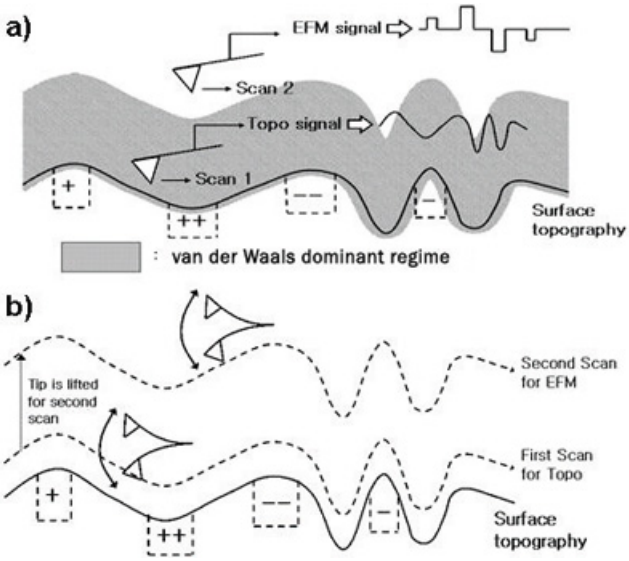

Figure 2.4: A depiction of tip lifting to escape Van der Waals dominant regime. [26]

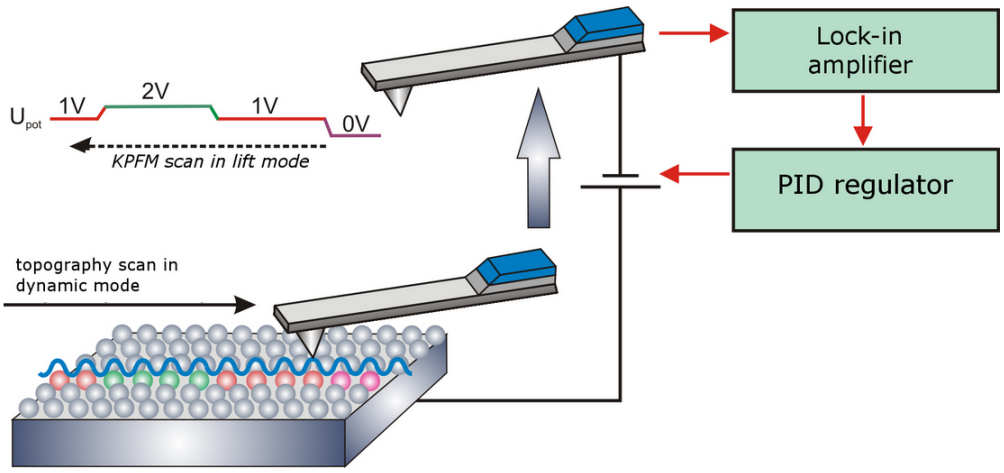

Figure 2.5: A depiction of the tip entering lift mode and scanning a sample comprised of two different materials (red and green). [27]

Since both the tip and the sample are conductive, electrons will flow to the highest work function material from the lowest until the Fermi levels coincide. The potential that is generated between the two conducting materials is known as the contact potential difference (CPD) which is equivalent to the difference in work function between the tip (ϕ_{tip}) and (ϕ_{sample}).

The CPD between the tip and the sample is defined as

$$V_{CPD} = \frac{\phi_{tip} - \phi_{sample}}{\mid e \mid} \tag{2.1}$$

where e is the electronic charge and assuming that the bias is applied to the tip and not the sample[28].

The electrostatic force between tip and sample is given as:

$$F_{el}(z) = \frac{1}{2}\frac{\partial C(z)}{\partial z}(\Delta V)^2 \tag{2.2}$$

F_{el} is the electrostatic force, ΔV is the potential difference between V_{tip} and V_{CPD}, z is the relative separation and C is the local capacitance.

In SKPM measurements, tip bias is varied such that F_{el} (z) = 0 which leads to $\Delta V = 0$ and as such $V_{tip} = V_{CPD}$. This condition allows for direct measurement of sample surface potential from tip bias.

When a bias $V_{tip} = V_{AC}\ \sin(\omega t) + V_{DC}$ is applied to the tip

$$\Delta V = V_{tip} - V_{CPD} = (V_{DC} - V_{CPD}) + V_{AC}\ \sin(\omega t) \tag{2.3}$$

where V_{DC} and V_{AC} are externally applied DC and AC voltage respectively. By combining equation 2.2 and 2.3

$$F_{el}(z) = \frac{1}{2}\frac{\partial C(z)}{\partial z}[(V_{DC} - V_{CPD}) + V_{AC}\ sin(\omega t)]^2. \tag{2.4}$$

This equation can be split into three parts.

$$F_{el}(z) = \underbrace{\frac{\partial C(z)}{\partial z}\frac{1}{2}(V_{DC} - V_{CPD})^2}_{\text{DC term}} + \underbrace{\frac{\partial C(z)}{\partial z}(V_{DC} - V_{CPD})V_{AC}\ \sin(\omega t)}_{\omega \text{ term}} + \underbrace{\frac{\partial C(z)}{\partial z}\frac{V_{AC}^2}{4}\ \cos(2\omega t)}_{2\omega \text{ term}}. \tag{2.5}$$

In equation 2.5, the DC term results in a static deflection of the tip. The ω term is used to measure the CPD and the 2ω term is useful in capacitance microscopy.

We also have the gradient of the electrostatic force, given by the equation

$$F'_{el}(z) = \frac{\partial F_{el}(z)}{\partial z} \tag{2.6}$$

and hence

$$F'_{el}(z) = \underbrace{\frac{\partial^2 C(z)}{\partial z^2}\frac{1}{2}(V_{DC} - V_{CPD})^2}_{\text{DC term}} + \underbrace{\frac{\partial^2 C(z)}{\partial z^2}(V_{DC} - V_{CPD})V_{AC}\ \sin(\omega t)}_{\omega \text{ term}} + \underbrace{\frac{\partial^2 C(z)}{\partial z^2}\frac{V_{AC}^2}{4}\ \cos(2\omega t)}_{2\omega \text{ term}}. \tag{2.7}$$

Due to the electrical forces applied to the tip, oscillations additional to the mechanical oscillations will be present. Therefore, a lock-in amplifier is integrated into the system to measure V_{CPD}. This allows the system to extract the electrical force component from the ω term of equation 2.7 as a function of V_{CPD} and V_{AC}. When $V_{DC} = V_{CPD}$ the modulation amplitude of F'_{el}(z) at ω drops to zero. This forms the basis of the feedback loop that is used to control the tip. In the case of SKPM the feedback loop controls the DC bias to set the ω amplitude to zero, the DC bias that is required to null the force is a measure of the sample surface potential. As such the value of V_{DC} is acquired for each point per line scan, which is used to compose

a map of the absolute value of surface potential. [29, 28]

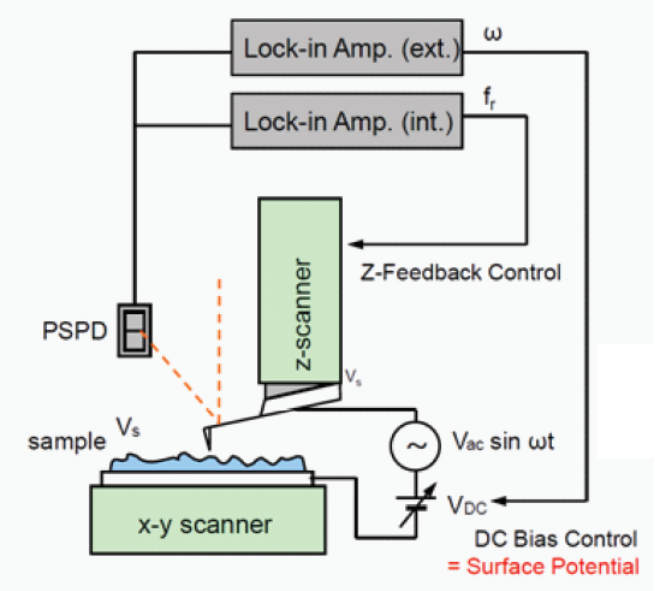

Figure 2.6: The set-up and feedback loop for SKPM methods. [30]

This technique does have some disadvantages. The resolution of the method is dependent upon contributions from the whole cantilever, which has been modelled by Colchero et al [31]. This is split into three contributions: the parabolic tip apex, the mesoscopic tip cone, and the macroscopic cantilever.

In most experimental scanning conditions, i.e. the tip has been lifted a few nanometers above the sample surface, the cantilever term will dominate and hence the resolution of the scan is of the order of the width of the lever. To enhance the resolution of the method there are two options; redesign the cantilever so as to reduce the contributions from the lever and tip cone by reducing physical dimensions and open angle respectively, or measure the force gradient as opposed to a direct measurement of force. The latter option is the method which will be explored in the next section, when we take the derivative of the force, we leave the tip apex term dominant (to about 80nm lift height) as the large but essentially constant terms of the cone and lever are eliminated.

2.2.3 EFM-Phase

Another EFM technique, designed to increase lateral scanning resolution, is EFM-phase. In this method, similar to SKPM, a two pass system is in place where the first is tapping mode AFM in which the topography of the sample is recorded, and the second pass is completed in interleave lift mode. The differences in the two methods arise in the second pass of the scan: whereas the electrostatic force is nulled in SKPM. In EFM-phase the phase shift is continually recorded as the tip bias is modulated. The phase shift relates to the force gradient, $\frac{dF}{dz}$, which accentuates the contribution from the tip apex with weaker contributions from the bulk of the tip and cantilever [32]. The tip experiences an electrostatic force from the sample surface given by equation 2.2.

When the force gradients are small, phase shift and resonant frequency are

$$\Delta\phi = -\tan^{-1}\left(\frac{k}{Q}\frac{dF}{dz}\right) \tag{2.8}$$

and

$$\Delta\omega = -\frac{\omega_0}{2k}\frac{dF}{dz} \tag{2.9}$$

where k, Q are the spring constant and quality factor of the cantilever respectively.

By taking the first derivative of equation 2.2 and substituting into equation 2.11 we obtain the phase shift as a function of potential difference between tip and sample, given by:

$$\Delta\phi = \tan^{-1}(\frac{k}{2Q}\frac{d^2C}{dz^2}(\Delta V)^2) \tag{2.10}$$

it can be shown that the resolution of EFM-phase methods is dependent on the lateral distribution of $\frac{d^2C}{dz^2}$ which has the greatest contribution from the apex region of the tip [33]. It is hoped that the development of this scanning method will increase the resolution of the images produced and be of particular benefit when scanning carbon nanotubes functionalised with proteins. Further information and more theoretical detail regarding the EFM-phase technique can be found in chapter

5.

2.3 Fluorescence microscopy methods

2.3.1 Confocal Microscopy

Confocal microscopy is a powerful optical imaging method with increased contrast and resolution compared to a standard optical microscope. The fundamentals of confocal microscopy were patented by Marvin Minsky in 1957 [34] with the overall aim of improving on current methods such as the traditionally used wide field fluorescence microscopy which homogeneously floods the entire sample with light. This process is unfavourable as many fluorescent molecules photo-bleach after prolonged exposure to light [35] and furthermore, the fluorescence detected by the microscope will include large unfocused background fluorescence. In a confocal microscope this issue is resolved by implementing point illumination in conjunction with a pinhole in an optically conjugate plane directly in front of the microscope detector. These modifications allow the elimination of unfocused signal. The confocal microscope also has an increased scanning resolution when compared to the wide field fluorescence microscope, since the detection of fluorescence occurs only very close to the focal plane, however as much of the detected signal is blocked by the pinhole the confocal microscope suffers from decreased signal intensity as is shown in figure 2.7. This can be mitigated by increasing the exposure time for each image [36].

Confocal microscopy allows direct and non-invasive imaging of living biological samples both in solution and when dried. For the experiments presented within this work, the samples were fluorescent proteins, immobilised through covalent binding onto a surface of single layer graphene. However it is worth mentioning that this method is frequently used across multiple disciplines from the study of cell biology to clinical uses. For example the imaging and evaluation of various diseases of the eye [38, 39].

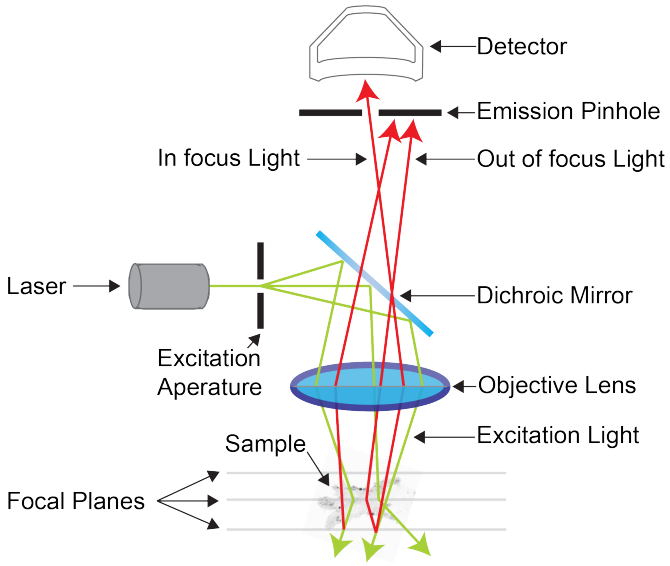

Figure 2.7: Depiction of the experimental set up for a standard confocal microscope. This diagram shows the removal of out of focus signal via the addition of a pinhole directly in front of the detector, allowing only focused fluorescence signal to be detected [37]

.

2.3.2 Total internal reflection fluorescence Microscopy (TIRFM)

TIRFM or TIRF microscopy uses total internal reflection (TIR) to illuminate cells in contact with a glass cover-slip. The initial idea was first developed in 1956 by E. J. Ambrose and then further extended in 1981 by Daniel Axelrod as the more fully formed TIRFM [40].

The mechanics of the TIRFM construct are that the evanescent wave, formed at the glass-liquid interface when the incident light undergoes TIR, will specifically illuminate and excite target fluorophores directly adjacent to the glass-liquid interface. Due to the exponential decay suffered by the evanescent wave, the depth of penetration into the liquid sample is restricted to the order of 100 nm which allows for selective imaging of surface regions. TIRFM is, as with confocal microscopy, widely used across multiple disciplines most notably in the biological sciences to observe single molecule fluorescence [41]. In the confines of the experiments presented within this work, TIRFM is employed to image and evaluate fluorescent proteins bound to carbon nanotubes.

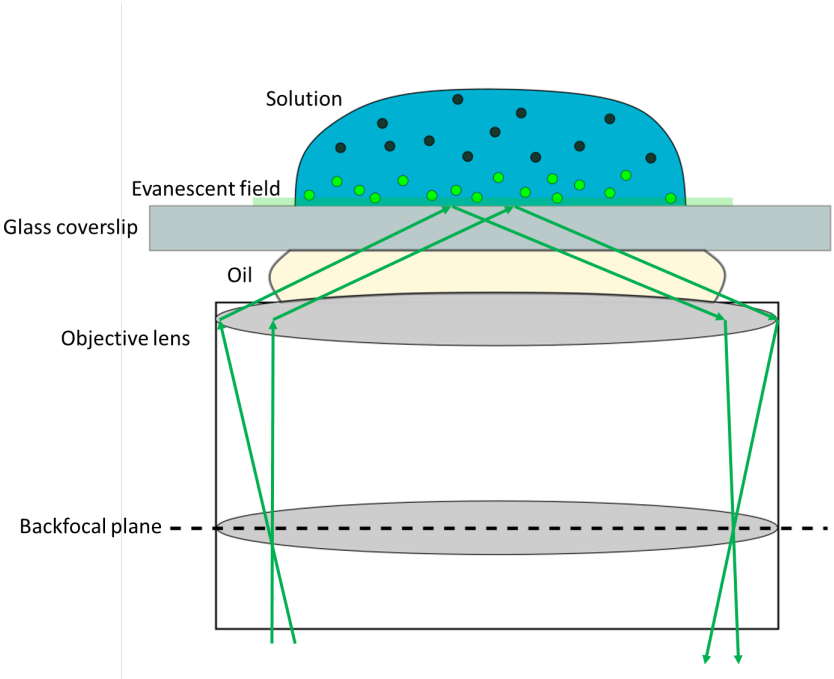

Figure 2.8: Experimental set up for TIRF microscopy, the dark circles within the solution represent fluorophores and the bright green circles represent fluorophores excited by the evanescent wave.

Chapter 3

General background

3.1 Organic Semiconductors

Organic semiconductors are materials formed from carbon based π-conjugated polymers and small molecules (classification based on molecular weight). They may exist in the form of amorphous thin films but also as molecular crystals. Organic and inorganic semiconductors exhibit vastly different behaviour. In the case of an inorganic semiconductor material it is, ideally, covalent binding that links the atoms in the material allowing standard electronic band theory to be followed [42].

A classical crystalline semiconductor is defined as a material which has an electrical conductivity between that of a conductor and an insulator. Electrical conductivity arises from the transfer of delocalised electrons between valence and conduction band, which in turn determines the behaviour of the semiconducting material [43, 44]. The properties of a semiconductor can be altered by introducing impurities into the crystal lattice, this is known as doping. An example of a pure (intrinsic) semiconductor is a pure crystal of silicon or germanium. When dopant impurities are added to intrinsic semiconductors, the electrical conductivity increases as there are now more free charge carriers within the crystal lattice. These doped semiconducting materials are also known as extrinsic semiconductors.

Doping is a crucial component in semiconductor fabrication that affects not

only electrical conductivity, but also optical, and structural properties of the material [45, 46]. Impurity atoms are added with such fine precision ranging from 10^8 to 10^3 impurity atoms per silicon atom [47]. The material used to dope the intrinsic semiconductor is also important as different impurity atoms result in different properties. For example: adding antimony impurity atoms to pure silicon will produce a p-type semiconductor as antimony is an acceptor/p-type dopant, whereas adding the donor/n-type material boron to the pure silicon will induce n-type behaviour in the resulting semiconducting material [48]. A visual representation of the addition of impurities can be found in figure 3.1.

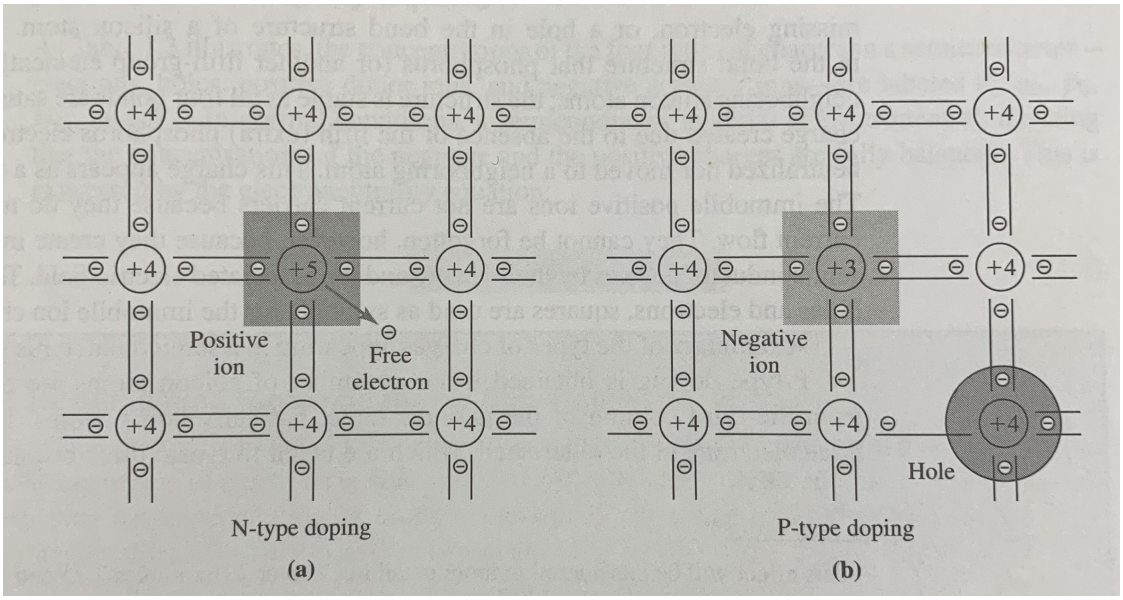

Figure 3.1: The effects on the pure crystal lattice upon the addition of (a) N-type impurity atoms and (b) P-type impurity atoms [49]

The addition of dopant impurities into the crystal lattice, whether donor or acceptor, causes a change in free carrier mobility. This results in an increase in electrical conductivity as there is now an imbalance between electrons in the valance band of the material and holes in the conduction band. This changes the Fermi level which makes it easier for valence electrons to move to the conduction band. A representation of this is shown in figure 3.2.

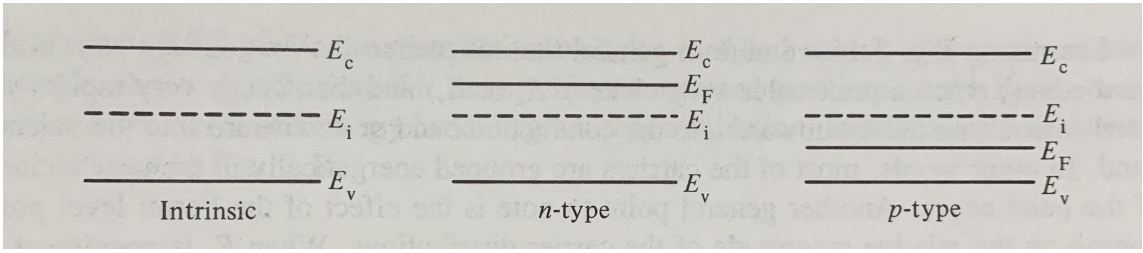

Figure 3.2: A representation of (left to right) intrinsic, n-type, and p-type semiconductor materials using the energy band diagram. The E_i line represents the position of the Fermi level were the material intrinsic in nature, serving as a reference energy level [47].

For a molecular organic semiconducting (OSC) material it is the overlapping of delocalised π-electron clouds between the conjugated molecules that gives rise to conductivity. In an organic semiconductor charge transfer takes place between the highest occupied molecular orbit (HOMO) and lowest unoccupied molecular orbital (LUMO). The energy difference in HOMO and LUMO level is often referred to as the HOMO-LUMO gap and is analogous to the valence-conduction band gap of inorganic semiconductors as is shown in figure 3.3 below.

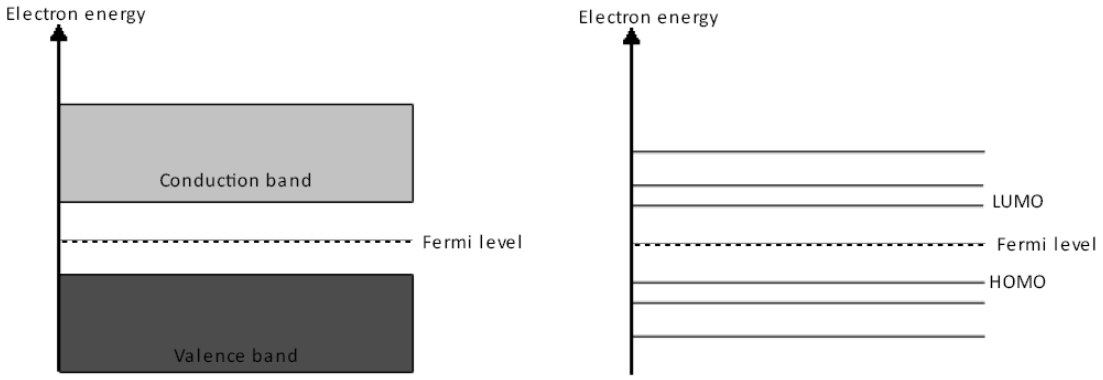

Figure 3.3: Diagrams to show the difference in density of states for a bulk semiconductor (left) versus an isolated molecular semiconductor (right)

3.2 Organic field effect transistors

Organic field effect transistors (OFETs) are useful devices that can be used to study the properties of an organic semiconductor. In this section, the operation,

characterisation, and derivation of fundamental material properties will be explored.

A field effect transistor consists of the following components: a gate electrode, separated from a semiconducting layer by an insulating dielectric; source and drain electrodes, separated by a distance L which represents channel length. This can be seen in figure 3.4. In the case of organic FETs the semiconducting layer is vacuum sublimated, drop cast or spin coated. The method of deposition is dependent on the organic material that is used [50]. The gate electrode is usually formed from heavily doped silicon, although the use of a conducting polymer or a metal is also reported [51]. The material selected for the dielectric layer is often chosen with respect to the structure of the transistor device [52], and can be formed of an inorganic insulator (such as SiO_2) or polymeric insulating materials such as poly(methylmethacrylate). Suitable materials for the source-drain electrodes are often chosen as high work function metals such as gold, but transistor devices have also been formed using printable conducting polymers, and in more recent work carbon nanostructures such as graphene and highly ordered films of carbon nanotubes [53].

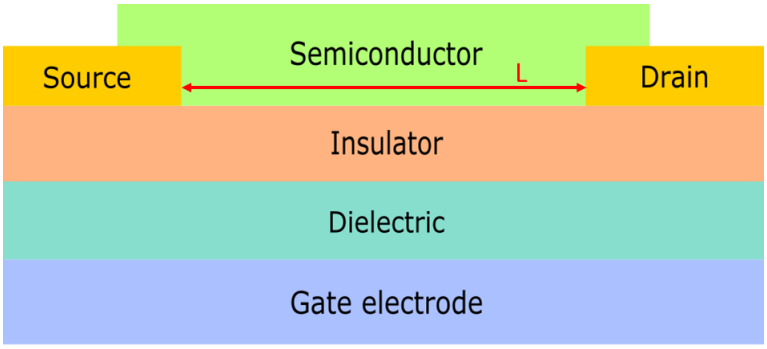

Figure 3.4: An example template for an organic thin film transistor type device. In this example the device is bottom gate, bottom contact.

In operation, a non-zero voltage is applied to the drain and gate electrodes (V_d and V_g respectively) while the source electrode is grounded ($V_s = 0$). The potential difference that is applied between the source and drain electrodes is commonly referred to as the source-drain bias, whereas the potential difference applied between the source and gate electrodes is known simply as the gate voltage. It is often more practical to refer to the effective gate voltage, given by: V_g - V_{th}, where V_{th} is the threshold voltage (the voltage required to turn the device on). For a more negative

source electrode, i.e. a positive gate voltage, the charge carriers that are injected are electrons. For a more positive source electrode and a negative gate voltage, the charge carriers are holes. It is this distinction between charge carriers that allows us to define FETs as either p or n-type devices. While some OFETs can conduct both hole and electron charge carriers (known as ambipolar), most exhibit predominantly n or p-type behaviour. The devices OFET devices used within this thesis are all p-type devices, and therefore the biases applied will be negative, in order to transport holes through the device channel. The transportation of charge carriers is intrinsically linked to the OSC and is dependent on HOMO and LUMO levels.

There are three basic operating regimes of a FET [54, 52, 55], each with associated current-voltage characteristics, an illustration of which can be found in figure 3.5. These are known as the linear regime, the start of the saturation regime at pinch-off, and the saturation regime. For the first instance, a potential is applied to the gate electrode such that $V_{sd} < V_g - V_{th}$. The gate voltage will induce either negative or positive charges at the interface between the semiconducting and insulating layers that have been injected into the device via the grounded source electrode. The charge accumulated is proportional to both the capacitance of the insulating material (C_i) per unit area, as well as the applied gate voltage. However, accumulated charges induced in this way are not always mobile, and hence will not contribute to the current flow in the device. Any deep lying traps in the device must first be filled before mobile charges can become available to contribute to the current. The point at which additional charges can become mobile is known as the threshold voltage V_{th} allowing the effective gate voltage to be defined as V_g - V_{th} [56]. However, filling of traps is not the only contributing factor: donor/acceptor states as well as dipoles at the interface of the device can cause an accumulation of charge carriers in the channel even at $V_g = 0$. In order to return the channel to its off state, a voltage opposite to the normal operation of the transistor must be applied. When $V_{sd} = 0$, the concentration of charge carriers within the channel of the FET is uniform. Upon the application of a small source-drain bias that satisfies $V_{sd} \ll V_g$ a linear gradient of charge density forms within the channel: this is the linear regime of device operation. In this case the applied source-drain bias is directly proportional to the current flowing through the transistor channel. In

terms of potential: V(x), at position x along the channel, increases linearly from the grounded source (at which V(x) = 0), to the drain electrode where V(x) = V_{sd}.

The next regime of operation, where saturation is beginning and pinch off is achieved, occurs when the V_{sd} is increased to the point that $V_{sd} \approx V_g$ - V_{th}. It is at this point that a depletion region begins to form within the device at the drain-channel interface, which is known as the pinch off point. V(x) - V_g is now lower than the threshold voltage of the device. Within this depletion region there is a comparatively high electric field, and as such a space-charge limited current ($I_{sd,sat}$) can flow as the charge carriers pass from the pinch off point to the drain. The current saturates at this level and increasing the source-drain bias will not increase it substantially. However, it will lead to a slight increase in the depletion region and as such a further shortening of the channel. This is the final saturated regime of operation.

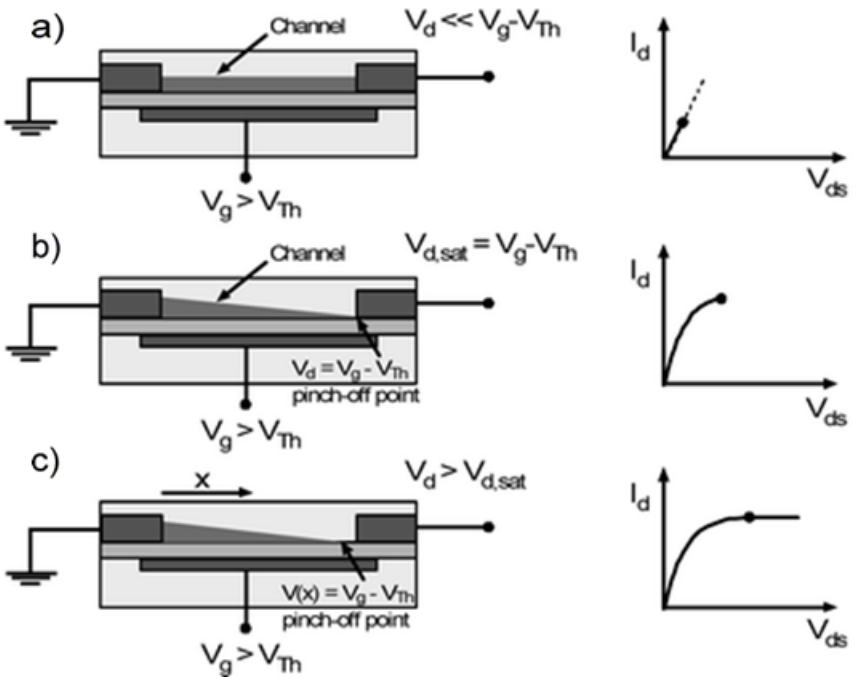

Figure 3.5: Illustrations of the three operating regimes of field-effect transistors and corresponding current-voltage characteristics: (a) linear regime; (b) start of saturation regime at pinch off; (c) saturation regime [52].

Analytically these operating regimes can be described by assuming the gradual channel approximation, i.e. the charge distribution within the channel is determined by the perpendicular field created by the gate voltage and not from

the parallel field which stems from the drain voltage. This model holds for long channel lengths, but fails when the device channel length is reduced below 1μm as the gate dielectric must also scale to below 100 nm. In order to obtain acceptable on-off device behaviour the ratio of gate dielectric thickness to channel length must be ≤ 0.1. If this ratio is much larger than 0.1 the device can no longer modulate the channel conductance due to screening of the gate field by the source and drain contacts. [52, 57, 58]

A device exhibits ohmic behaviour if the current through it is linear with the voltage applied across it and any potential drop at the contacts is negligible. An ohmic contact is defined as a contact which will not add a significant parasitic impedance to the structure on which it is used and will not sufficiently change the equilibrium carrier densities within the semiconductor to affect the device characteristics [44]. Thus in order to form good ohmic contacts, source and drain electrodes must be formed of a material whose work function is close to the HOMO or LUMO level of the semiconducting layer. If there is a large discrepancy between these two materials a potential barrier is formed, which leads to poor charge injection and subsequently Schottky like contacts. The lack of good ohmic contacts results in an additional resistance in the transistor device which is known as the contact resistance [59]. This contact resistance can be observed as a voltage drop at the electrode/channel interface which can be experimentally measured using a method such as SKPM. The contact resistance has the most impact on the device when it is operating in the linear regime. This is due to the fact that a large portion of the source-drain voltage is already dropped at the electrode/channel interface and not across the channel. This often presents itself in the output characteristics of the device as a region of initially suppressed followed by super-linear current increase in the linear region.

Often the metal-semiconductor interface will exhibit an additional dipole barrier, changing the work function of the metal and thus the height of the potential barrier. By intentionally introducing dipoles at the metal surface by, for example, the introduction of a self-assembled monolayer(s), charge injection into the semiconducting material may be improved. It is important to note that the

contact resistance that is often observed within transistor devices is not determined purely by the metal/semiconductor interfacing, but also by device structure. This is something that will be discussed in further detail later on in this chapter.

A study of the OSC material was conducted by modulating either source drain voltage (V_{sd}) or gate voltage (V_g). This results in the formation of two key plots: the output curves (I_d - V_d) and the transfer curves (I_d - V_g). Using the output curves the device operation at fixed gate voltage is explored and information regarding the behaviour in linear and saturation regime of operation such as: current, carrier concentration, conductance, and field effect mobility [60]. From transfer curves, in the linear regime of device operation, the threshold current for the device can be derived from the data plot, as well allowing calculation of the transconductance of the OSC material [43]. Transfer curves taken in the saturation regime of operation offer different information such as the region in which the device is turning from OFF (low current) to ON (high current) - known as the subthreshold regime. Furthermore, by plotting $I^{\frac{1}{2}}$ and taking the gradient of the plot at high V_g, the mobility of the OSC material can be calculated. Finally it is also possible to calculate the subthreshold swing of the device (how fast the device goes from OFF to ON), using the transfer curves.

3.2.1 Extracting parameters from device characteristics

To obtain the output characteristics for an OFET device V_{sd} is varied for a constant value of V_g. Once the gate voltage surpasses the threshold voltage of the device mobile charges are induced Q_{mob} per unit area of channel at the source/channel interface. This quantity is related to the gate voltage via

$$Q_{mob} = C_i(V_g - V_{th}). \tag{3.1}$$

where C_i is the capacitance per unit area of the dielectric material. However, this equation is based on the assumption that the potential within the channel is zero but the induced charge density is dependent upon the position within the channel

(x). We account for this in the following

$$Q_{mob} = C_i(V_g - V_{th} - V(x)). \tag{3.2}$$

Ohms law states that

$$V_d = I_d R \tag{3.3}$$

and if we combine this with the equation for electrical conductivity, assuming the mobility is bias independent it is possible to obtain

$$\sigma = \frac{RL}{A}, \tag{3.4}$$

where L is the channel length of the transistor device, A is the cross sectional area of the channel and σ is the electrical conductivity. Then

$$V_d = I_d \frac{L}{A\sigma}. \tag{3.5}$$

The cross sectional area of the channel can be described by multiplying the channel width (W) by the thickness of the charged layer, t,

$$A = tW. \tag{3.6}$$

Substituting this into equation 3.5 obtains

$$V_d = I_d \frac{L}{(tW)\sigma}. \tag{3.7}$$

The conductivity is directly related to the mobility of the charge carriers by the equation

$$\sigma = ne\mu \tag{3.8}$$

where n is the number density of charge carriers in the channel, e is the elementary charge and μ is the charge carrier mobility. Substituting equation 3.8 into 3.7 obtains

$$V_d = I_d \frac{L}{(\mu W)(ent)}. \tag{3.9}$$

From equation 3.2 the average value of induced charges in the channel, equivalent to the average carrier concentration in the channel, can be given as

$$Q_{mob,avg} = C_i[V_g - V_{th} - \frac{V_d}{2}] = net. \tag{3.10}$$

After substituting this equation into equation 3.9 and rearranging to make I_d the subject, the gradual channel expression for the drain current can be obtained:

$$I_d = \frac{W}{L}\mu C_i\left[(V_g - V_{th})V_d - \frac{1}{2}V_{sd}^2\right]. \tag{3.11}$$

When the transistor is operating within the linear regime, the equation above can be simplified to

$$I_d = \frac{W}{L}\mu_{lin} C_i(V_g - V_{th})V_{sd}. \tag{3.12}$$

Since the drain current is linearly proportional to the gate voltage, the field effect mobility within the linear regime (μ_{lin}) can be extracted from the gradient of I_d against V_g for a constant source-drain bias

$$\mu_{lin} = \frac{\partial I_{sd}}{\partial V_g} \cdot \frac{L}{WC_iV_{sd}}. \tag{3.13}$$

When $V_{sd} = V_g - V_{th}$ due to pinch off within the channel and subsequent saturation of the device current, the equation 3.12 is no longer valid. Neglecting channel shortening due to the depletion region at the drain electrode, the saturation current can be obtained by substituting V_{sd} with $V_g - V_{th}$

$$I_{sd,sat} = \frac{W}{2L}\mu_{sat} C_i(V_g - V_{th})^2. \tag{3.14}$$

In this saturated regime, the square root of the saturation current is directly proportional to the gate voltage however, this equation assumes that the mobility of the charge carriers is gate independent. If this is not the case, then a gate voltage dependent saturation mobility can be extracted via

$$\mu_{sat}(V_g) = \frac{\partial I_{sd,sat}}{\partial V_g} \cdot \frac{L}{WC_i} \cdot \frac{1}{(V_g - V_{th})}. \tag{3.15}$$

Graphical representations of the linear and saturation regimes can be seen in figure 3.6 which shows the transfer characteristics, i.e. the drain current versus the gate voltage for constant V_{sd} for an idealised n-channel transistor device.

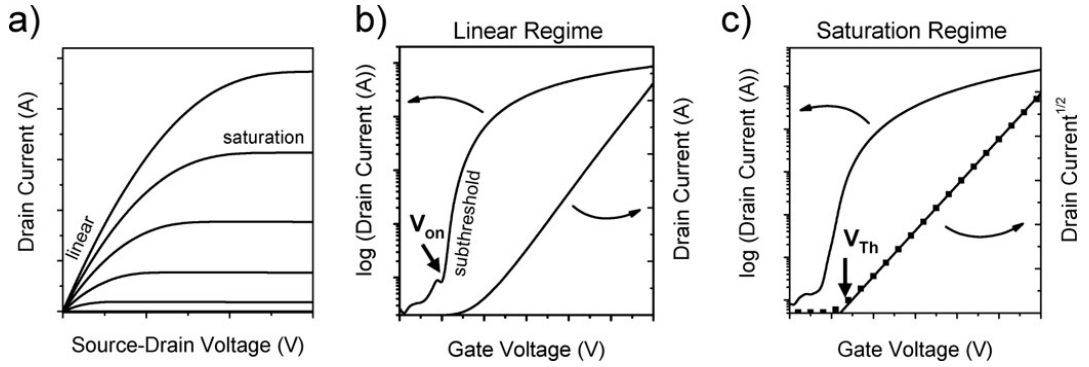

Figure 3.6: Representative current-voltage characteristics of an n-channel organic field-effect transistor: (a) output characteristics indicating the linear and saturation regimes; (b) transfer characteristics in the linear regime ($V_{sd} \ll V_g$), indicating the onset voltage (V_{on}) when the drain current increases abruptly; (c) transfer characteristics in the saturation regime ($V_{sd} > V_g - V_{th}$), indicating the threshold voltage V_{th}, where the linear fit to the square root of the drain current intersects with the x-axis. [52]

3.2.2 Contact resistance

One of the limiting factors affecting reliable operation and continuing reduction in device size is the large contact resistance observed in organic field effect transistors [61, 62]. As previously stated, in a transistor device, charge is injected from a metal source electrode and removed at a metal drain electrode after it has passed through some conductive channel. The channel material may be varied, from organic polymer blends to thin films of two dimensional materials such as graphene allowing for a vast range of specialised devices with varying operational ranges. In order to transport charge carriers from the metal electrode and into/out of the accumulation layer at the dielectric-semiconductor interface, a finite applied voltage is required. This leads to an abrupt potential drop at the channel-electrode interface which can be attributed to the contact resistance observed in device operation. There are various parameters which, through careful fabrication choices, allow some control over this injection process such as: the work function of the metal for charge injection, the ionisation potential of the semiconductor material, and the geometry of the device

[63].

In a staggered configuration (also known as top contact - TC) devices, the contact resistance has been shown to be less dependent on the work function barrier of the metal electrodes. This is due to the device geometry which forces the accumulation layer to be below the semiconducting material and the metal contacts to be formed on top. When there is constant contact between semiconductor and insulating layer of the device the sharp potential drop that is usually observed at the channel-electrode interface, and therefore the contact resistance, is significantly reduced. In the case of coplanar (bottom contact - BC) device geometry, the accumulation layer and the metal contacts are grown beneath the semiconducting layer, introducing an obstruction between the semiconductor and the insulator. In this case it is thought that the bulk film resistance of the OSC layer plays the largest role in contact resistance [64]. In the BC device geometry, injected carriers must travel vertically through the OSC to reach the channel, as can be seen in figure 3.7, and in this case the metal/OSC injection barrier seems not to play such a significant role. By introducing a self assembled monolayer (SAM) above the contacts in BC devices, the contact resistance of the OFET can be lowered [52, 65]. The reduced contact resistance observed in SAM functionalised devices is due mainly to increased channel mobility as the addition of the SAM aids in OSC layer growth, which will be more fully investigated in chapter 4. There are multiple methods in which contact resistance can be investigated, but within this thesis non-contact scanning probe potentiometry - scanning Kelvin probe microscopy is utilised.

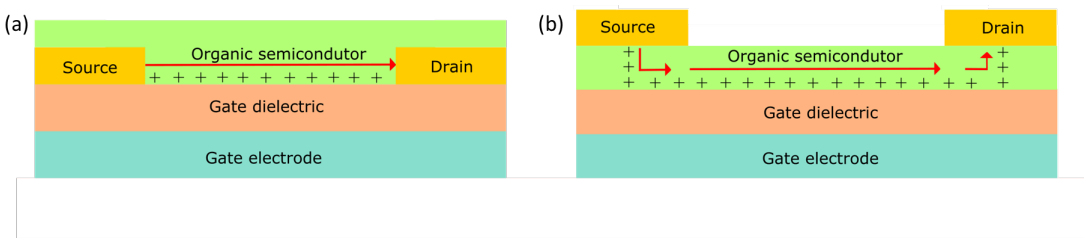

Figure 3.7: An illustration of the injection of charge carriers (holes) into the OFET channel for (a) BC device geometry and (b) TC device geometry

3.3 Protein attachment

3.3.1 Introduction to protein structures

In this section, a basic overview of the structural properties of proteins will be presented. In subsequent sections, individual protein structures will be introduced with more detail. In order to fully understand the role each protein plays in the experimental work to follow, it is pertinent to understand how and why proteins form and act in the manner that they do. A range of proteins are essential to life: cells will not function without them. Within each protein amino acids are linked together by peptide bonds to form a polypeptide chain. These chains, depending on the order of the amino acids, twist into a multitude of complex three dimensional shapes. This is known as folding and the correct fold for each protein type is crucial for functionality [66]. Misfolding in proteins causes cells to behave incorrectly leading to various proteiopathies (protein misfolding diseases) such as Alzheimer's disease [67], prion diseases and a wide variety of other disorders [38].

The structure of a protein can be described at four levels. The first, known as the primary structure, describes the unique sequence in which the 20 amino acids that construct each protein are linked in a chain. The specific and unique order of these amino acids is the deciding feature in the folded conformation of the structure. The second level of structural composition is known as the secondary structure and refers to the local 3-D shape formed by the folding of the polypeptide chain. These secondary structures are broken down into two types: alpha (α) helix and beta (β) sheet. The α-helix structure resembles, as the name implies, a helical coil and is formed through hydrogen bonding within the polypeptide chain which coils the chain into this shape. The second secondary structure is the β-sheet, in which the polypeptide chain appears pleated. In the case of a β-sheet structure, the polypeptide chain is bound by hydrogen bonds formed between polypeptide units in between the folded chain. α-helicies are usually represented by the use of helical ribbons, whereas β-sheets are represented by arrows.

The third, tertiary level structure of proteins represents the domain formed when the secondary structures of one polypeptide chain are packed together. Tertiary structures are held together by various bonds such as hydrogen and ionic bonding as well as hydrophobic and van der Waals interactions. Covalent bonding may also occur when two sulphur atoms from different side-chains bind to form a disulphide bridge. This packing of domains in proteins is known as a quarternary structure. If a protein is composed of multiple peptide chains then each chain is referred to as a sub-unit [68, 69, 70].

3.4 Proteins studied in this thesis

The proteins that were studied in this thesis are now introduced. The first protein which will be introduced here is the green fluorescent protein (GFP): a robust and highly stable protein. GFP is a proton pump with a chromophore at its core which allows easy visualisation in order to confirm retention of activity [38]. GFP can survive drying and ambient conditions.

The second protein studied within this thesis is cytochrome b_{562}, a redox protein that has been dimerised in two ways allowing for the study of short and long axis binding to carbon nanostructures. The dimer form of the protein can be chemically broken allowing the study of the monomeric form as well as the dimer.

Finally, in order to form a bio-sensing mechanism, a detection protein and its analyte are introduced. In this thesis these are the Beta-lactamase inhibitor protein (BLIP-II) as the detector and TEM beta-lactamase (TEM-1) as the analyte. This interaction is particularly interesting as TEM-1 is one of the enzymes responsible for resistance in bacteria to beta-lactam based antibiotics.

3.4.1 Green fluorescent protein

Green fluorescent protein (GFP) is a fluorescent protein composed of 238 amino acid residues and presents in a cylindrical shape due to the 11 stranded β-sheet in a

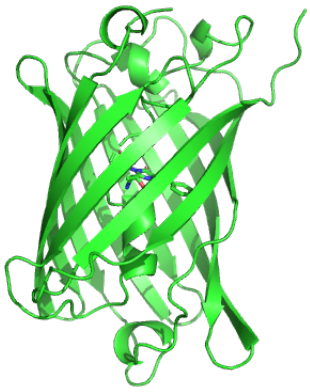

Figure 3.8: Wild type superfolder green fluorescent protein (wt sfGFP)

pleated sheet arrangement which forms a beta barrel. An alpha helix containing the covalently bound chromophore runs through the inside of the beta barrel. The barrel structure is nearly perfectly cylindrical unique to the GFP family of proteins. It is 4.2 nm long with a diameter of 2.4 nm [71]. GFP exhibits a bright green fluorescence when exposed to blue-ultraviolet wavelength light and has a major excitation peak at a wavelength of 395 nm and a minor excitation peak at 475 nm. It emits in the lower green portion of the visible spectrum with an emission peak at 509 nm wavelength with a shoulder at a wavelength 540 nm.

It was first purified from the bio luminescent jellyfish Aequorea victoria [72, 70]. While this is the first recorded method for the production of GFP, more modern practices utilise cells of E. coli to express the protein for biological research purposes. The widespread usefulness of the GFP has led to the engineering of many variants of GFP, including colour mutants of a wide range. One particular mutant of GFP that is pertinent to this study is superfolder GFP (sfGFP). This particular mutation was produced to address misfolding of wild type GFP (wtGFP) upon expression from E. coli and is a more robustly folded version of GFP [73].

3.4.2 Cytochrome b_{562}

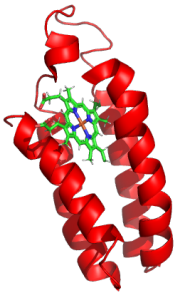

(a) Wild type cytochrome b_{562}

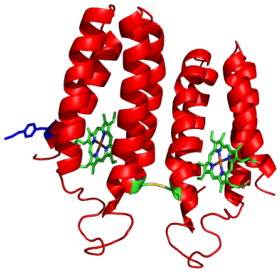

(b) Short axis dimerised cytochrome b_{562}

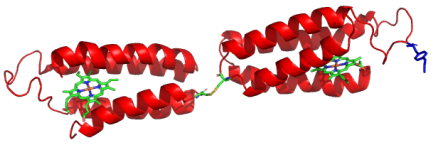

(c) Long axis dimerised cytochrome b_{562}

Figure 3.9: The molecular structure of three variants of the cytochrome b_{562} molecule

Cytochrome b_{562} (cyt b_{562}) is another protein that was be used in the work of this thesis and as with GFP its modern production originates from E. coli cells. Cyt b_{562} is a four anti-parallel α-helix protein comprised of 106 amino acids which non-covalently bind to a single heme group [74]. The presence of the heme group in this protein makes it a redox protein. Cyt b_{562} is regarded as one of the simplest examples of a redox active protein and exhibits a redox-potential that responds to environmental stimuli as well as carrying out electron transfer [75, 38].

Artificial cyt b_{562} dimers were produced via the introduction of cysteine residues allowing for the dimerisation of monomer cyt b_{562} through disulphide bridging. It is hoped that the subsequent reduction of these disulphide bridges within the artificial dimer structure will result in greater control of binding orientation when covalently bound to a carbon nanotube.

Two cyt b_{562} dimer structures were synthesised: long axis (cyt $b_{562}{}^{LA}$) and short axis (cyt $b_{562}{}^{SA}$). For the cyt $b_{562}{}^{LA}$ mutant the cysteine residue is

engineered into position 50 and for the cyt $b_{562}{}^{SA}$ mutant the cysteine is engineered into residue 104. For both of these mutants, the cysteine residue is engineered into a surface accessible position which allows for the formation of a disulphide bridge between the residue present on each monomer, thus forming a dimerised form of cyt b_{562}.

3.4.3 Beta-lactamase inhibitor protein and TEM beta-lactamases

Beta-lactamase inhibitor proteins (BLIP) are part of a family of proteins produced by bacteria such as streptomysces clavuligerus. Beta-lactam based antibiotics are some of the most widely used antimicrobial medicines [11, 76], and with the recent and rapid rise of antibiotic resistance the loss of efficient and potentially life saving treatment is a real threat to public health care. The most prominent mechanism of this resistance to beta-lactam based antibiotics is the production of enzymes such as TEM-1 (the most common penicillin resistance beta-lactamase enzyme) that catalyse the hydrolysis of the beta-lactam ring rendering antimicrobial agents ineffective[12, 77]. An in depth study regarding the mechanics of this process within the TEM-1 enzyme was published in 1996 by Christian Damblon et al [13].

BLIP is formed of 165 amino acid residues and is a protein inhibitor of class A β-lactamases and was discovered in 1990 [78]. In more recent years, other BLIP's have been discovered including BLIP-I which is similar to BLIP in both sequence and protein fold, and BLIP-II which is unrelated to the structure and protein fold of BLIP and BLIP-I [79]. The structure of BLIP-II (figure 3.10) is a seven blade β-propeller fold that, through a number of β-turns and loops, forms interactions with the loop-helix region of β-lacatamase from positions 99 to 114[80]. Studies of BLIP-II have provided data indicating the potency of inhibition to be significant and demonstrating a binding constant in the pico-molar range for multiple enzymes including TEM-1 [81, 82].

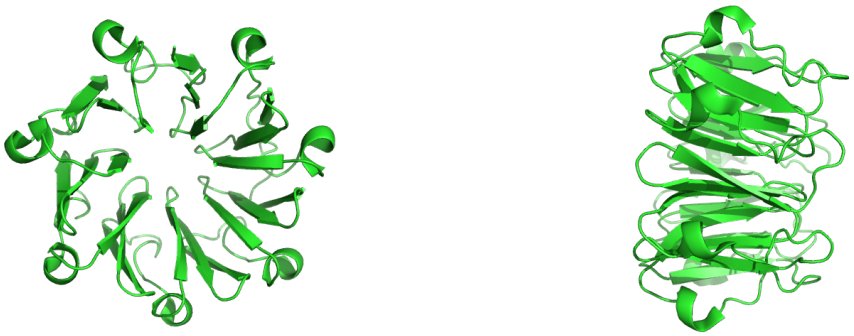

(a) 'Top' view of BLIP II protein structure (b) 'Side' view of BLIP II protein structure

Figure 3.10: The molecular structure of wtBLIP II protein viewed from two orientations. (a) illustrates the 'propeller' like structure, where (b) illustrates a side on view of the protein with the active binding site located to the right hand side of the protein

The structure of the TEM-1 enzyme consists of two domains as can be seen in figure 3.11. The first domain is formed of a five-stranded beta-sheet covered by three alpha helices on one face and one alpha helix on the other face. The second domain is comprised of mainly alpha helices. It is at the interface of these two domains that the catalytic cleft is located, which is responsible for catalysing the hydrolysis of the beta-lactam ring - resulting in the inactivation of beta-lactamase based antibiotics.

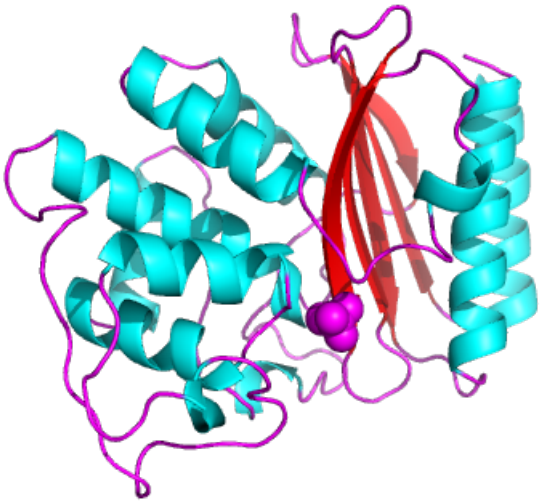

Figure 3.11: A representation of the structure of the TEM-1 enzyme created using Pymol from the protein data bank. The structure has been coloured with respect to secondary structure to illustrate the two domains more clearly.

The interaction between the BLIP II structure and the TEM-1 enzyme has been the focus of many studies [83, 82]. The active binding site of BLIP-II is well documented and the interaction between the BLIP-II and the TEM-1 is shown in figure 3.12 where the active binding site is shown in pink, the BLIP II in green, and the TEM-1 enzyme in blue.

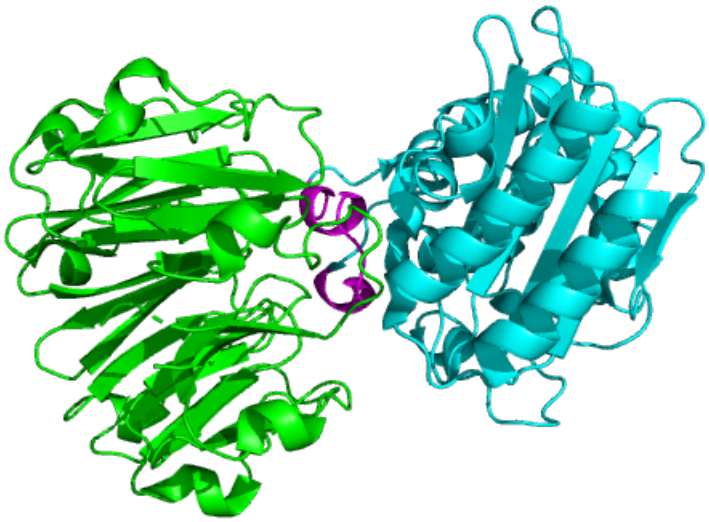

Figure 3.12: The molecular interaction between BLIP II protein and TEM-1 enzyme where the active binding site is shown in pink, the BLIP II in green, and the TEM-1 in blue.

3.4.4 Azido phenylalanine chemistry

In order to bind each of the aforementioned proteins to carbon nanostructures, they must be functionalised with a molecule that will interface with the carbon nanostructure covalently or non covalently. In each of the experiments presented within this thesis a covalent bond between the carbon and the protein is formed by the interaction between the non-proteinogenic non-canonical amino acid (ncAA) *p*-azido-L-phenylalanine (azF) and the carbon nanostructure. The azF is inserted into each protein variant at various positions on the protein surface to best suit the purpose of each experimental aim.

In the case of sfGFP, there are multiple variants that can be produced. The focus, in this work, is on sfGFP 204 azF as it has been found to be the most reliable when attaching to tubes, however the azF molecule has been successfully inserted into residues at positions 132, 111, and 80. These variants will also feature in the work presented in this thesis. For the cyt b_{562} mutants in monomer form cyt $b_{562}{}^{LA}$ and cyt $b_{562}{}^{SA}$ the azF residues are engineered into the positions 50 and 5 respectively. This means that once dimerisation has occurred, each cyt b_{562} dimer pair has two azF residues on the protein surface allowing greater control over orientation upon binding to carbon nanostructures. Finally for the BLIP-II the azF was inserted into the 41 residue position. This residue was selected as it allows for sufficient access of the key interaction sites of the protein to facilitate the detection of the wtTEM analyte protein. Detailed diagrams including residue positions can be found in chapter 6 at the beginning of each specific protein experiment section.

The azF in each of these experiments has been inserted into the protein by reprogramming the genetic code without affecting the functionality, stability or structural properties of the protein. In order to incorporate this azF into the protein structure, two plasmids were required; pDULE, which carries the engineered tRNA and tyrosyl tRNA synthase for azF incorporation and pBAD (Invitrogen) which carries the gene of interest and the desired TAG (reprogrammed amber stop codon) mutation [84]. The azF is a photochemical reaction handle, meaning that upon the addition of UV irradiation with light of wavelength below 310 nm the azF loses the N2 group and forms a reactive nitrene radical with two lone pairs of electrons that inserts itself between the C=C bonds of the sp^2 carbon nanostructure forming a covalent bond. This binding method successfully binds the azF to the carbon without the introduction of breakage in the C-C bonded network and therefore has a minimal effect on the conjugated π-bond network [85, 86, 87].

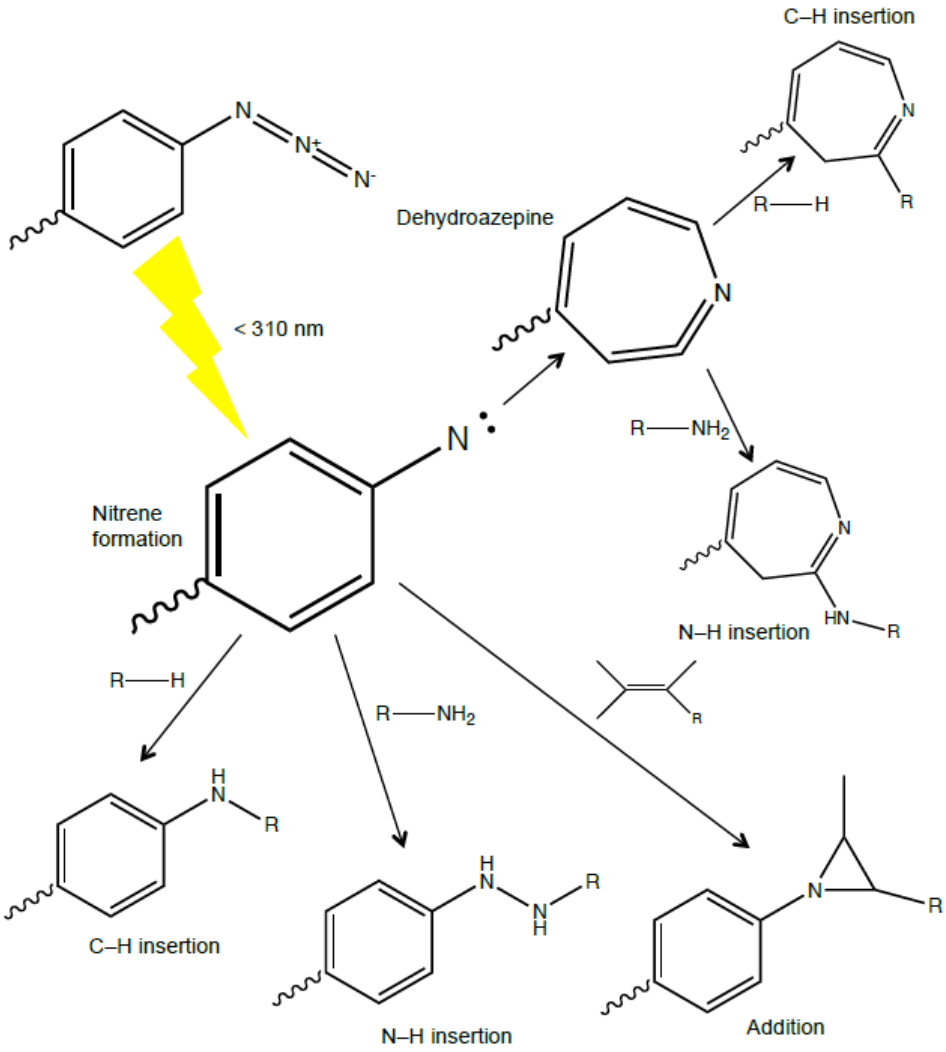

Figure 3.13: UV activation of the azF photochemical reaction handle. Irraditation of azF using light of wavelength less than 310nm causes the loss of nitrogen group and the subsequent formation of the nitrene radical [88].

3.5 sp^2 carbon nanostructures

The blanket term of carbon nanostructures encompasses many variations of low dimension carbon allotropes each with unique applications to many fields. Some of these allotropes include: graphene, carbon nanotubes, graphene nanoribbons, buckminster fullerenes, nanodiamonds and carbon nanodots which hold many interesting and widely different properties.

The focus of this section will be on graphene and its parent structure highly oriented pyrolytic graphite (HOPG), and carbon nanotubes; as these are the

structures which are the most useful in the purview of the experiments contained within this thesis. Here, the formation, dynamics, and useful properties of these structures is explored with a focus on the exploitation of the unique qualities these structures possess.

3.5.1 Highly oriented pyrolitic graphite

Highly oriented pyrolytic graphite (HOPG) is a synthetic form of graphite produced to eliminate the defects and imperfections found in naturally occurring graphite structures. Pyrolytic graphite in particular is a synthetic graphite structure with a high degree of crystallographic orientation and is formed by either graphitization of pyrolytic carbon (produced by heating a hydrocarbon almost to its decomposition allowing the graphite to crystallise.) or by chemical vapour deposition. The formation of HOPG is based upon the method for the production of pyrolytic graphite, but with the addition of a tensile stress applied in the basal plane direction. This addition improves alignment of graphite crystals and allows for interplanar spacing like that of naturally formed graphite. This method, first documented in 1962 by L. C. F. Blackman and Alfred Ubbelohde, is known as stress recrystallization of graphite [89].

HOPG is very close in many of its properties, including preferred orientation in the plane (0001), density, parameters of the crystal lattice and anisotropy of its physical properties, with the natural mineral form of graphite. HOPG however, similarly to mica (another widely used substrate material) is lamellar in form. This is because the crystal form of HOPG can be characterised by the arrangement of the carbon atoms which form in stacked, parallel layers. The structure of graphite can be described as alternate layers of single atom thick graphite, which explains the cleaving behaviour characteristic of HOPG and mica structures.

The lattice of HOPG is such that two triangular sub-lattices of carbon atoms, each with three nearest neighbour carbon atoms from the opposite sub-lattice. The result of the interpenetration of these sub-lattices is described in figure 3.14.

For the experiments presented in this thesis regarding HOPG, we use a sample obtained from agar scientific with a mozaic spread of 3.5 +/- 1.5 and dimensions 10 mm x 10 mm x 2 mm.

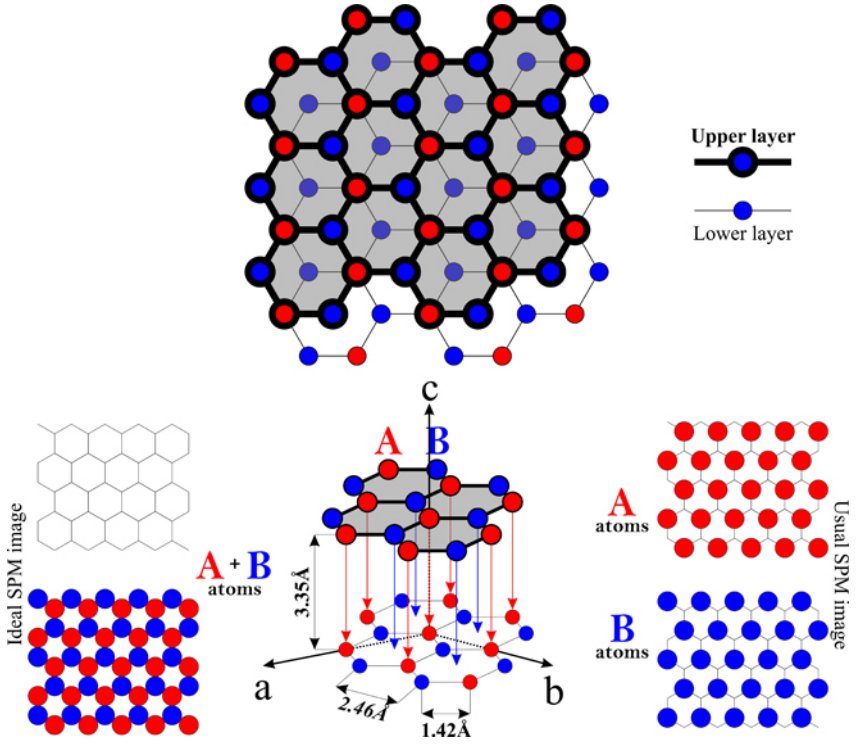

Figure 3.14: The interpenetrating layers of carbon honeycomb lattice forming HOPG bulk crystal structure. Also shown is the ideal SPM image compared to the SPM image generally obtained [90].

3.5.2 Graphene

Graphene was initially synthesised by repetitive mechanical exfoliation of a bulk HOPG crystal using scotch tape in 2004 by Nosvelov and Geim [91]. It was quickly established that this material had many applications in various areas of the physical sciences. Single-layer graphene (SLG) and few-layer graphene (FLG) are of specific interest as they exhibit the electronic behaviour of a semi-metal differing from the behaviour of multi-layer and bulk 3D crystal.

Graphene is described as a zero gap semiconductor as its conduction band and valence band meet at the Dirac points. These are six points in momentum space at the boundary of the Brillouin zone and are divided into two sets: K and K' [92].

The structure of graphene is a honeycomb like lattice of carbon atoms as shown in figure 3.15 which can be seen as a triangular lattice with two carbon atoms per unit cell, the two lattice vectors can be described as

$$\mathbf{a}_1 = \frac{a}{2}(3, \sqrt{3}), \mathbf{a}_2 = \frac{a}{2}(3, -\sqrt{3}), \tag{3.16}$$

Where the carbon-carbon (c-c) distance, a, is 1.42 Å. The reciprocal lattice vectors can then be given as

$$\mathbf{b}_1 = \frac{2\pi}{3a}(1, \sqrt{3}), \mathbf{b}_2 = \frac{2\pi}{3a}(1, -\sqrt{3}). \tag{3.17}$$

These can be related to the physical lattice form as is shown in figure 3.16

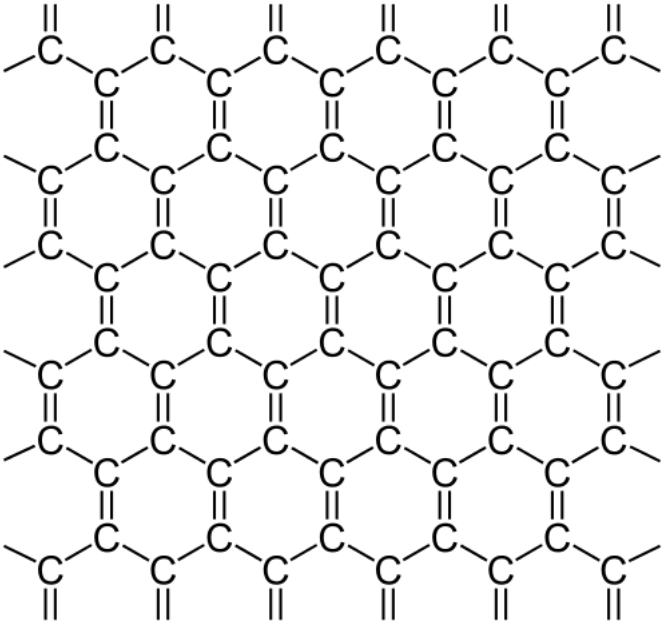

Figure 3.15: Honeycomb lattice structure formed by carbon atoms of single layer graphene.

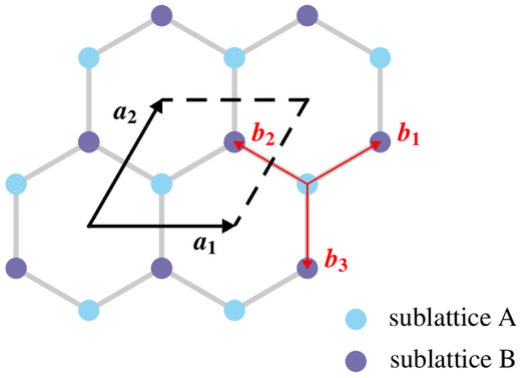

Figure 3.16: A representation of the sublattice structure of graphene showing the positions of the lattice vectors and reciprocal lattice vectors with respect to the graphene lattice structure [93].

Although initially prepared from bulk HOPG crystal, graphene is more frequently produced using chemical vapour deposition (CVD) allowing large films to be grown on metallic substrates (such as copper) and then transferred to silicon. This is the method of formation from which the graphene samples used in this work were produced. The samples imaged show large area coverage of single to few layer graphene, of high quality. This makes them perfect target areas for protein binding.

3.5.3 Carbon nanotubes

Since their discovery and subsequent description by S. Injima of Japan in 1991, carbon nanotubes (CNT's) have become an integral structure in the study of nano-physics. Their unique properties and robust nature lend them to vast applications in fields such as nano-medicine, nanotechnology, sensing devices, transistors. and membranes.

CNT's are simply rolled up sheets of graphene with a sp^2 hybridisation. They are light weight with a small size and high aspect ratio. CNT's exhibit incredible tensile strength as well as unique electrical, thermal and mechanical properties [94, 1].

The structure of the nanotubes can be described as a network of hexagonal cells, the sp^2 network. An important property which is directly linked to this network is the chirality of the nanotube. This is defined in terms of the orientation of the

hexagonal cells with relation to their alignment to the longitudinal axis of the tube. The chirality of a nanotube is described by two integer values (n and m) that denote the location of a hexagon within the network which, once the nanotube is rolled, will align with the hexagon located at the origin of the given coordinate system. The chiral vector is given by the equation

$$C_h = na_1 + ma_2 \tag{3.18}$$

where a_1 and a_2 are unit vectors within the hexagonal lattice structure.

The chirality of a nanotube can also be specified by its chiral angle(Θ), with two specific angles that are of particular interest. Θ is given by the equation:

$$\Theta = tan^{-1}\left(\frac{\sqrt{3}m}{m+2n}\right). \tag{3.19}$$

This angle is the result of the direction of nanotube rolling in conjunction with the direction of the common edge of two hexagons within the lattice. The two angles of interest are $\Theta = 0°$ and $\Theta = 30°$, which give nanotubes of vastly different characteristics. When $\Theta = 0°$, so called zig-zag type nanotubes are formed and when $\Theta = 30°$ the variant of nanotubes formed are called arm-chair type nanotubes as shown in figure 3.17. The final property that is crucial to the determination of the nanotube properties is the diameter of the tubule. The chiral symmetry of the nanotubes is determined by the values n and m. The chiral vector and diameter determine the differences in nanotube properties. In terms of the integer values m and n, the diameter of the tubes is

$$d_t = C_h/\pi = \frac{\sqrt{3}a_{c-c}(m^2 + mn + n^2)^{\frac{1}{2}}}{\pi} \tag{3.20}$$

where a_{c-c} is the distance between the nearest carbon atoms, which in the carbon nanotube relates to graphene which has an a_{c-c} of 0.1421 nm and C_h is the chiral vector of the tube. Whereas the chirality of the tube determines its variant, any variation in the tube diameter and chiral angle Θ determine its unique properties.

The strength of the sp^2 network of carbon-carbon bonds is what gives rise

to the unique mechanical properties that CNT's provide. With a highest recorded tensile strength of 63 GPa, around 50 times that of recorded values for steel, CNT's make for excellent, robust, test structures. Aside from strength of material, CNT's also exhibit excellent thermal and electronic properties with some tubes presenting an electronic conductivity even higher than copper. Further to this CNT's have exceptional chemical and environmental stability, another reason why they are an ideal candidate for bio-sensing applications [95].

For the duration of the studies presented within this thesis semiconducting single wall CNT's (sSWCNT's) are used, however tubes which exhibit metallic behaviour are also available, depending of the rolling of the tube from the graphene lattice as discussed above. By careful control of the diameter of the tubes, electrical conductivity can be selected, ideal for use in main stream technological products such as fuel cells and flat panel displays, whereas the selection of a well defined band structure and electrical characteristics lends itself to sensing applications.

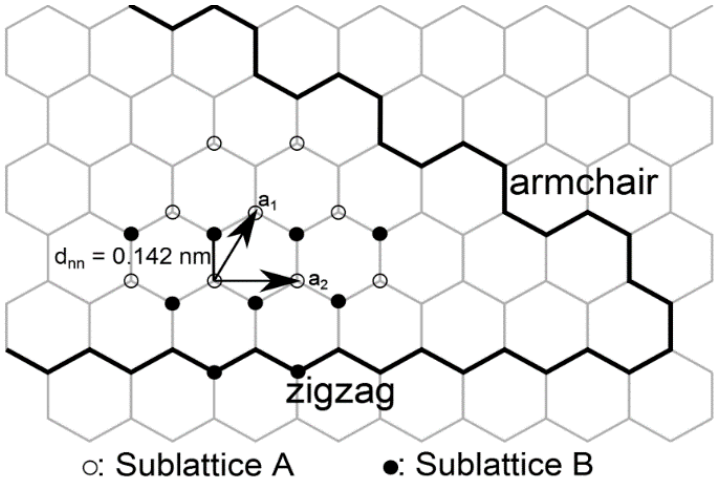

Figure 3.17: The armchair and zigzag configurations of carbon nanotubes as shown on flat single layer graphene. Once rolled along the axes shown, this becomes the formation of the carbon nanotube.

Chapter 4

Scanning Kelvin probe microscopy studies of organic field effect transistors

4.1 Motivation

With the advent of wearable technology and rise of bio-integrated sensing devices, there has been an rapid rise in the advancement of sensors, colour displays, and lab on chip devices. It is with this in mind that organic thin film transistors (OTFT's) become of particular interest to both commercial and scientific communities [96, 97, 98]. However meteoric the rise of this field has been, it is not without its difficulties. In order to take organic devices from the research lab to up-scaling for commercial use, the longevity and stability of the devices must be addressed and a standard for defining device characteristics established. One of the more pressing challenges is the development of conjugated polymers with semiconducting properties that will maintain stability in ambient air conditions, as well as providing a large field effect mobility [99, 100, 101, 102, 103, 104].

In this chapter the local electrostatics of both the electrode-channel interfaces and along the channel of organic field effect transistor (OFET) devices will

be explored. Different device configurations will be investigated in depth using various scanning probe microscopy methods in order to form a cohesive view of the electrostatic and topographical characteristics of these devices. The first of the two main studies presented in this chapter consists of OFET's comprising an organic layer of DNTT, a conjugate semiconductor material with impressive characteristics, in three distinct device configurations in order to compare and contrast the working capabilities of each design. The second study comprises OFET's with an organic semiconducting material combined with a polymer to form a blended channel material, in this study two different blend materials, each with a doped and undoped variant, are investigated.

4.2 Dinaptho[2,3-b:2',3'-f]thieno[3,2-b]thiophene devices

4.2.1 Introduction to dinaptho[2,3-b:2',3'-f]thieno[3,2-b]thiophene devices

Despite the well-known importance of device geometry in the field of OTFT, and indeed organic field effect transistors (OFET's), there is a distinct lack of model or physical description that can account for favouring staggered (top contact bottom gate - TC) geometry over coplanar (bottom contact bottom gate - BC). As the field of organic electronics becomes more technologically relevant, an increase in discussions surrounding how key device behaviours are not only measured and interpreted, but how they are reproduced and advertised. In order to assess the best methods to improve the general field of organic electronics, more importance must be assigned to the standardisation of device structure and hence device characteristics.

In general most OFET's are fabricated with a bottom gate (BG) structure with two main configurations of the source/drain contacts[105]. It is widely believed that TC or staggered devices have lower contact resistances. However previously suggested reasons usually rely on explanations that are not sufficiently supported

physically, such as morphological continuity of the conjugated semiconductor. By combining the theoretical model suggested by Dr Chang-Hyun Kim in 2011 [106] with scanning Kelvin probe microscopy (SKPM) of real DNTT OFET's it is possible to show that the increased contact resistance seen in BC/coplanar devices arises from lack of continuous contact between the conjugated semiconductor DNTT and the insulator and further show mitigation of this abrupt potential drop through introduction of a self assembled monolayer (SAM).

4.2.2 Dinaptho[2,3-b:2',3'-f]thieno[3,2-b]thiophene (DNTT)

For many years one of the most widely used organic conjugated polymer materials has been the small molecule hydrocarbon pentacene [107]. However despite the ability of pentacene to provide OTFT operation in ambient conditions [108] as well as presenting an initial high field effect mobility (usually around $1cm^2/Vs$ or above [109]), the molecules oxidise very easily in air. This has the detrimental effect that the initially high field effect mobility quickly decreases over time with continued exposure to these conditions. To circumnavigate the mobility degradation induced by ambient conditions, the devices can be encapsulated, using inorganic compounds mixed with the organics to form permeation barriers [110]. However this encapsulation requires many additional processing steps and needlessly complicates device development. The alternative to this method is to develop a new semiconducting conjugated polymer whose structure and characteristics are similar to pentacene, but with an additional intrinsic resistance to oxidation. Taking into account this list of attributes a fused heteroarene; dinaptho[2,3-b:2',3'-f]thieno[3,2-b]thiophene (DNTT) has been synthesised by vapour deposition. DNTT is now widely regarded as the 'post pentacene' material boasting a highly crystalline thin film structure that promotes high hole mobility and a much higher ionisation potential ($\approx$ 5.4 eV) leading to prolonged air stability when compared to pentacene ($\approx$ 5.1 eV).

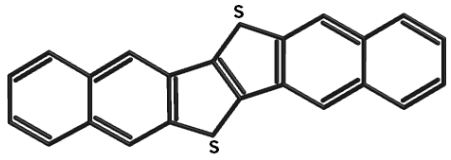

(a) Chemical structure of DNTT

(b) Chemical structure of pentacene

Figure 4.1: Chemical structures of the small molecule hydrocarbons; pentacene and DNTT

4.2.3 Fabrication and preparation of DNTT OFET samples

The DNTT OFET devices discussed in this chapter were fabricated by Dr Chang-Hyun Kim of the Gwangju Institute of Science and Technology (GIST) in South Korea. Three technologically relevant geometries of device were fabricated as can be seen in figure 4.2. A gate substrate of heavily doped n-type Si wafers were cleaned with acetone, isopropanol and dried under a nitrogen stream. The substrate was then subjected to an oxygen plasma treatment to remove any organic material before a solution of poly(methyl methacrylate) (PMMA) (M.W. = 120,000, 40 mg/mL in toluene) was spin-coated (2000 rpm for 45 s) onto the surface. The surface was then annealed at 120°C for 30 minutes leaving a film of thickness 200 nm. For both BC and BC-SAM devices structures, it was required that a 5 nm chromium wetting layer was first deposited before the 35 nm Gold source/drain electrodes could be deposited by thermal evaporation. To prepare the SAM's for the BC-SAM devices the samples were immersed into a solution of 10 mM pentafluorobenzene (PFBT) solution (in isopropanol) for 10 minutes, followed by a thorough rinse with pure isopropanol and finally drying under flowing nitrogen. The organic channel was deposited simultaneously for all devices using thermal evaporation of DNTT at 0.2 Å/s resulting in a final nominal thickness of 40 nm. For the TC OFET's, gold source/drain electrodes of thickness 30 nm were vacuum deposited onto the organic semiconducting layer, in this case there is no need for a chromium wetting layer. For each step in the evaporation process, a dedicated shadow mask was used to make the patterns. The channels of the devices have a width of 500 μm and a length of 50 μm.

The BC and TC devices represent, respectively, coplanar and staggered OFET device configurations. A bottom gate is usually employed when the molecular semiconductor is vacuum processed [111]. In the case of the BC-SAM devices, the self-assembled monolayer has been included to investigate the effect of interface functionalisation. In all structures, a bi-layer dielectric of PMMA and SiO_2 has been employed. In this bi-layer, the PMMA provides a strong insulation layer and the SiO_2 provides surface inertness. All the layers, excluding the Au electrodes, were prepared using the same process parameters, and the thin films of the molecular semiconductor DNTT, were evaporated in a single process run. This was done to ensure that any differences observed in the films could be attributed to the devices geometries and not to thin film processing.

4.2.4 Initial results using SKPM

To begin the initial study of the DNTT OFET devices, a brief introduction into the types of device that will be studied is necessary. There are three distinct conformations of device structure that will be under investigation in this section of work. These are: top contact (TC) where the organic material has been laid directly on top of the insulating layer and the gold contacts are patterned on top, bottom contact (BC) in which the gold contacts are patterned onto the insulating layer of the device and the organic thin film is grown on top, and finally BC with a self-assembled monolayer (BC-SAM) wherein, as with BC devices, the contacts are laid down first, followed by the SAM and finally the organic thin film of DNTT. These conformations are shown in figure 4.2.

In order to investigate the effect of device structure a study of the topography of the device using tapping-AFM was undertaken. First the device was imaged such that the channel and part of each electrode was in view, this allowed us to visualise the macroscopic differences in each sample as can be seen in figure 4.3. From this raw data it is possible to visually discern a difference between the topography of each device geometry. In particular comparing the channel topography of the TC and BC configuration devices. The BC devices presents structural defects

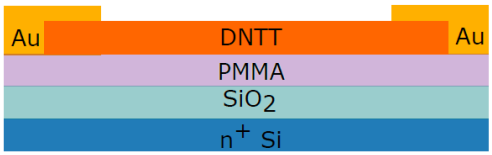

(a) Top contact

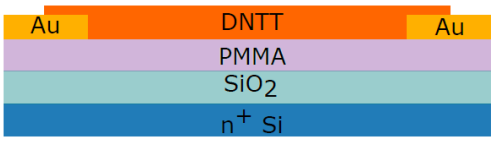

(b) Bottom contact

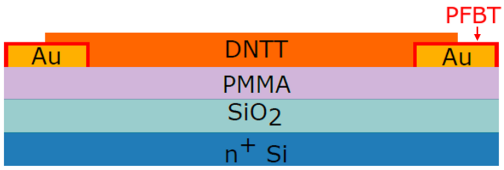

(c) Bottom contact with PFBT SAM

Figure 4.2: Geometries of fabricated DNTT OFET's devices

within the organic film, most clearly in the channel. These defects are particularly clear in the BC device without SAM. Another difference that is visible even at this larger scan size is the sharpness of the electrodes. For the TC device the electrodes are more clearly defined, the BC devices show a less defined electrode-channel edge however the addition of a SAM layer appears to mitigate this effect.

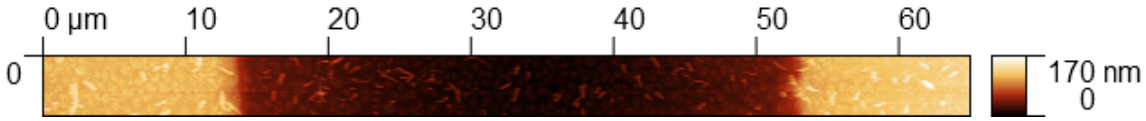

(a) Top contact - filename: 2016-12-09.000

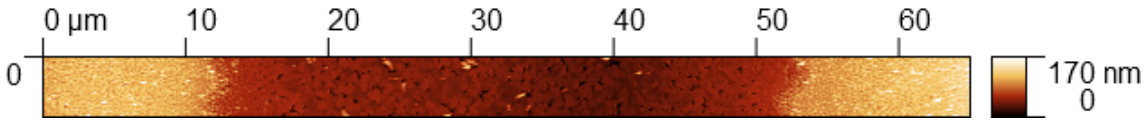

(b) Bottom contact - filename: 2017-01-13.000

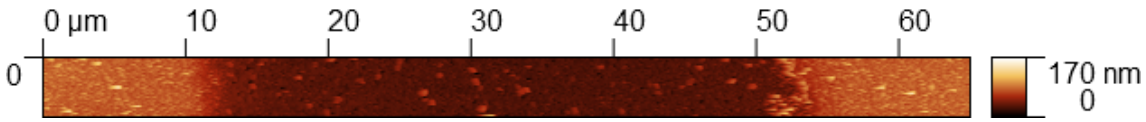

(c) Bottom contact with PFBT SAM - filename: 2017-01-13.014

Figure 4.3: Full 65 μm x 4 μm topographical images from tapping-AFM methods of TC, BC and BC-SAM DNTT devices.

Although differences in thin film structure may be observed at the macroscopic level of a full 65 μm scan, it is prudent to take a closer investigation; focusing on the channel material for each device structure. By comparing figures 4.4, 4.5, and 4.6 which show a representative 5 μm image for each device, It is possible to observe the structure of the film in the channel more closely.

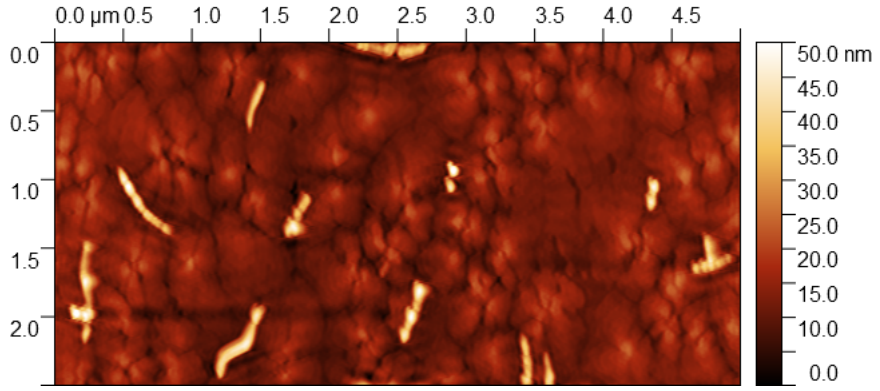

Figure 4.4: Tapping-AFM topography image of channel material for a TC DNTT OFET. 5 μm x 2.5 μm image.

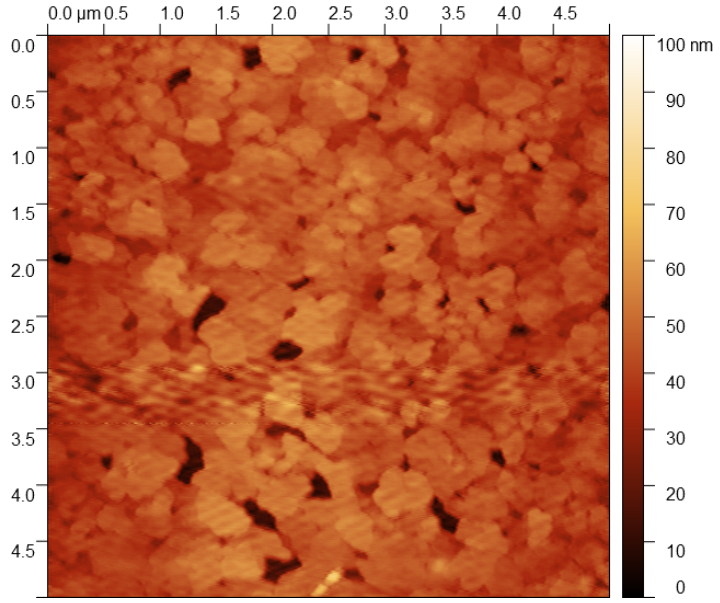

Figure 4.5: Tapping-AFM topography image of channel material for a BC DNTT OFET. 5 μm x 5 μm image.

It can be observed that the growth of the organic semiconductor is vastly different depending on the order of deposition. For the top contact device, large grain boundaries with lamellar edges have grown into a cohesive film. However for the bottom contact devices a much smaller grain size and a distinct lack of lamellar growth is observed. This may be due to a distortion in the organic material resulting in a more disordered film with smaller grain sizes than that of TC films. Furthermore, there are hole-like defects within the thin film structure, where the grains have failed to coalesce. In figure 4.6, the BC-SAM shows that the addition of the PFBT SAM layer partially mitigates the formation of these defects, but the grain size of thin film growth remains small. Although the overall focus of this study

is the electrode channel interface and its effect on contact resistance, the growth of the thin film, and subsequently any defects produced in the channel, may have an effect on the overall charge transfer that each device is capable of.

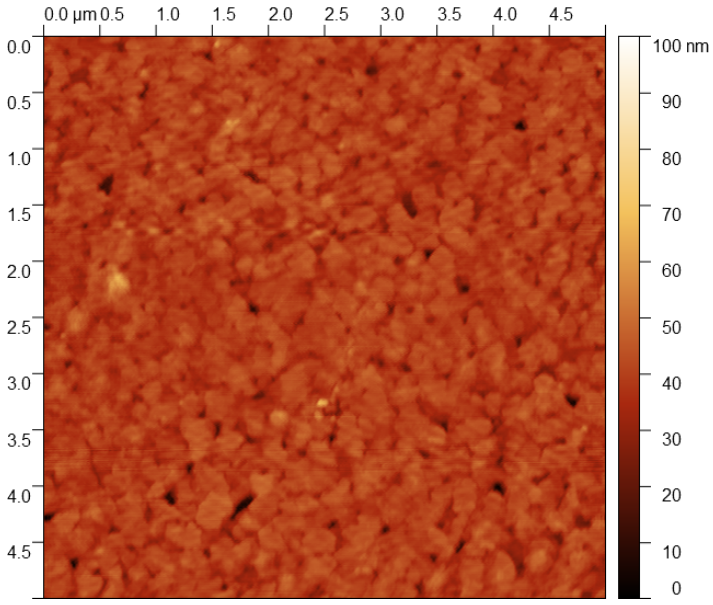

Figure 4.6: Tapping-AFM topography image of channel material for a BC-SAM DNTT OFET. 5 μm x 5 μm image.

Taking a closer look at the top contact structure, by selecting areas within a representative small scan size image (2 μm^2) and plotting the distribution of heights, the packing structure of the small molecule DNTT can be visualised. DNTT has a herringbone packing structure, the arrows shown on the peaks of the histograms shown in figure 4.7 represent the evidence for the existence of molecular terraces within a layered structure.

From this data it is obvious that the order in which the contacts are patterned and the thin film is grown is crucial to the structural formation of the DNTT layer. Further study into defect analysis of the thin films can be found in section 4.2.7. Now that the topography of the devices has been fully explored it is prudent to begin investigations of the electrostatic behaviour using scanning Kelvin probe microscopy (SKPM).

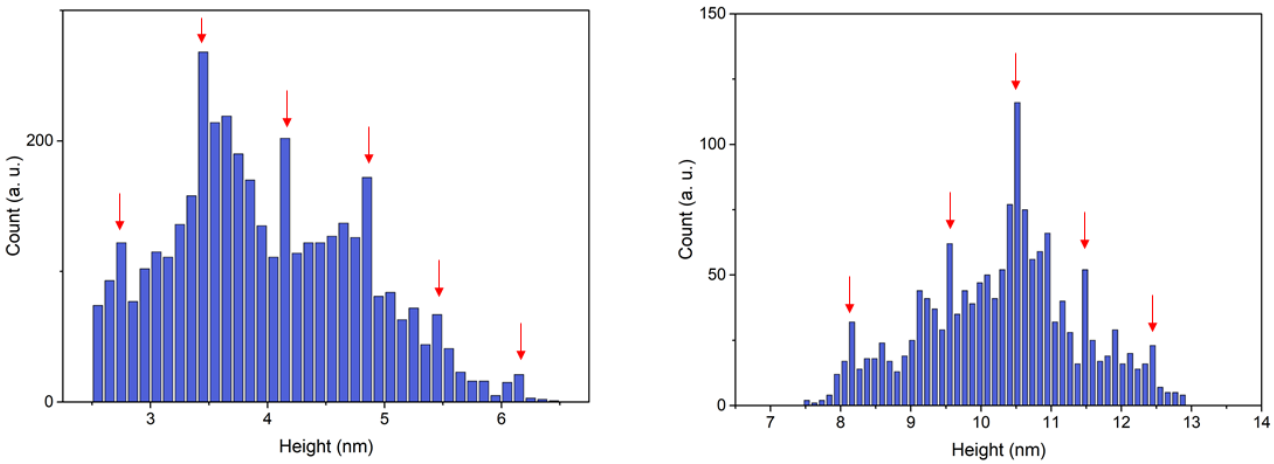

Figure 4.7: Histograms illustrating the presence of molecular layers/terraces within the thin film of a TC DNTT OFET device.

4.2.5 Scanning Kelvin probe microscopy studies

By utilising the powerful scanning tool that is SKPM it is possible to investigate the transistor samples under various conditions in a non-invasive manner. The specific aim of this is to observe the effect that sample structure has on the contact resistance, the potential drop between electrode and channel. The three sample conformations can be seen in figure 4.2. Using a Veeco Nanoscope III and Nanoscope extender with a J scanner attachment it is possible to take relatively large scale scans of the devices. Each device has a channel length of approximately 50 μm, so in order to include a portion of each electrode in the image a 65 μm scan size was used. Nanosensors POINTPROBE-PLUS EFM tips with an overall coating of $PtIr_5$ increases the electrical conductivity of the cantilevers, these cantilevers were employed for all EFM scanning presented in this work. The devices were electrically connected to the sample stage using a custom made sample holder. Each Si chip was cleaved such that four devices were available. Devices were then connected to the sample holder in pairs if possible, with a shared source contact.

To begin, a baseline of operation for the devices is established by subjecting each device to source-drain biases between V_{sd} = -0.25 V and V_{sd} = -8.00 V whilst maintaining a gate bias of $V_g = 0$ V. By operating the devices within this parameter space and using SKPM measurements to obtain two dimensional line profiles across the devices (as shown in figure 4.8) the local potential, as well as the work function

difference between the tip and the sample, are observed. Additionally this allows verification that the source-drain connections are operational and behaving as expected. Since DNTT is a hole transporting material, the drain contact is negatively biased and the source is grounded, in order to conduct holes from source to drain of the OFET devices.

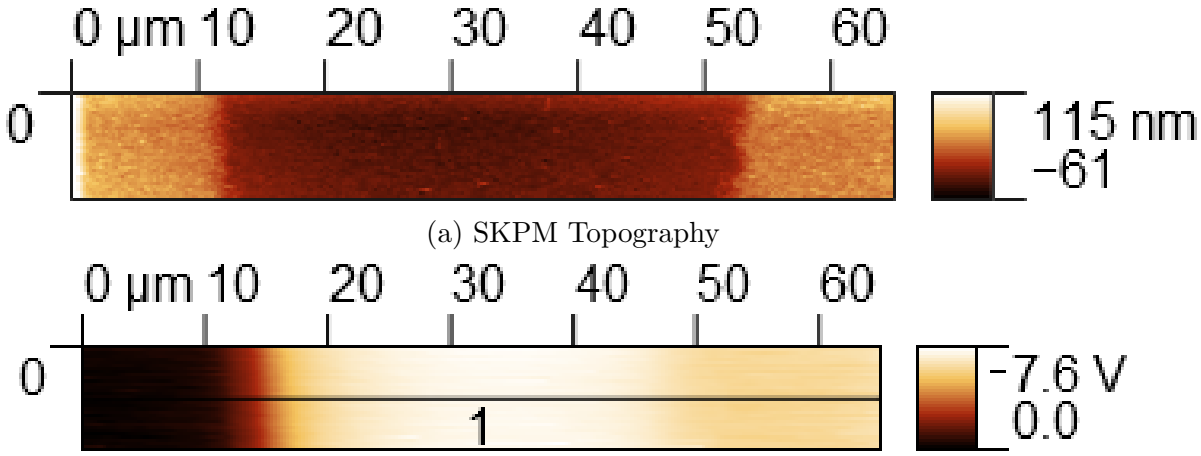

(a) SKPM Topography

(b) SKPM potential

Figure 4.8: An example of the selection of a two dimensional profile from a three dimensional SKPM image. In the example the image is from a BC device with an applied V_g = 0 V and V_{sd} = -6.00 V, filename: 2016-03-23.011. 65 μm by 4 μm image.

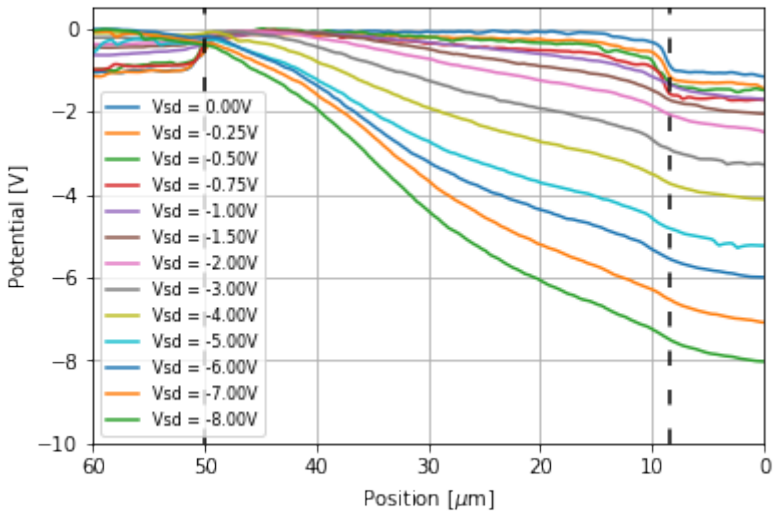

Figure 4.9: TC DNTT OFET device potential line scan data for varied source-drain bias with zero applied gate bias.

When there is zero gate voltage applied to the OFET device, no current flows between the source and drain electrodes. The device is said to be in an OFF state. It isn't until a non-zero gate bias is applied that charges are accumulated

at the dielectric-semiconductor interface, and the source drain bias forces charge carriers through the channel [112]. By observing the device in its OFF state, it is expected that no charge carriers will be observed in the channel region, and that the SKPM line profiles should show the local potential applied to the electrodes.

In figure 4.9, the line profiles obtained through SKPM show the potential across the device with a grounded source electrode and the expected applied drain bias over the drain electrode, although there is some discrepancy in the observed drain potential at the lower (V_{sd}<-2.00 V) applied biases.

However, in the channel of the device the behaviour is less easily explained. As previously stated, there should be few charge carriers in the channel of the device in the absence of a gate bias. The line profiles appear to show an approximately linear decrease in potential from the source to the drain electrode. At small source drain bias, the basin shape of the device is observed as expected. However increasing the source drain bias appears to affect the channel.

Another noteworthy observation with regards to these profiles is that increasing the drain bias significantly reduces the potential drop that is observed at the interface between the drain electrode and the channel.

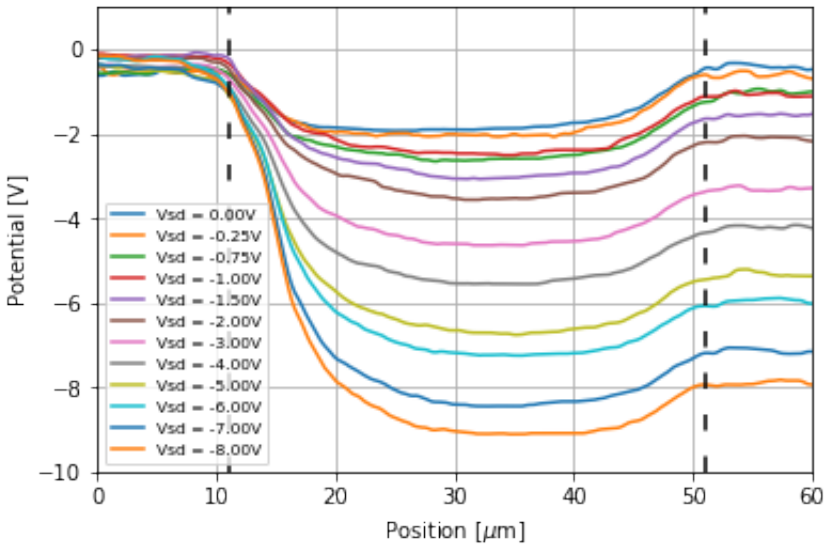

Figure 4.10: BC DNTT OFET device potential line scan data for varied source-drain bias with zero applied gate bias.

In figure 4.10 the SKPM line profile data for a BC device is presented. Again the device appears to be in good operation, with a well grounded source electrode and the bias above the drain electrode reading as what has been experimentally applied. As with the TC device, some discrepancy in the potential reading above the drain electrode at the lower (V_{sd} <-2.00 V) range of applied bias is observed, but this does not appear to have any observable effect on the operation of the channel or the device as a whole.

The most stark difference between figures 4.9 and 4.10 is the line profile behaviour in the channel. For the TC OFET a linear gradient across the whole device is observed, with the exception of a small drop at the electrode-channel interface which may be due to the the work function difference between tip and sample.

If we consider the case where V_{sd} and V_g are both zero for a TC device, there are no charge carriers in the accumulation layer of the device. Therefore in SKPM, the tip should be measuring purely the work function difference between the tip and the sample. For the PtIr tips: the work function of platinum is 5.12 - 5.93 eV [113], but from Bruker (a supplier of SKPM/EFM PtIr tips) a value of $\approx$ 5.5 eV, and for iridium $\approx$ 5.3 eV in air, is quoted [114]. The mixed material tips, in air, should have an approximate work function between 5.3 - 5.5 eV. Over the gold electrodes, the SKPM profiles show a potential of -0.5 V. The literature value for the work function of gold is given as 5.1 eV [115], but in practice (i.e. non-UHV conditions) this can be expected to be less: $\approx$ 4.9 eV [116]. The work function difference between tip and sample, over the gold electrodes is therefore expected to be between -0.4 and -0.6 V. This corresponds well with what is observed over the electrodes for the TC device in figure 4.9. Over the channel of the device, where the sample is DNTT whose ionization potential is given in literature as $\approx$ 5.4 eV [65], this implies that a contact potential difference of 0 - -0.1 V. This is also consistent with what is observed in figure 4.9.

For the BC device, where there is a thin layer of DNTT over the gold electrodes, it is expected that the contact potential difference should be 0 - -0.1 V across the entire device. This however, as can be observed in figure 4.10, is not the case. At zero V_{sd} and V_g, the profile shows a contact potential difference of $\approx$ -0.5

V over the electrodes, consistent with the work function of the Au electrodes rather than the DNTT thin over-layer. The observed value of -2.0 V in the channel is difficult to understand in that it does not correspond to the expected value from the DNTT ionization potential. The results obtained in the next experiment, wherein a non-zero V_{sd} and V_g is applied, produce a contact potential difference that is more in-line with what is expected.

The next step in the investigation is to apply a non-zero fixed gate bias exceeding that of the threshold voltage for the device (Which can be found in table 4.1), in the cases that follow that is an applied gate bias of V_g = -7.00 V. The application of the non-zero gate bias essentially polarises the dielectric causing charges to accumulate at the dielectric-semiconductor interface. The applied V_{sd} bias forces these accumulated charge carriers from the source electrode to the drain electrode where the current (I_d) can be measured.

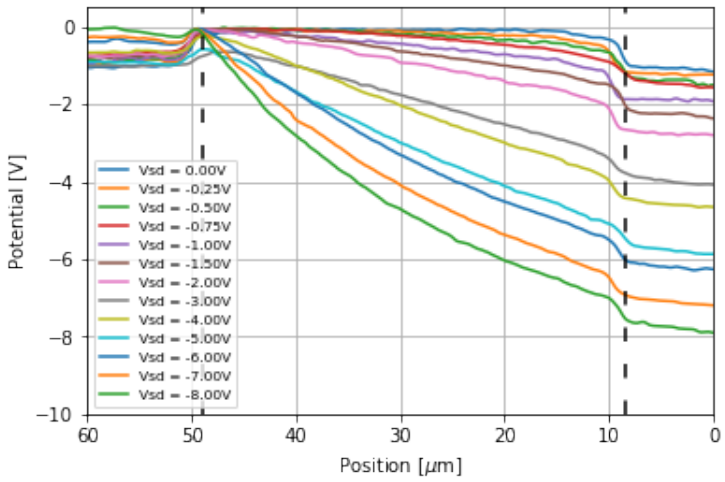

Figure 4.11: TC DNTT OFET device potential line scan data for varied source-drain bias with fixed non-zero applied gate bias - V_g = -7.00V.

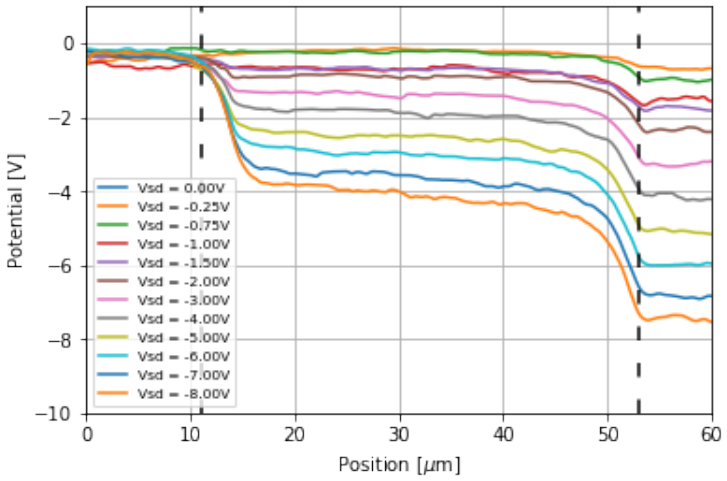

Figure 4.12: BC DNTT OFET device potential line scan data for varied source-drain bias with fixed non-zero applied gate bias - V_g = -7.00V.

Upon comparison of figure 4.9 with figure 4.11, and figure 4.10 to 4.12 a noticeable difference in device operation is observed.

For both device types it is observed that the potential drop at the electrode-channel interfaces is much greater upon the application of the non-zero gate bias. For the TC device the overall shape of the profiles is largely unchanged. Taking a more in depth look at the profiles however reveals that the transition from linear to saturation regime has been shifted from V_{sd} <-5.00V to V_{sd} = -6.00 V with device operation in saturation regime above V_{sd} = -6.00 V.

Another key difference between the potential profiles in figure 4.9 and figure 4.11 is the position in the channel at which the line profile goes from linear to super-linear. Where this was very clearly at 25 μm in figure 4.9, the application of the non zero gate bias has caused this to shift to 35 μm. This means that the super-linear drop of potential at the source channel interface has been reduced and the size of the region of channel after the pinch off point has been increased. This is because pinch-off occurs when V_g - V_{th} = V_{sd} and so as we have increased V_g pinch off occurs at higher V_{sd}.

In the case of the BC device the difference between figures 4.10 and 4.12 are much more obvious than that of the TC device. Starting at the source-channel interface a significant drop in potential is still observed, however it occurs over

approximately 3-4 μm compared to the initially observed 10 μm. Whereas for -8.00 V_{sd} with an applied -7.00 V_g a drop of 3V in the first 10 μm of channel is observed.

It is possible to qualitatively link the shape of the two dimensional potential profiles to the local charge carrier concentration. As the current at each point in the transistor is constant, the local potential drop must scale, approximately, with local resistance. From Ohm's law: $J = \sigma E$ where J is the current density, σ is the conductivity, and E is the electric field. Provided any local changes in the channel are ignored, it is shown that the local conductivity (σ) is approximately inversely proportional to the local electric field, E, which in SKPM methods is represented by the gradient of the potential profile. With this in mind, regions of steep gradient in the profiles are indicative of a low carrier density whereas a higher carrier density is implied at the shallower gradient regions.

After this initial potential drop, the channel region between 15 and 45 μm shows a linear potential profile and no longer exhibits the basin like shape potentially caused by the work function difference of electrode and channel. This implies that there are now charge carriers present in this region of the channel and they are likely screening the work function difference. In the channel region from 45 μm up to the drain electrode, the device exhibits a second potential drop of a similar magnitude to the first. Therefore the potential drop across the electrodes is the same as without an applied gate bias, but spread over the two electrode-channel interfaces allowing for the charge carriers to pass through the channel. In figure 4.12 also included is a potential profile for $V_{sd} = 0$ V, this shows that the application of the non-zero gate bias in the absence of a source drain bias still exhibits the basin shape, i.e. showing only the effect of the work function difference and no charge carriers.

The final step in this experimental investigation is to observe the device in operation for a fixed source-drain bias, in this case V_{sd} = -7.00 V, over various gate biases $V_g = 0$ V to V_g = -20.00 V in 2.00 V increments. This allows for the visualisation of the effect that increasing the gate bias has on the charge transfer of the device and final confirmation of device operation. Here it is once again possible to observe the transition of device operation from linear to saturation regime, as we go from $V_g \ll V_{sd}$ to $V_g \gg V_{sd}$.

The charge density in the channel, as well as I_d are modulated by the magnitude of the electric field applied via the gate electrode. This is where the term 'field-effect' originates. By observing the effect of changing the magnitude of V_g, it should be possible to observe the change from linear to saturation regime.

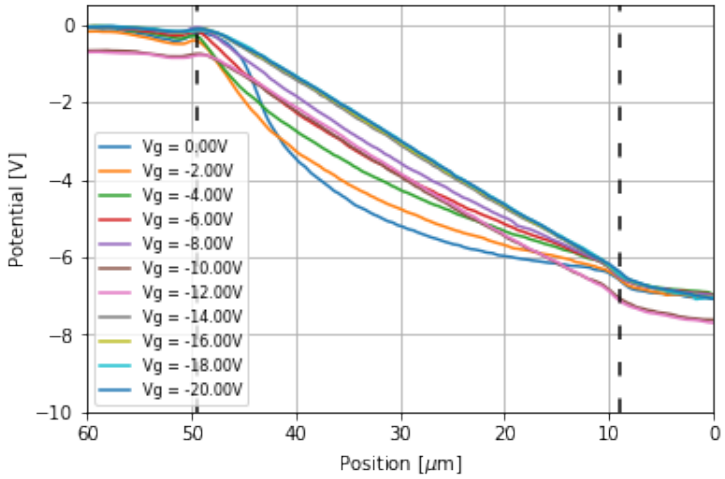

Figure 4.13: TC DNTT OFET device potential line scan data for varied gate bias with fixed non-zero applied source-drain bias - V_{sd} = -7.00 V.

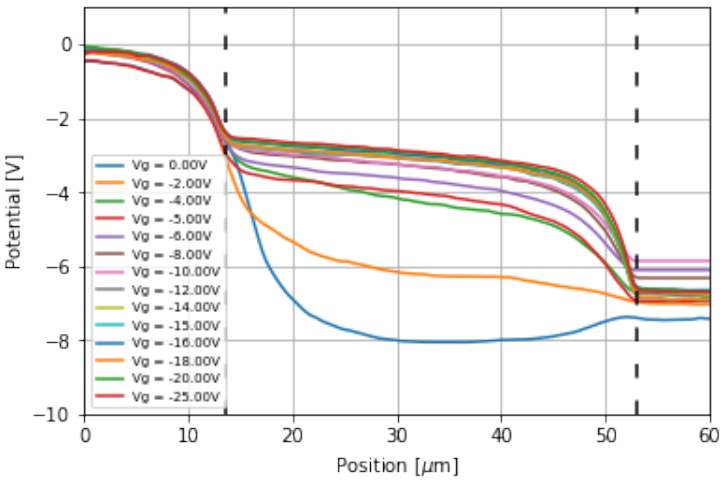

Figure 4.14: BC DNTT OFET device potential line scan data for varied gate bias with fixed non-zero applied source-drain bias - V_{sd} = -7.00 V.

In figure 4.13 the progressive transition between linear to saturation regime is observed. In order to have device operation in the saturation regime, a $V_{sd} \geq V_g$ - V_{th} must be satisfied, therefore for small V_g (V_{th} to -8.00 V) and V_{sd} of -7.00 V device operation is within the saturation regime. Once V_g is sufficiently large, such

that $V_g \gg V_{sd}$, the transistor device will operate in the linear regime, this is shown in figure 4.13 as profiles from -14.00 V_g to -20.00 V_g.

This same trend is present in figure 4.14 for the BC device. Once again, at zero applied gate bias, the basin shape that has been previously discussed is present, and as the device is shifted to more negative gate biases (from -2.00 V to -10.00 V) potential profiles show the device operating in the saturation regime. At V_g >-10.00 V the two dimensional profiles show the transition to a linear gradient demonstrating operation in the linear regime.

What sets the BC device apart from the TC OFET is the potential drop at the electrode channel interfaces. In figure 4.14 the conditions for the channel to contain sufficient charge carriers is observed. If a comparison is made between the profiles for V_g = 0V and V_g = -2.00 V the effect of the application of a non-zero gate bias is clear.

Now that an overall understanding of device operation over various bias settings has been obtained, the parameter space can be narrowed down to better observe the behaviour of the contact potential difference. As previously mentioned the profiles produced from SKPM data represent the cumulative effect of the local potential in the accumulation layer of the device and the work function difference between the tip and the sample. In order to remove the contribution from the work function difference a profile for the device operating under 0 V_{sd} and 0 V_g must be subtracted from all subsequent profiles. Therefore local potential can be freely observed. Figure 4.15 shows an example of this for a single profile. Included is the measured profile (in orange), the profile for both zero applied source-drain and gate bias (in green), and the resulting profile when green is subtracted from orange (in blue).

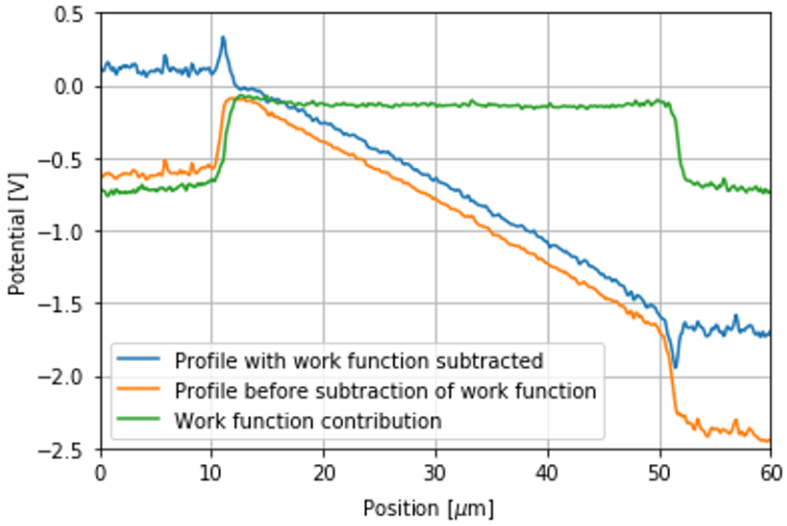

Figure 4.15: An example of subtracting the SKPM measured work function between tip and sample to obtain the local potential in the accumulation layer. This graph shows a TC device where the applied potential is V_{sd} = -2.00 V and V_g = -30.00 V.

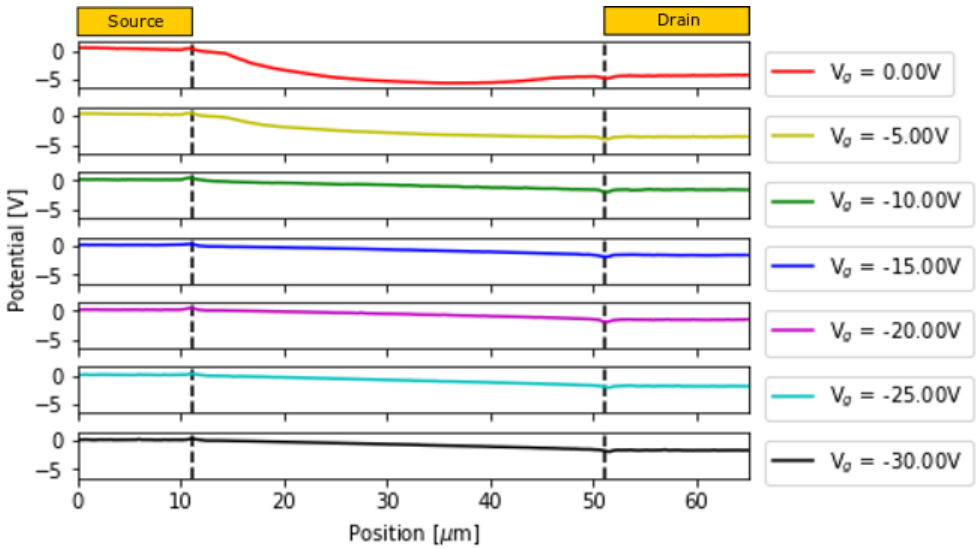

Figure 4.16: Separated potential profiles with work function removed for TC device for a fixed V_{sd}= -2.00 V. Gate bias is stepped in 5.00 V increments from 0.00 V_g to -30.00 V_g. Profiles have been separated in the y-axis to allow for ease of viewing.

By comparing figures 4.16 and 4.17 there is a clear difference in contact resistance at the electrode-channel interface between TC and BC DNTT OFET devices. For the TC device, there is little to no potential drop observed at the electrode-channel interface. There is a small peak observed in the data, however this may be an artefact from the scanning that has been carried through the potential data scans as the tip moves from the gold electrode to the semiconducting material, an artefact from the analysis method or perhaps (if we take this to be a true feature)

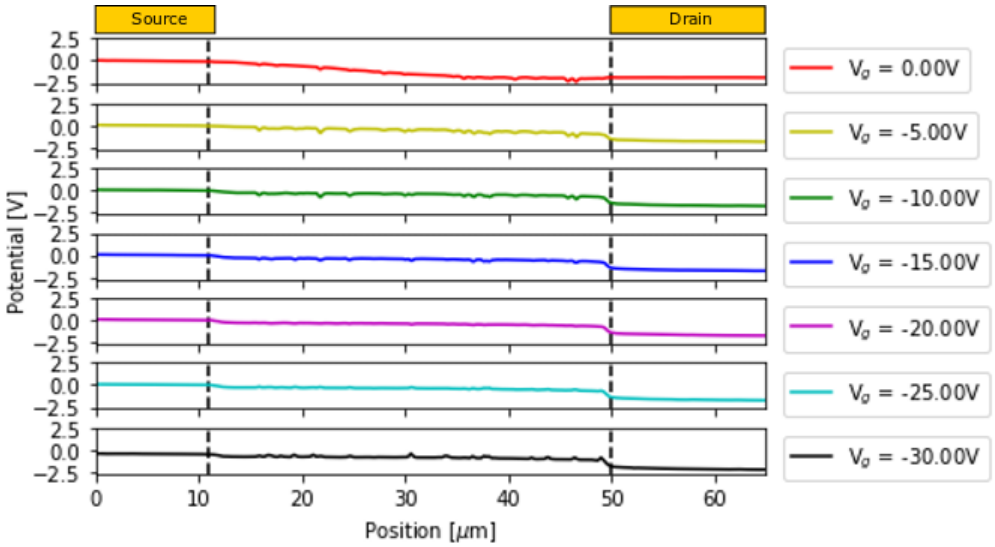

Figure 4.17: Separated potential profiles with work function removed for BC device for a fixed V_{sd}= -2.00 V. Gate bias is stepped in 5.00 V increments from 0.00 V_g to -30.00 V_g. Profiles have been separated in the y-axis to allow for ease of viewing.

indicative of a low carrier density in these regions. Given that these artefacts are more clear in the line profiles for the BC device, especially in the channel of the transistor, as the structure of the organic material is less well formed than for the TC device the hypothesis that the artefacts are from large topographical differences is most likely. The defects in the channel of the BC devices will be explored in further detail in section 4.2.7.1.

If a focus is placed solely on the channel-drain electrode interface, it is clear that the BC device is exhibiting a much larger potential drop than the TC device. At the source electrode-channel interface, it is also observed that the BC has a much more defined drop than the TC device, but additionally this potential drop becomes more pronounced as the gate bias is increased.

Although it is well known that TC devices have a better performance, many transistor devices are still formulated with a BC structure due to ease of engineering. It is much easier by far to deposit organic material over pre structured electrodes than it is to deposit electrodes on top of a, very often, highly sensitive organic semiconductor. Therefore we seek to find a structure that will somewhat mitigate the effects of this large contact resistance. Here we show that the addition of a SAM of PBFT, henceforth a BC-SAM device, deposited onto the gold electrodes

before the addition of the organic semiconducting material.

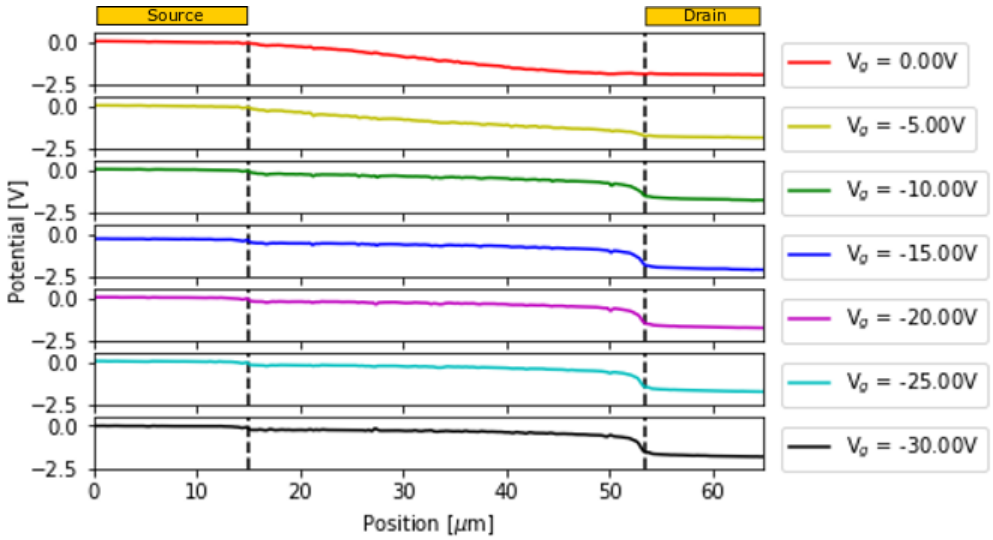

Figure 4.18: Separated potential profiles with work function removed for BC-SAM device for a fixed V_{sd}= -2.00 V. Gate bias is stepped in 5.00 V increments from 0.00 V_g to -30.00 V_g Profiles have been separated in the y-axis to allow for ease of viewing.

Surprisingly, in this data, the addition of the PFBT SAM layer to the devices does not show the desired effect of mitigating the contact resistance and visually follows the same trend that the BC devices were observed to follow. The most striking difference from a direct comparison of figure 4.17 to figure 4.18 is the behaviour over a line scan in the channel of the device. The significant troughs caused by the defects formed during the growth of the semiconductor are almost completely removed with the addition of a SAM. This will be investigated in further detail in section 4.2.7.2.

4.2.6 Conclusions from SKPM analysis of DNTT OFET devices

In general, the process of isolating contact resistance from other variables requires hundreds of devices assumed to be identical and trap free. Here, by utilising SKPM methods it has been possible to extract, using only a single device, the contact resistance of an OFET device in a non-invasive procedure. Not only is the contact resistance obtained, but further analysis allows a more precise and experimentally

backed value of charge carrier mobility in the organic semiconductor layer to be obtained. This method has the potential to be applied across the field of organic and thin film semiconducting materials, as a simple and non-intrusive method for obtaining charge carrier mobility.

4.2.7 Defect analysis of organic material

As has been previously introduced, the BC and BC SAM type devices contain defects in the organic material layer. To be certain that the observed defects are structural holes in the material, measurements of potential at the defect sites were compared to background potential of the film at a constant source-drain bias of -2.00 V_{sd}. In order to obtain a comprehensive view of the effects of the defects, four defect sites were selected from each large area scan. By taking the potential data scan from the SKPM studies and measuring the potential at each defect for each gate bias between V_g = 0.00 V and V_g = -30.00 V an image can be built up of the behaviour of the defects.

4.2.7.1 BC devices

The BC device is operated at a source drain bias of V_{sd} = -2.00 V. By comparing the topography data with the potential data collected using SKPM, four defects were selected across the device as can be seen in figure 4.19. A plot of the potential for each of these defect sites with respect to gate bias is then produced in figure 4.19.

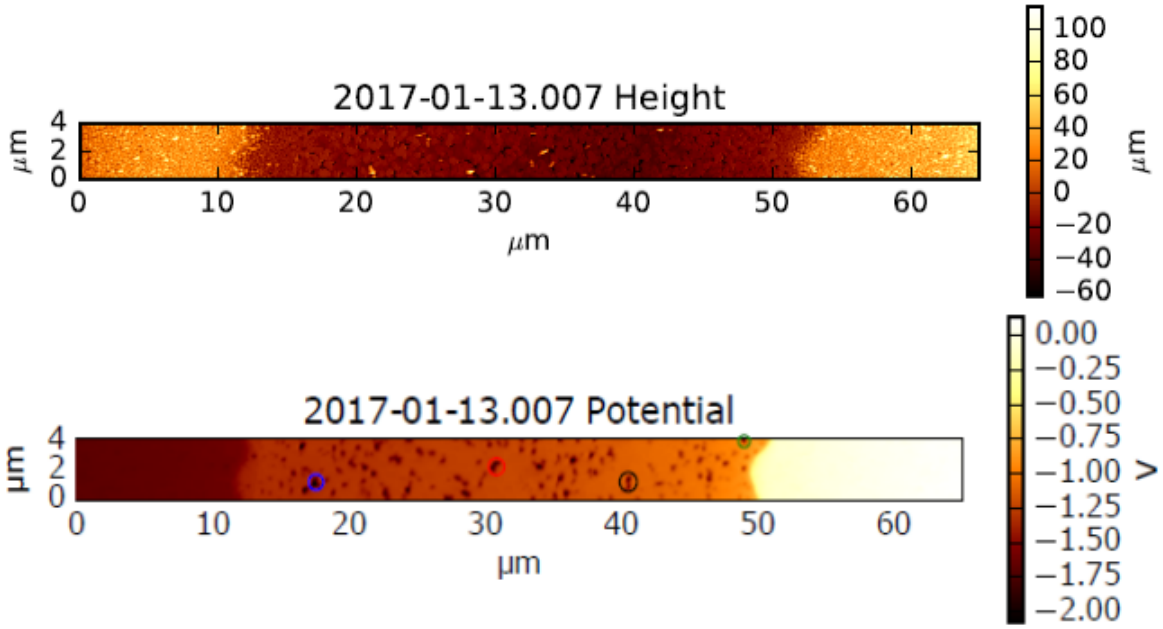

Figure 4.19: Topography and potential SKPM data for BC DNTT OFET device, with selected defects at V_{sd} = -2.00 V and V_g = -30.00 V. 65 μm x 4 μm image.

The potential at each defect is plotted in figure 4.20. This plot is then separated into individual defects to compare the potential directly above the defect to areas near to the defect site and background thin film potential. This can be found in figure 4.21.

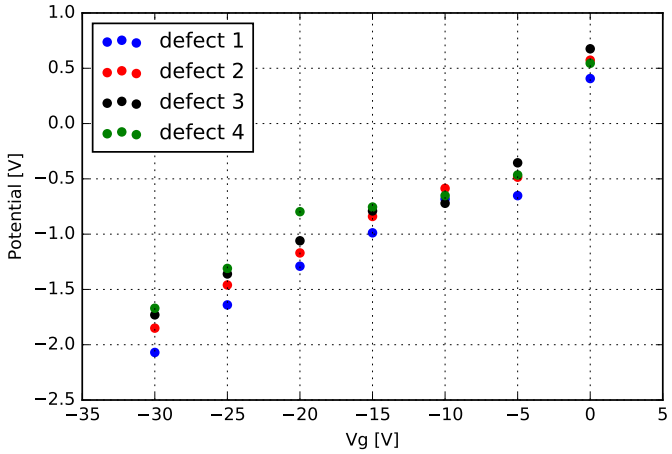

Figure 4.20: A plot of measured potential against gate bias at each defect site for a BC DNTT OFET device at -2.00 V_{sd}. 65 μm x 4 μm image.

From figure 4.20 the measured potential within the defect is shown to be more negative for more negative gate bias. The potential measured within the defect does not match the applied gate bias, which could imply that the defects within the thin film are only on the very surface of the material and do not extend entirely through to the gate dielectric. However as SKPM measurements are based on a long-ranged Coulombic interaction, there may be some screening effect from the defect free surrounding material which may affect the results. As such it is not possible to rule out the possibility that these defects do indeed penetrate through the entirety of the thin film.

Figure 4.21 shows the potential measured within the defect compared to background thin film and areas surrounding the defect. It can be observed that the defect has little to no effect on the potential of the area directly surrounding it, as this follows the potential observed for the background thin film. As the gate bias is increased above -20.00V the potential measured within the defect becomes more negative than the measured background.

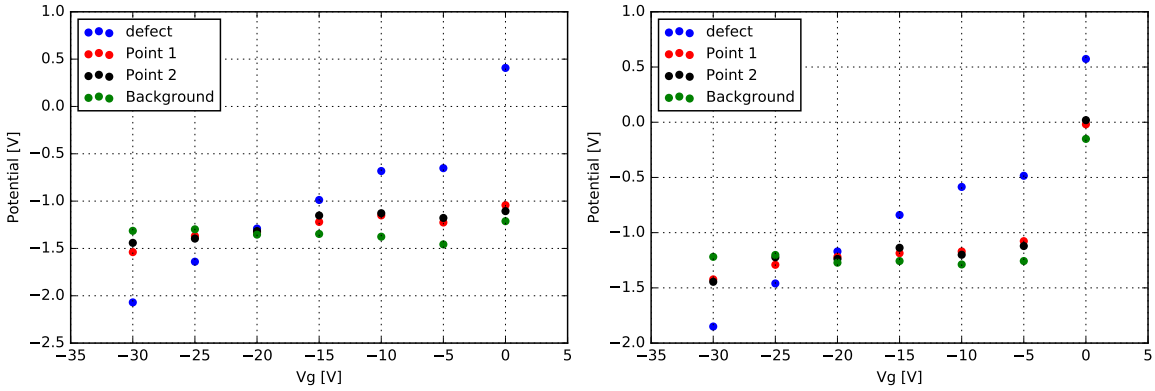

(a) Defect 1

(b) Defect 2

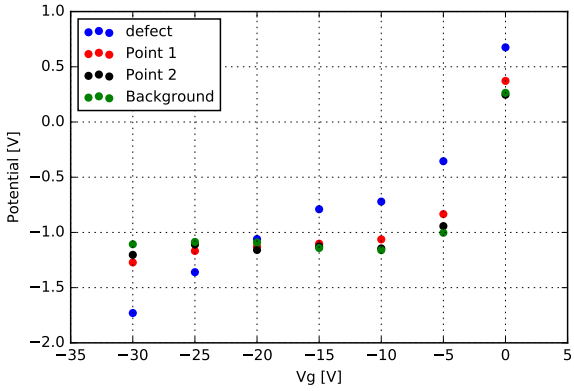

(c) Defect 3

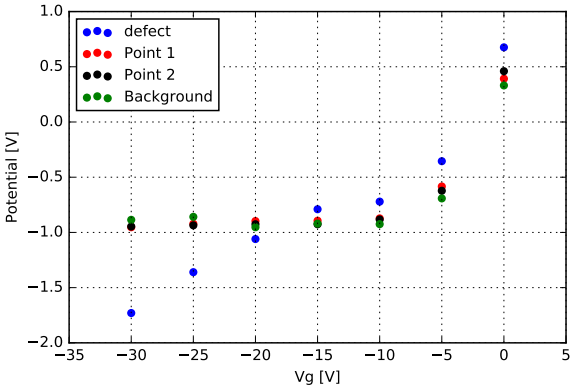

(d) Defect 4

Figure 4.21: Defects and surrounding areas compared to background: Potential versus gate bias for BC DNTT OFET device. The blue points denote the potential reading within the defect, the red and black points denote potential data from areas close to the defect, the green points denote a background reading taken on the same X coordinate as the defect.

4.2.7.2 BC-SAM

The experiment is now repeated for the BC-SAM devices. It is known from the morphological study that the defects appear to be less pronounced with the addition of the SAM. This further study should confirm our previous results and show that by adding a SAM to the BC devices, we can mitigate growth defects. The defect sites are chosen as with the BC device and can be found in figure 4.22

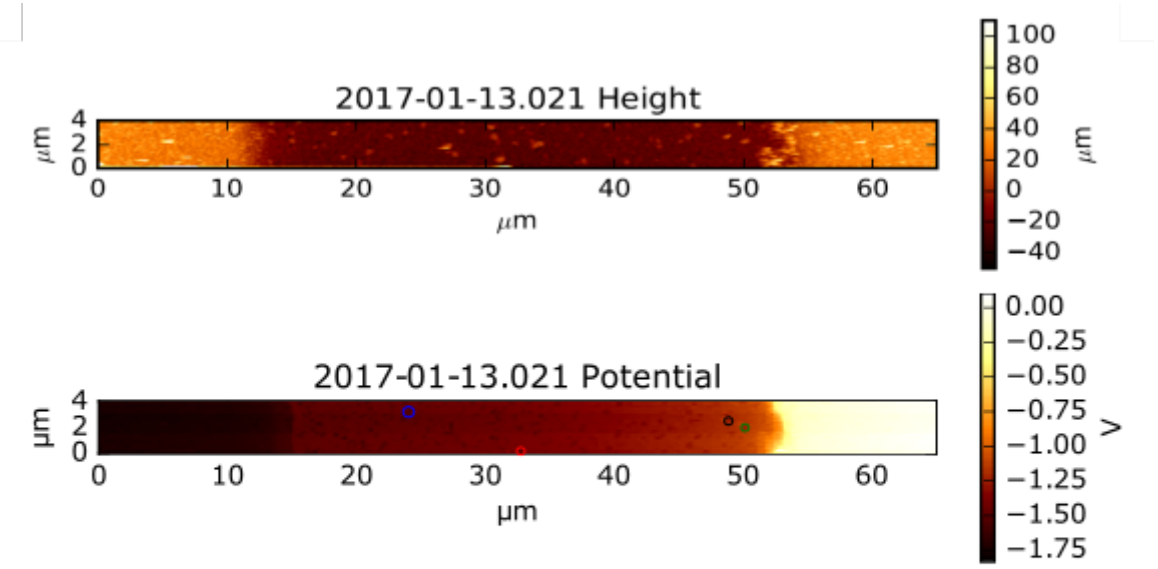

Figure 4.22: Topography and potential SKPM data for BC-SAM DNTT OFET device, with selected defects at V_{sd} = -2.00 V and V_g = -30.00 V. 65 μm x 4 μm image.

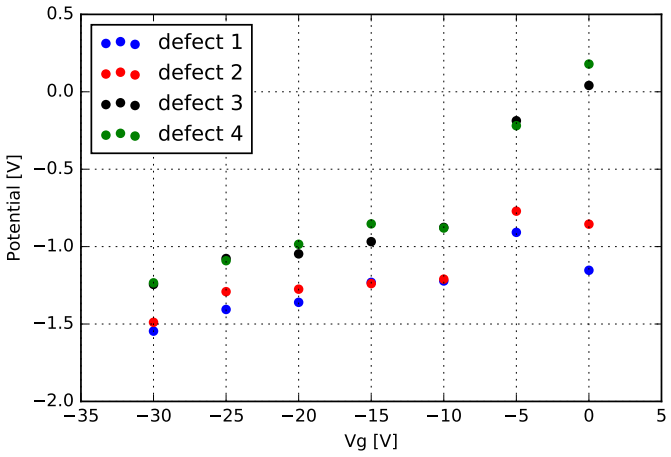

Figure 4.23: A plot of measured potential against gate bias at each defect site for a BC-SAM DNTT OFET device at -2.00 V_{sd}. 65 μm x 4 μm image.

Figure 4.23 shows the potential measured within the defect from SKPM data. Comparing this to figure 4.20 that the potential reading within the defect is less negative. The potential still scales with gate bias, but to a lesser degree. This implies that the defects are less pronounced after the addition of the SAM.

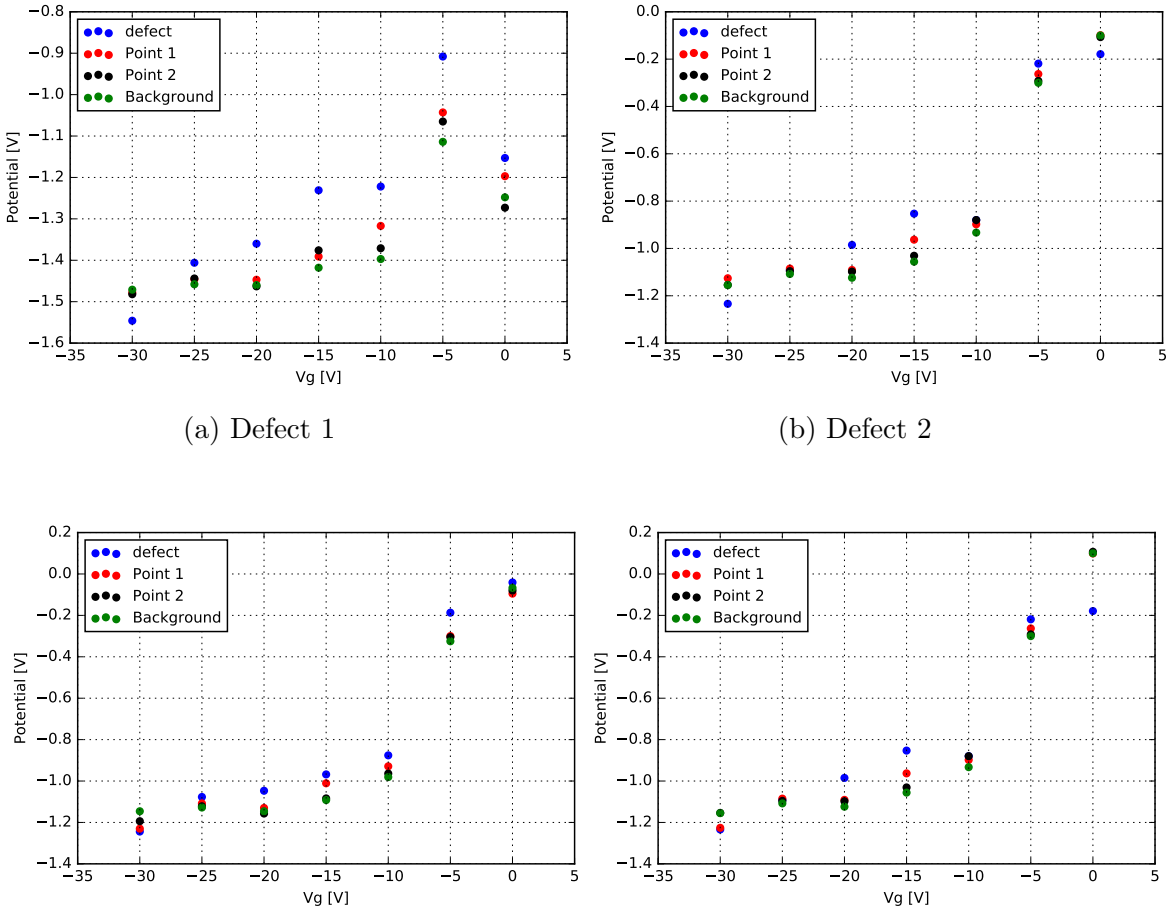

(a) Defect 1

(b) Defect 2

(c) Defect 3

(d) Defect 4

Figure 4.24: Defects and surrounding areas compared to background: Potential versus gate bias for BC-SAM DNTT OFET device.

In figure 4.24 the background, and areas surrounding the defect are compared to the potential of the defect. The behaviour of the potential of the defect follows very well the behaviour of the background and near by areas, different from the BC device. Once again it is possible to state that the defects do not seem to affect the areas surrounding them. It is therefore possible that the defects within the BC-SAM device are less pronounced, or perhaps are not as deep lying within the thin film.

4.2.7.3 Conclusions from defect analysis

By using SKPM methods to observe the potential within and around perceived defect sites for BC and BC-SAM devices at a constant source-drain bias of -2.00 V and varied gate bias, it was possible to analyse the effect of the SAM addition to

the defect formation in the thin film. In the BC device, the measured potential at the defects become more negative with gate bias, and at gate biases greater than -20.00V the measured potential at the defects is more negative than the surrounding area. The addition of the SAM mitigates this effect and the potential of the defect is shown to closely follow that of the background thin film. The conclusions of this may be that the addition of the SAM layer causes the defects formed within the thin film to be less deep into the organic layer. From topographical studies it has also been observed that the addition of the SAM results in less frequent and smaller diameter defects. This may play a non-negligible role in the performance of the devices. It is however not possible to make a detailed interpretation of these results due to the degree of uncertainty with regards to the nature of the interactions.

4.2.8 Parameter extraction

By combining produced SKPM data with transistor data provided by Dr Chang-Hyun Kim, it is possible to extract a variety of parameters for each transistor device. As has been observed in previous sections of this chapter, for TC devices the potential applied to the OFET is dropped across the channel (V_{ch}), with negligible drop at the electrode-channel interface (V_c). However, in the case of BC and BC-SAM devices the potential drop across the OFET is a combination of V_{ch} and V_c.

A plot of linear transfer characteristics was produced for each device from data provided by Dr Kim for transistors with measurements of: channel width (W) 500 μm, channel length (L) 50 μm and unit-area capacitance (C) 10.8 nFcm^{-2}, as is shown in figure 4.25. For these plots, current measurements (I_d) are taken across a sweep of gate voltages (V_g) from 10.00 V to -30.00 V. The first parameter that may be extracted from this data is the threshold voltage. By differentiating the linear transfer data using a Savitzky Golay filter (derivative 2) the threshold voltage for each device type is obtained. The values for V_{th} derived from this data can be found in table 4.1. It is also possible to obtain values for I_d at distinct V_g values from these plots which can be combined with V_{ch} values extracted from the SKPM potential profile data as the potential drop across the transistor channel. This allows

the calculation of R_{ch}, the 'intrinsic' resistance of the OFET channel which is then used to calculate the intrinsic mobility, μ_{ch}, using the equation

$$\mu_{ch} = -\frac{1}{R_{ch}} \times \frac{L}{WC(V_g - V_{th})}. \tag{4.1}$$

The results of this equation are dependent on V_g and V_{th} and as such a mean value for the device is presented in table 4.1. In the case of the BC and BC-SAM devices the potential drop across the channel as measured using SKPM methods in the case of V_d = -2.00 V is between approximately -0.35 V and -0.70 V for BC devices and 0.40 V to 0.55 V for BC-SAM (with the exception of V_g = -5.00 V, where the potential dropped across the channel is significantly higher in the BC-SAM case). In the case of the TC device, a negligible potential drop is observed at the contacts and hence we assume that $V_{ch} \approx V_d$ = -2.00 V.

The next parameter that may be extracted from the linear transfer data is the linear mobility of the device given by the equation

$$\mu_{lin} = -\frac{dI_d}{dV_g} \times \frac{L}{W} \times \frac{1}{C} \times \frac{1}{V_d}. \tag{4.2}$$

This parameter can be derived directly from the linear transfer characteristics data, without the SKPM potential profiles.

Now taking data obtained from operating the device in the saturation regime of operation across a sweep of gate voltages from 10.00 V to -30.00 V (figure 4.26), it is possible to extract the saturation mobility (μ_{sat}) of each device. The equation for μ_{sat} is given by:

$$\mu_{sat} = \left(\frac{d\sqrt{-I_d}}{dV_g}\right)^2 \times \frac{2L}{W} \times \frac{1}{C} \tag{4.3}$$

and as with μ_{lin}, this method allows the mobility to be calculated solely from the saturation regime data and does not require the SKPM potential profiles. This method of mobility extraction once again produces lower values than when the μ_{ch} approach is taken.

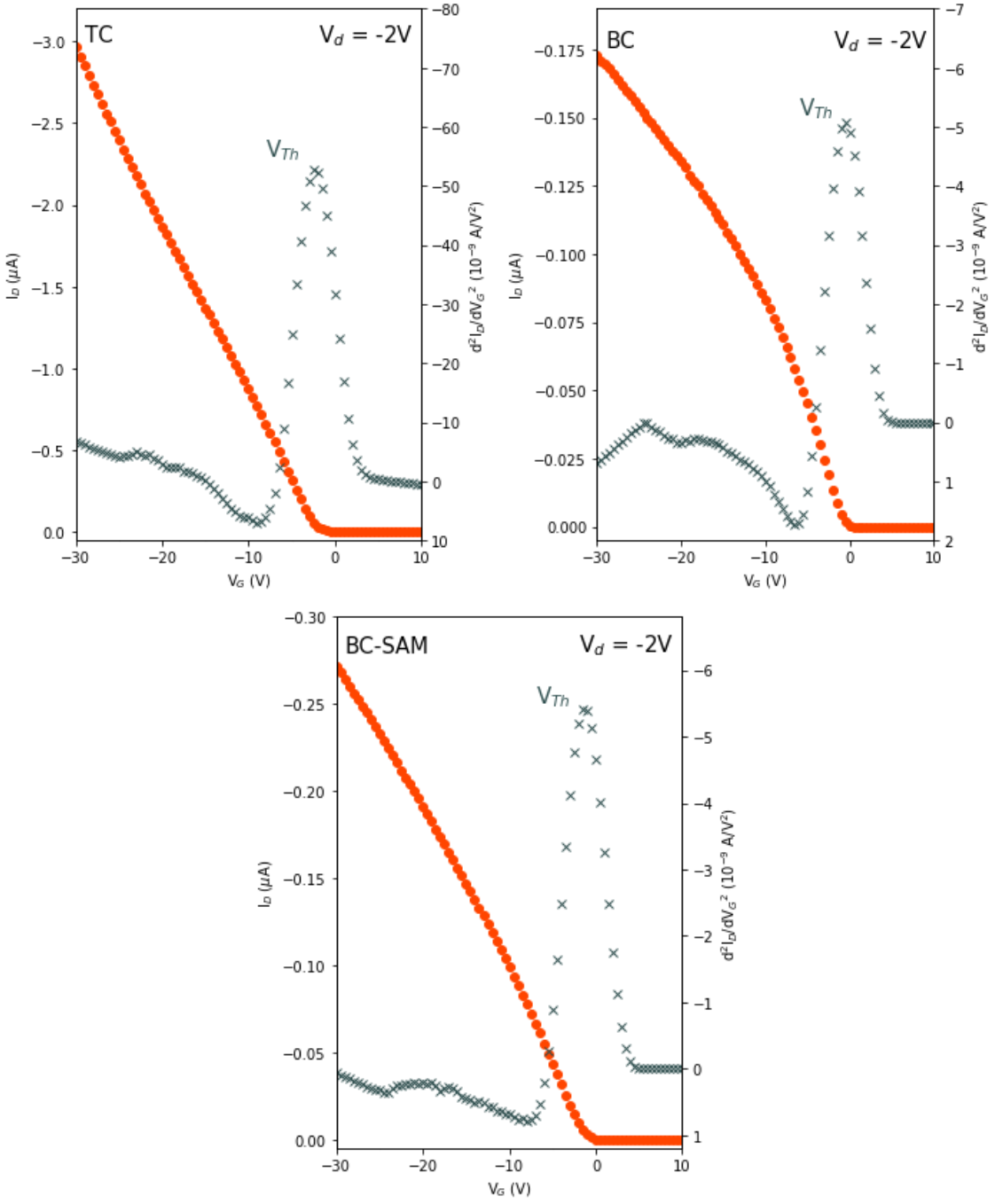

Figure 4.25: Plotted data from the linear regime of operation for TC, BC and BC-SAM DNTT OFET devices, along with second derivative (blue crosses) to determine threshold voltage.

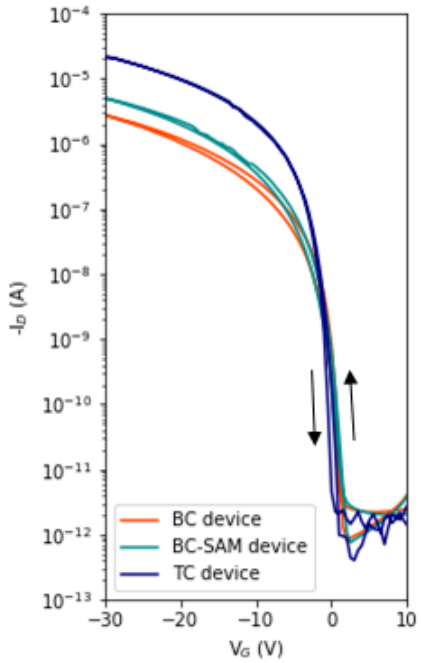

Figure 4.26: A plot of saturation regime data for TC, BC and BC-SAM DNTT OFET devices for source drain bias of -30.00 V.

The data provided by operating the transistor devices in the saturation regime is also useful as an aggregated performance indicator. The results of which demonstrate the small hysteresis of the devices as well as high quality switching. The data also evidences the turning on of the device close to V_g close to zero.

It is clear from this data that the method by which the parameters of the OFET devices are extracted has a non-negligible affect on the extracted OFET mobility. If the potentiometrically verified value of μ_{ch} is assumed to be correct, then it can be said that the extracted linear and saturation mobilities grossly underestimate the device mobility as is shown in figure 4.27.

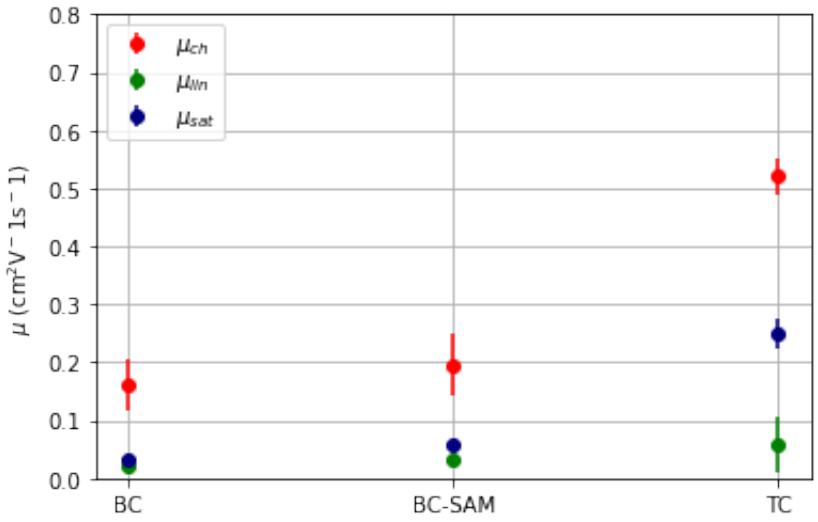

Figure 4.27: A comparison for value of charge-carrier mobility calculated by different methods for each device.

As both the BC and BC-SAM devices exhibit a potential drop at the electrode-channel interface it is possible to draw comparisons between the size of the contact resistance and its relation to gate voltage for each device. In order draw comparisons between the two samples, the modulation of the width normalised R_c values were plotted against the effective overdrive voltage (V_g - V_{th}) which is directly proportional to the accumulated charge density allowing the samples to be compared on a common physical basis. The results of this can be found in figure 4.28 which shows the addition of the SAMs to the device results in a reduction in R_c.

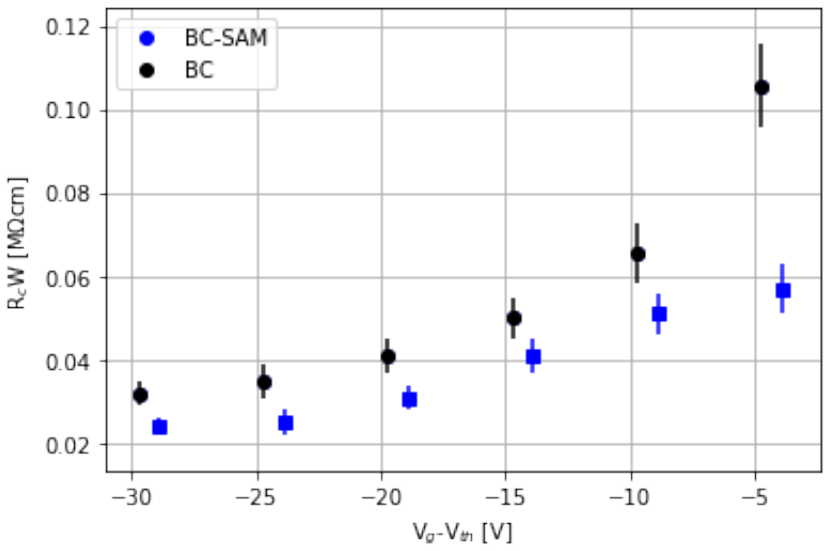

Figure 4.28: Width normalised contact resistance against effective overdrive voltage for BC and BC-SAM DNTT OFET devices.

Device conformation	V_{th} [V]	μ_{ch} [cm^2/Vs] *	μ_{lin} [cm^2/Vs]	μ_{sat} [cm^2/Vs]
BC	-0.28	0.161 ± 0.045	0.02 ± 0.003	0.032 ± 0.003
BC-SAM	-1.1	0.195 ± 0.053	0.031 ± 0.004	0.058 ± 0.006
TC	-2.2	0.52 ± 0.03	0.34 ± 0.05	0.25 ± 0.03

Table 4.1: Threshold voltages and mobilities, calculated through the methods described above, for the three device configurations of the DNTT OFET devices. * the values for μ_{ch} are mean values.

In 4.1 above, it is observed that the addition of the SAMs to the BC device increases not only the threshold voltage of the device, but also the intrinsic, linear operation, and saturation operation mobilities. It was determined that the SAMs promoted the tight packing of DNTT therefore enhancing transport of charge carriers [65]. However, the TC device still presented the highest mobilities across all calculation methods. By reducing the contact resistance in BC devices, it is hoped that the sharp carrier-density bottleneck may eventually be overcome.

4.2.9 DNTT study conclusions

Through SKPM and AFM methods, an in depth study of DNTT OFET devices was performed. The effect of the device configuration was explored in relation to: potential profiles, contact resistance, defect formation, and carrier mobility. By taking potential line scans from SKPM potential data for varied gate and source-drain biases, a comprehensive view of the behaviour of the transistors was obtained. Using AFM methods to obtain topographical data in the channel of each device conformation showed the formation of defects within the thin film of both bottom contact transistors. For the top contact devices large, dendritic grains formed lamellar edges growing into a cohesive film, whereas in each of the bottom contact conformations, smaller grains which failed at times to merge were observed.

Using the obtained potentiometric data combined with transfer characteristics for each device (provided by Dr Chang-Hyun Kim), the mobility of the organic film was calculated. Three variations of this value were calculated: one using linear regime transfer data only, one using saturation regime transfer data only, and

finally one using the potentiometric data to obtain values for channel and contact resistance. It was shown that the values obtained solely from the transfer characteristics significantly underestimate the mobility of the thin film, as is evidenced by the mobility value obtained through experimental data which is greater in the case of each device.

The mobility values calculated for these devices look low when compared to literature values of similar devices. Hofmockel [117] presents mobilities between 8.5 cm^2/Vs and 1.3 cm^2/Vs using an alkylated derivative of DNTT in thin film transistors which, unlike DNTT, can be solution deposited and have a higher maximum effective mobility. Sigma Aldrich quotes a mobility of 3 cm^2/Vs for DNTT and a mobility of $\approx$ 7.9 cm^2/Vs for the alkylated derivative C_{10}-DNTT for TC device structures [118]. The the disparity between the literature values and the values calculated in table 4.1 may be due to testing in ambient conditions, or perhaps defects or non-idealities in the thin films.

The small molecule DNTT is just one of the emerging materials for organic thin film transistor devices. There are many organic semiconductors currently showing potential under testing conditions. However DNTT OFET devices exhibit an extremely stable thin film, even in ambient conditions, and (when grown before electrode deposition) a homogeneous and pin-hole free thin film. Other semiconducting materials in the same class as DNTT, such as BTBT and DATT also exhibit similar mobilities [118], and may be good contenders for OFET devices.

4.3 Organic semiconductor blend thin film transistors

4.3.1 Introduction to Organic semiconductor blends

Although small molecule semiconductors have provided very high field-effect mobilities and are well known for their high crystallinity, issues arising from device-to-

device variation due to morphological anisotropies lead to difficulties in processing over large area substrates [119, 120]. This coupled with poor processing from a solution-phase has lead to a shift in research from purely small molecule to small molecule:polymer blends. Blending together organic small molecule semiconducting materials with polymers allows for the creation of a thin film that gains the high electrical performance typical of small molecule films, as well as the superior solution processing qualities that polymers possess. Within this chapter, two such blends are studied.

The first blend combines an acene small molecule organic semiconductor (OSC) 2,8-difluoro-5,11-bis(triethylsilylethynyl)anthradithiophene (diF-TES-ADT) [121, 122] with the amorphous p-type polymer poly(triarylamine) (PTAA) to produce the blend dif-TES-ADT:PTAA which was first introduced in 2009 by R. Hamilton et al [123], the chemical structures for which can be found in figure 4.29. The highest mobilities obtained in this study were reported as a saturation mobility of (2.4 ± 0.05) $cm^2V^{-1}s^{-1}$ and a linear mobility of (1.88 ± 0.04) $cm^2V^{-1}s^{-1}$. Also reported, was the consistence and reproducibilty of key characterisation parameters, over the whole sample.

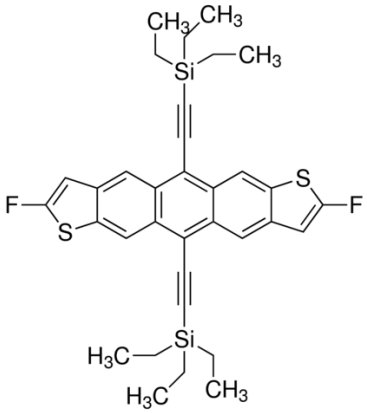

(a) dif-TES-ADT.[124]

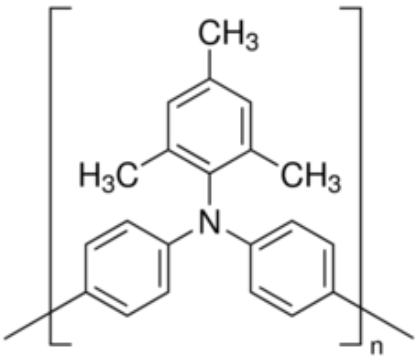

(b) PTAA. [125]

Figure 4.29: Chemical structures for the organic p-type semiconductor dif-TES-ADT and the amorphous p-type polymer PTAA which make up the first OSC:polymer blend devices.

The second OSC:polymer blend is a third generation hole transporting organic blend semiconductor first presented in 2016 by A. F. Paterson et al [126]. The combination of the small molecule 2,7-dioctyl[1]-benzothieno3,2-b][1]benzothiophene (C_8-BTBT) with the polymer binder indacenodithiophene-benzothiadiazole (C_{16}IDT-BT) resulted in solution processed OTFT's with hole mobilities in the excess of 13 $cm^2V^{-1}s^{-1}$. The selection process for each blend is quite intricate. In the case of C_8-BTBT:C_{16}IDT-BT the small molecule OSC was selected due to its high solubility in a variety of organic solvents coupled with its ability to form large inter-molecular overlaps which arise from well-ordered molecular arrays [127, 128]. The polymer binder was chosen primarily due to its high hole mobility (3.6 $cm^2V^{-1}s^{-1}$) and good solubility, as well as displaying a HOMO level comparable to that of the small molecule OSC (-5.15 eV and -5.04 eV respectively).

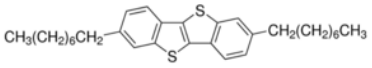

(a) C_8-BTBT. [129]

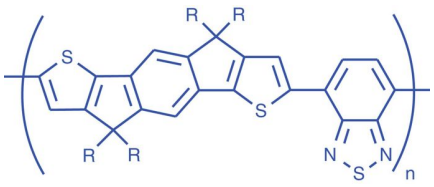

(b) C_{16}IDT-BT. [127]

Figure 4.30: Chemical structures for the small molecule C_8-BTBT and the polymer binder C_{16}IDT-BT which make up the first OSC:polymer blend devices.

The samples provided here were produced by colleagues in the department of Physics and Centre for Plastic Electronics Imperial College London, who published their work on these samples in 2018 [130]. For the purpose of the study presented here, the devices produced vary slightly from the initial design reported by the original developers. A substrate of silicon was cleaned by sonication in a detergent solution (DECON 90) and rinsed with DI water. Gold (Au) source and drain electrodes of 40 nm thick were deposited with a channel length of 60 μm. In order to modify the surface of the gold electrodes the samples were submerged in 5 x 10^{-3} mol L^{-1} of pentafluorobenzene thiol (PFBT) in isopropanol for 5 minutes before rinsing with pure isopropanol. To deposit the OSC:polymer blend, the solution (1:1 by weight at 4 wt % concentration of solids in tetralin) was spin coated onto the substrates. Spin-coating was performed at 500 rpm for 10 s the 2000 rpm for 20 s, followed by drying at 100 °C for 15 minutes in nitrogen in order to obtain layers of approximately 70 nm thick.

Deposition of the OSC:polymer blends by spin coating as described above has been shown to cause vertical-phase separation of the two material components which results in a polycrystaline surface layer rich in small molecules, which exhibits high mobility on top of a polymer-rich bulk which acts as a binder [131, 119, 132]. The segregation of the small molecules in the blend to the exposed interface of the device leads to the formation of large crystals within the channel region. This unique micro-structure has been shown to reduce the energetic disorder in the channel material through the formation of conductive grain boundaries [133].

For each OSC blend, a sample where the material is doped with Tris(pentafluorophenyl)borane known as BCF, whose molecular structure is shown

in figure 4.31, and a pristine (undoped) sample are studied. The purpose of this exploration is to investigate the differences in electrostatic behaviour for each OSC:polymer blend device, and also to probe the effect of the BCF dopant to the thin film. To do this, AFM and SKPM methods were employed to image the surface topography and potential respectively of each device.

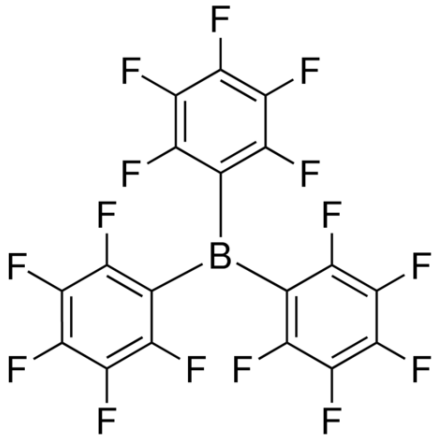

Figure 4.31: The molecular composition of the small molecule dopant Tris(pentafluorophenyl)borane also known as Perfluorotriphenylboron (BCF) [134].

4.3.2 Scanning Kelvin probe microscopy of OSC:polymer blends

To begin this study, the surface topography of each of the OSC:polymer blend devices was explored using AFM methods.

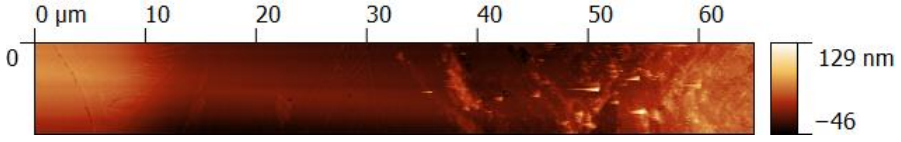

Figure 4.32: Topographical data for pristine dif-TES-ADT:PTAA device - filename: 2017-09-15.023. 65 μm x 8 μm image.

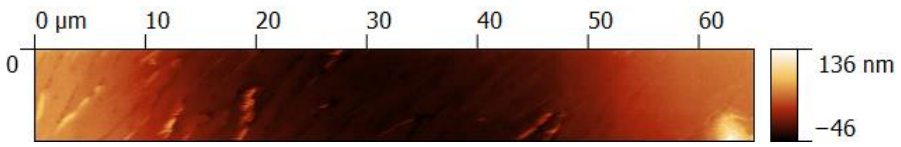

Figure 4.33: Topographical data for dif-TES-ADT:PTAA device doped with BCF - filename: 2017-10-16.022. 65 μm x 8 μm image.

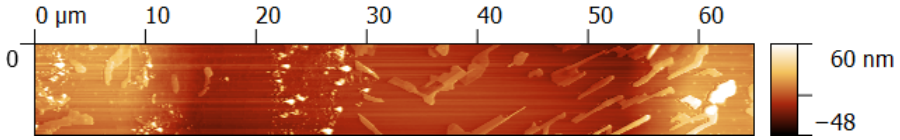

Figure 4.34: Topographical data for pristine C_8-BTBT:C_{16}IDT-BT device - filename: 2018-01-25.001. 65 μm x 8 μm image.

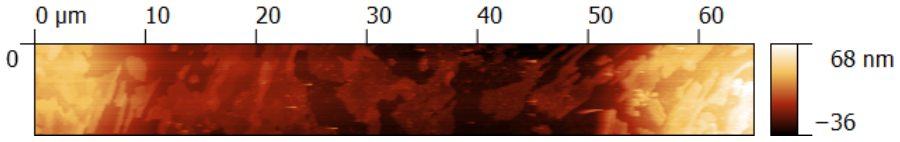

Figure 4.35: Topographical data for C_8-BTBT:C_{16}IDT-BT device doped with BCF - filename: 2018-01-25.014. 65 μm x 8 μm.

The electrostatics of the device were then probed, by taking potential data as with the DNTT samples: varying the gate for different source-drain biases. However using this method the data obtained made it clear that little further information about the sample could be gained from potential line scans. It appears that only at a significant source drain bias will be sufficient to create any significant difference to the device, as gate bias is modulated, that can be observed through the comparison of potential line profiles. However SKPM is limited in that data can not be collected at a surface potential any greater than 10 V, and the image will saturate at this level. Figure 4.36 show the potential line scan data for the pristine dif-TES-ADT:PTAA sample and is representative of the behaviour of the BCF doped dif-TES-ADT:PTAA sample as well as the pristine and doped C_8-BTBT:C_{16}IDT-BT devices.

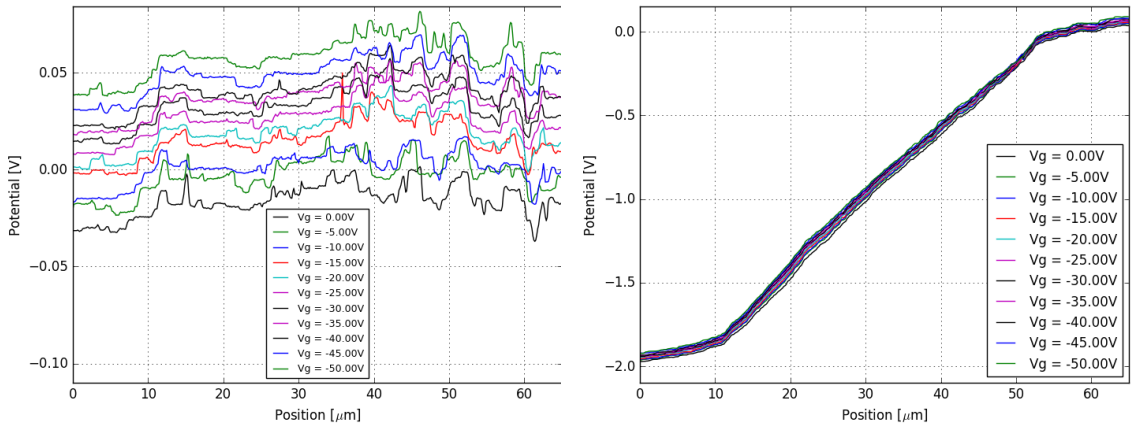

(a) 0V$_{sd}$

(b) -2.00V$_{sd}$

(c) -7.00V$_{sd}$

(d) -15.00V$_{sd}$

Figure 4.36: Potential profile line scans for pristine dif-TES-ADT:PTAA devices for fixed source-drain bias and varied gate bias.

Since little further information could be gained from the potential line scans, further study of the potential images was undertaken. By taking the first and second derivative of the potential data with respect to the distance along the channel, x, it became clear that the blended material showed areas of interest in the channel material where large crystals have inter-grown.

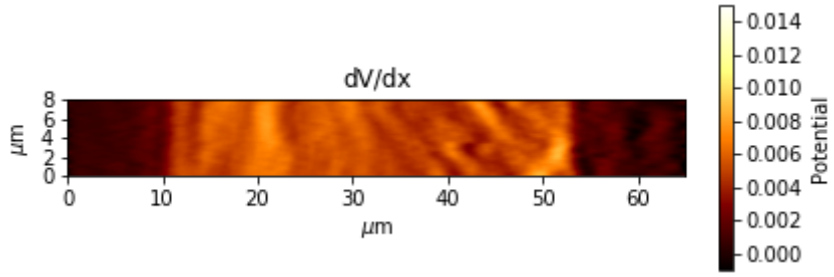

(a) First derivative of pristine sample

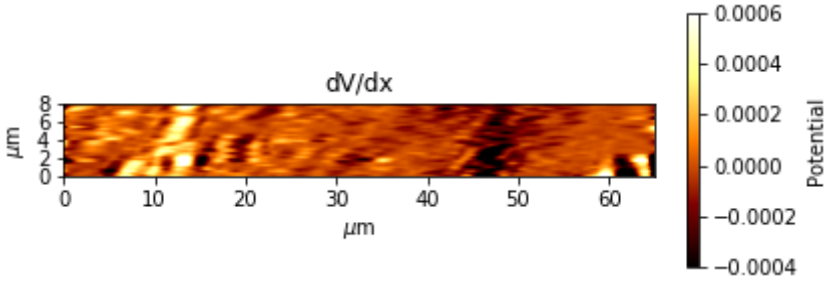

(b) First derivative of doped sample

Figure 4.37: First derivatives of potential data for pristine and doped dif-TES-ADT:PTAA OFET devices. 65 μm x 8 μm image.

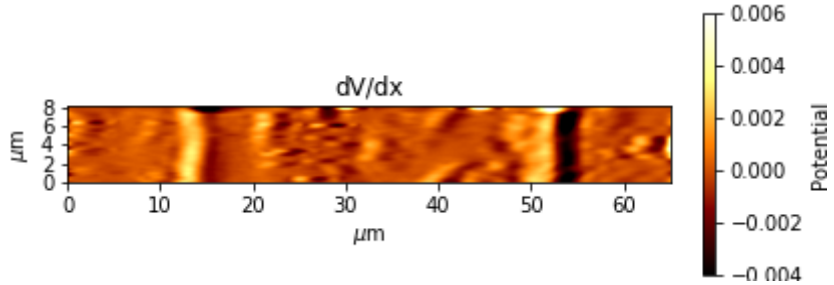

(a) First derivative of pristine sample

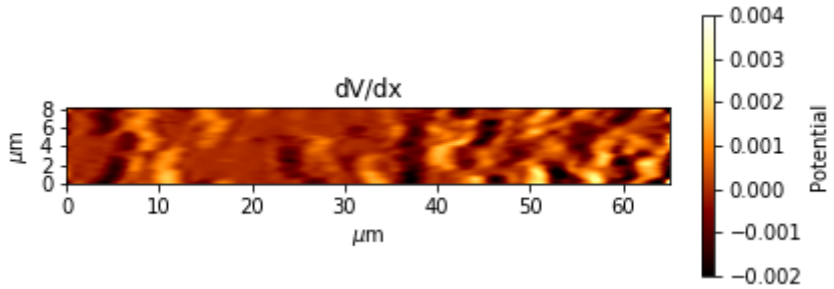

(b) First derivative of doped sample

Figure 4.38: First derivatives of potential data for pristine and doped C_8-BTBT:C_{16}IDT-BT. 65 μm x 8 μm image.

As can be observed in figure 4.37 and 4.38, by taking the first derivative of the potential data taken using SKPM methods, it is possible to recover some information regarding the structure of the OSC:polymer blend in the channel of the device. It is possible to further this study into the surface electrostatics by taking the gradient of the magnitude of the potential at each point of the recorded potential data allowed an image to be formed of the behaviour of the channel material. From this data it can be observed that the regions in which the grains are overlapping to form ridges are highly resistive. It is important to note that each of these SKPM images was taken with a V_g = 0 V and a V_{sd} = -2.00 V, so as to obtain carriers in the channel and optimise imaging.

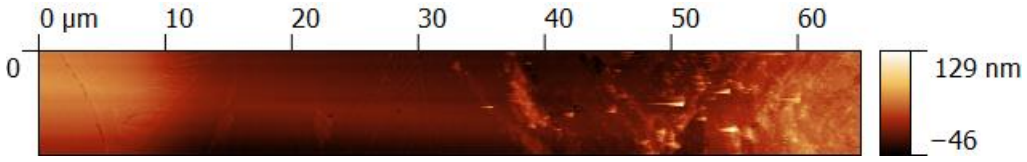

(a) Pristine dif-TES-ADT:PTAA topography from AFM methods

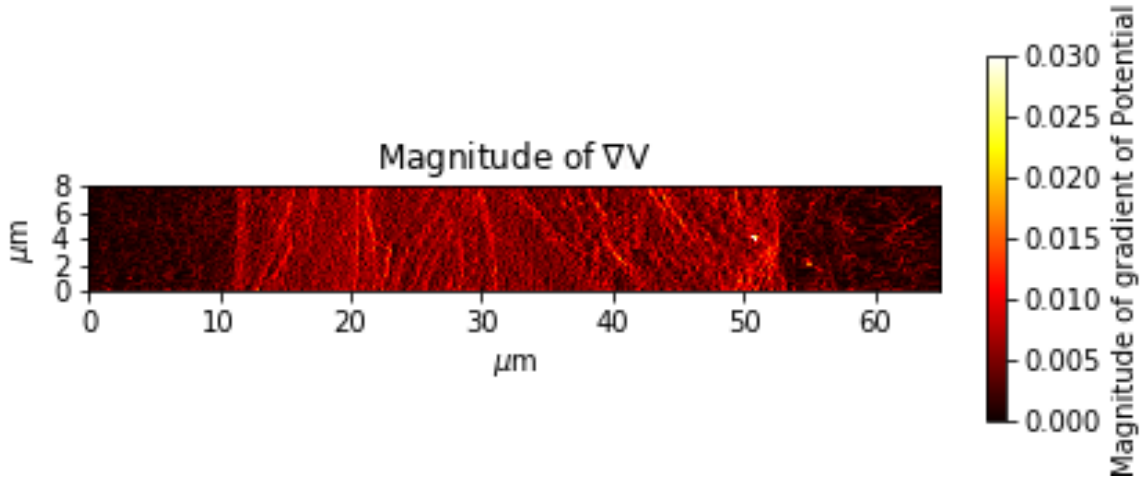

(b) Magnitude of the gradient of the potential for a pristine dif-TES-ADT:PTAA OFET from SKPM methods.

Figure 4.39: Comparison of topography to map of magnitude of the gradient of the potential for a pristine dif-TES-ADT:PTAA OFET device. 65 μm x 8 μm image.

The magnitude of the gradient of V was taken using the numpy gradient function within Python. This method calculates the gradient of the array, V, using second order accurate central differences in the interior points and either first or second order accurate one-sides (forward or backwards) differences at the boundaries [135]. As such the returned gradient has the same shape as the input array and hence, can be plotted as a gradient map as seen in figure 4.39.

Comparing the topography image to the image created by taking the magnitude of the gradient of the potential, it is possible to obtain a greater understanding of the thin film of OSC:polymer blend and how the formation of the blended material influences the device characteristics. An initial concern was that the topographic features would contaminate the SKPM images (cross-talk). However when the two images are studied side by side (as can be seen in figure 4.39), although some similarities can be observed there is a much greater level of detail in the differentiated potential map. If attention is focused on the left electrode (from 0 - 12 μm) there is a 'crease' in the topography that is not present in the differentiated potential map. The most stark contrast is perhaps in the region from 35 μm to 65 μm, where the topography shows significant in-homogeneity in comparison to the rest of the image. This is not present in the differentiated potential map. It may also be observed that the dif-TES-ADT:PTAA forms differently over the gold electrodes than over the channel, and that the analysed image shows the effect of the electrode-channel interface on contact resistance where a resistive area of material is shown.

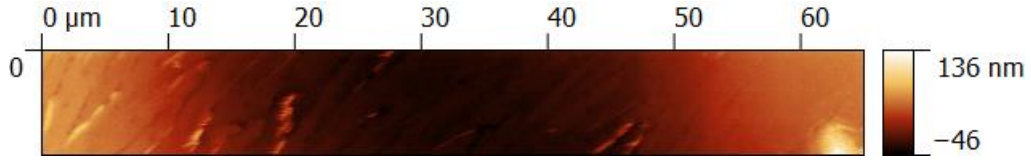

(a) dif-TES-ADT:PTAA doped with BCF topography from AFM methods.

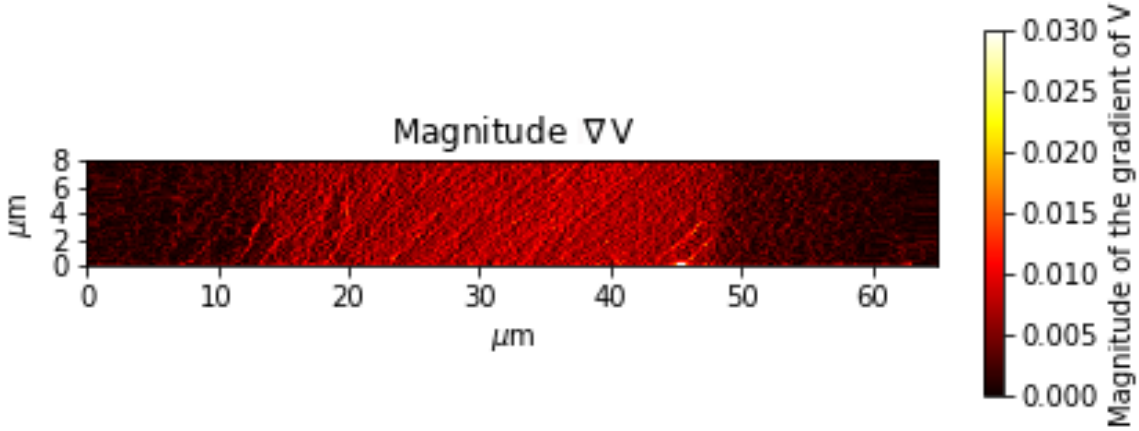

(b) Magnitude of the gradient of the potential for a BCF doped dif-TES-ADT:PTAA OFET from SKPM methods.

Figure 4.40: Comparison of topography to map of magnitude of the gradient of the potential for a BCF doped dif-TES-ADT:PTAA OFET device. 65 μm x 8 μm image.

This comparison between topography and magnitude of the gradient of the potential was then repeated for the doped dif-TES-ADT:PTAA sample. In figure 4.40 it is clear that the addition of the BCF dopant to the OSC:polymer blend has an effect on the formation of the thin film. More ridges are observed in the channel, but the formation of the thin film over the electrodes appears unchanged. Furthermore the highly resistive areas at the electrode-channel interfaces seem to be removed with the addition of the dopant. This implies a better carrier mobility in the device as the resistivity of the material is decreased.

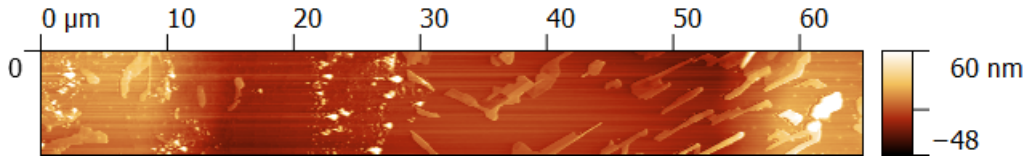

(a) Pristine C_8-BTBT:C_{16}IDT-BT topography from AFM methods.

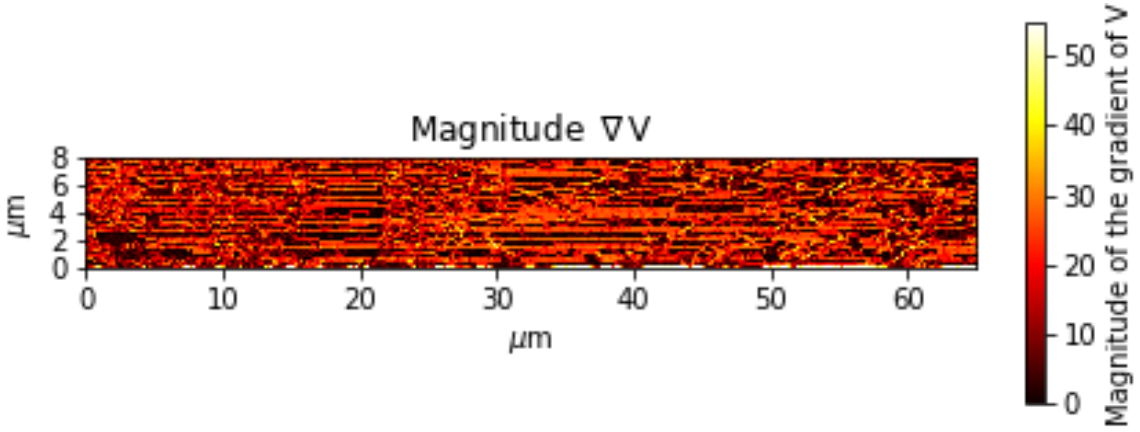

(b) Magnitude of the gradient of the potential for a pristine C_8-BTBT:C_{16}IDT-BT OFET from SKPM methods.

Figure 4.41: Comparison of topography to map of magnitude of the gradient of the potential for a pristine C_8-BTBT:C_{16}IDT-BT OFET device. 65 μm x 8 μm image.

Next, the topography and magnitude of the gradient of the potential for the pristine C_8-BTBT:C_{16}IDT-BT device was compared. It is immediately obvious that the formation of the thin film is vastly different from the dis-TEFADT:PTAA blend. The film appears less uniform and appears to show a separation of material components. Although some scanning anomalies are present the images presented in figure 4.41, it is still possible to ascertain a highly resistive region at the electrode-channel interface at approximately 15-17 μm. It is also possible to infer that the small 'islands' of material that may be separated, appear to be more resistive than the background thin film.

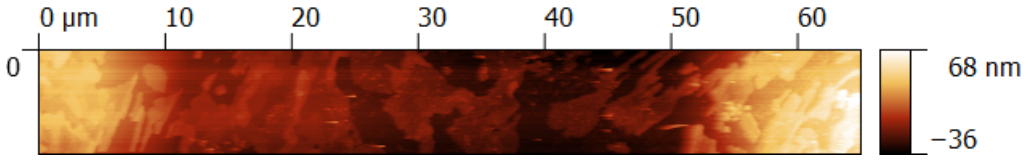

(a) BCF doped C_8-BTBT:C_{16}IDT-BT topography from AFM methods.

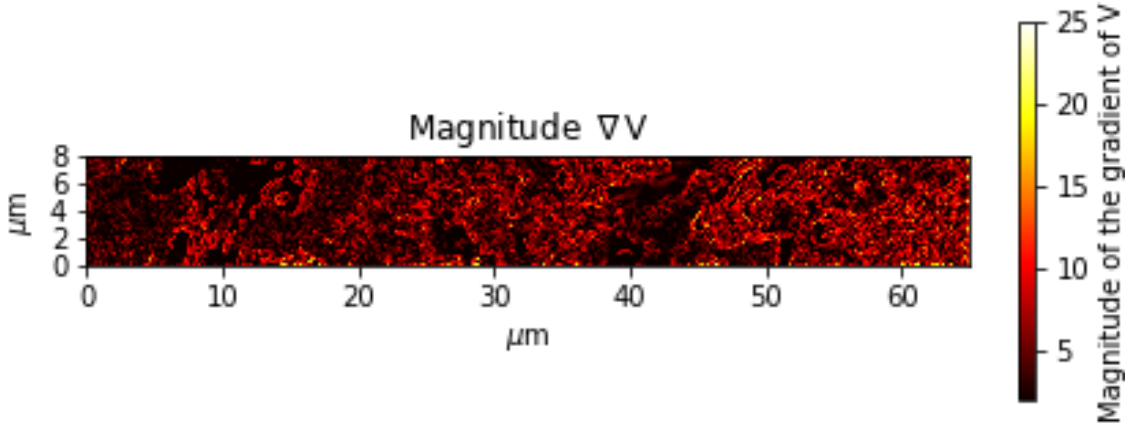

(b) Magnitude of the gradient of the potential for a BCF doped C_8-BTBT:C_{16}IDT-BT OFET from SKPM methods.

Figure 4.42: Comparison of topography to map of magnitude of the gradient of the potential for a BCF doped C_8-BTBT:C_{16}IDT-BT OFET device. 65 μm x 8 μm image.

Finally a comparison of topography to magnitude of the gradient of the potential for C_8-BTBT:C_{16}IDT-BT device doped with BCF was made (figure 4.42). As with the previous blend material, the addition of the dopant has made a large effect of the formation of the film. Whereas for the dif-TES-ADT:PTAA blend the areas of resistivity within the channel were decreased, for the C_8-BTBT:C_{16}IDT-BT they are much more prevalent. It appears that the areas with the highest resistance are the boundaries between the 'islands' and the background thin film. It is also possible to note that the contact resistance shown in the pristine sample of the C_8-BTBT:C_{16}IDT-BT device is no longer present, an effect which was also observed for the dif-TES-ADT:PTAA OSC:polymer blend.

4.3.3 Conclusions from the organic semiconductor polymer blend experiments

While SKPM methods are a powerful tool for probing the potential of OFET's the analysis of the data obtained requires treatment based upon the devices. Standard procedures of obtaining line profiles for various gate and source-drain biases were not suitable for this experiment, and instead taking derivatives of the potential at each point per line of scan allows for a map of changes in surface potential to be obtained. By taking the magnitude of the gradient of the potential it is possible to view areas of highly resistive material and draw observations regarding the formation of the thin films. From this experimental data is was possible to conclude that the addition of the BCF dopant to the OSC:polymer blend resulted in a decreased in contact resistance, as well as altering the formation of the thin film in the channel of the device. For the dif-TES-ADT:PTAA blend the addition of the BCF led to a less resistive channel material, with more frequent ridges in its structure. For the C_8-BTBT:C_{16}IDT-BT material blend the addition of the dopant resulted in more clearly defined 'islands' of material as well as a more resistive channel material at the 'islands'-background boundaries.

Chapter 5

Development of EFM-phase

5.1 Motivation

In order to form a bio-sensing device it is essential that there is a method in place to measure analyte detection. If a protein binds to a carbon nanotube, it can change the charge distribution of the tube [14]. It was initially envisioned that using scanning Kelvin probe microscopy (SKPM) would provide a good overview of the change in electrostatic potential observed when proteins bind to carbon nanomaterials. However, as is introduced in section 2.2.3, the contributions from the cantilever to scanning resolution make it impossible to resolve carbon nanotubes (CNT's) or proteins bound to them. Therefore by applying an AC bias to the cantilever when the tip is scanning in lift mode it is possible to improve scanning resolution by limiting cantilever contributions to the tip apex only [31]. In this chapter the development of experimental and analytic procedures are explored as well as imaging of various structures culminating with imaging proteins bound to carbon nanotubes.

5.2 Previous use of EFM-phase techniques

As the dimensions of devices such as transistors grow ever smaller, there is increased interest in the development of greater resolution imaging techniques. EFM allows for the investigation of not only surface electrostatics for a wide range of devices including thin-film FET devices, solar cells, and carbon nanostructures such as graphene and carbon nanotubes. Moreover, variants of EFM techniques have been developed to probe surface potential, charge distribution and density, surface capacitance, and charge trapping.

The ultimate goal of this section is to image proteins bound to carbon nanotubes. Significant previous work has been attempted using a variety of EFM methods to image carbon nanotubes [136, 137, 138], as well as biological structures such as DNA [139]. However few studies combine the two research interests.

5.3 EFM-phase theory

The theory behind EFM-phase methods was briefly introduced in section 2.2.3 but here, more detail relating to the specific device used to obtain measurements is discussed.

The aim of EFM-phase is to measure the force gradient (where more conventional SKPM measures the force directly) of the tip-sample interaction, allowing the tip apex to be the dominant contributor to the resolution of the scanning method. For SKPM the scanning resolution is reported as 100 nm, whereas for EFM phase C. H. Lei et al have reported a resolution of $\approx$ 20 nm [33]. This makes this method an ideal candidate for the imaging of nano-meter scale biological entities such as proteins.

In comparison to SKPM methods the EFM-phase approach involves minor changes to hardware and a fundamentally different approach to data process. AC bias is applied as the tip is lifted following the topography pass and the phase signal

is collected on the return lift mode pass. A trigger signal is generated at the start of each line scan and as such there are four triggers per cycle of scanning. In order to apply the bias to the retrace pass of the lift-mode operation, the correct trigger must be selected.

Theoretically EFM-phase works thus: under a constant tip-sample bias (V) the electrostatic energy between the tip and the sample is given by

$$U = \frac{1}{2}C(\Delta V)^2, \tag{5.1}$$

where C is the tip-sample capacitance and $\Delta V = V - V_{CPD}$ [140, 141, 142].

The electrostatic force, normal to the sample surface, can be written as the energy gradient

$$F(z) = -\frac{dU(z)}{dz} = -\frac{1}{2}\Delta V^2 \frac{dC(z)}{dz}, \tag{5.2}$$

where z is the tip-sample separation on which U and E are dependent.

In SKPM F(z) is nullified to achieve a direct measurement of surface potential, in EFM-phase the phase is measured instead. This results in an enhancement of scanning resolution compared to SKPM measurements.

The phase difference, Φ, between the applied bias and the tip oscillation can be related directly to the force gradient, $\frac{dF}{dz} = F'$ [143].

A cantilever with a resonant frequency ω_0, and spring constant k experiences a phase difference, when driven at resonance, of $\Phi = \frac{\pi}{2}$ [144]. As the tip approaches the sample surface F'(z) will alter the resonant frequency and effective spring constant of the system, thus affecting the phase angle. At small amplitudes

$$\Phi = tan^{-1}\left(\frac{k}{QF'}\right) \approx \frac{\pi}{2} - \frac{Q}{k}F' \tag{5.3}$$

where Q is the quality factor and k is the dielectric constant. This equation is dependent on the force derivative acting normal to the sample surface such that F' $= \Sigma\frac{\partial F_i}{\partial z}$ i.e. the summation of derivatives of all of the forces acting on the cantilever. The $\frac{\pi}{2}$ term may be excluded if the phase shift is considered as the delay from the

free oscillation state of the cantilever. In this case, allowing for an arbitrary additive phase offset, Φ_0 in the measurement, which includes the $\frac{\pi}{2}$ term,

$$\Phi = -\frac{Q}{k}F' + \Phi_0. \tag{5.4}$$

This suggests that for EFM-phase measurements $\Delta\Phi$ is proportional to the overall force gradient between the tip and the sample. For equation 5.4 the sign of the equation is negative for attractive forces and positive when the forces are repulsive in nature.

Combining equations 5.2 with 5.4 obtains

$$\Phi = -\frac{Q}{2k}\frac{d^2C(z)}{dz^2}(\Delta V)^2 + \Phi_0. \tag{5.5}$$

Since $C(z) = \epsilon_0 k\frac{S}{z}$ for a capacitor, where S is surface area, in a purely capacitive tip-sample interaction the force is always attractive and hence Φ is always negative.

$$\Phi = -\frac{Q}{2k}\frac{d^2C}{dz^2}(V_{tip} - V_{CPD})^2 + \Phi_0 \tag{5.6}$$

which can be simply expressed as

$$\Phi = A(V_{tip} - B)^2 + C \tag{5.7}$$

for fitting purposes. Here $A = -\frac{Q}{2k}\frac{d^2C}{dz^2}$, $B = V_{CPD}$, and C is the phase offset. This shows that in lift mode operation of EFM-phase $\frac{d^2C}{dz^2}$ and CPD can be extracted via a parabolic fit.

5.4 Recovering the data

The data collected using EFM-phase methods is acquired by sweeping the applied tip bias at each data point of the AFM scan in order to obtain a parabolic variation of Φ as a function of V_{tip}. By fitting this curve with equation 5.7 values of $\frac{d^2C}{dz^2}$, V_{CPD}, and Φ may be obtained for each position in the full scan. These values can

then be plotted to generate maps for each of these three parameters.

However, the Multimode SPM system is constrained to obtain only one data point at each pixel in a line scan per channel. There are three channels that may be utilised in this system, and as such data points are acquired for: height, phase angle, and tip bias. By exploiting the fact that the spatial resolution of EFM is inferior to topographical measurements it is possible to deduce a full parabola for each pixel in order to fit the above parameters. Due to the inferior spatial resolution, the period of the AC signal applied to the tip can extend over around 10-15 data points in the topographical scan. This allows the parabola to be fitted to multiple points, taken either from nearest neighbour points in a single line scan or from the neighbouring area in the 2D scan. The fitted parameters can therefore be assigned to the central pixel in the sampled region. By repeating this process with a moving window, the fitted parameters can be obtained for each pixel in the 2D scans and therefore, maps for each calculated parameter may be plotted.

This approach was initially attempted by a former PhD student Isam Abdullah, as part of his PhD project [141]. An unexpected problem that he encountered is illustrated in 5.2. The curve for Φ as a function of V_{tip} is not parabolic in practice. This indicates that the voltage that is measured does not correspond to to the voltage applied to the tip. By systematically varying the applied AC signal frequency and other parameters, Isam deduced that there was a capacitive time constant involved in either the measurement circuit, or in the charging of the tip or the sample surface directly underneath the tip. M. Elliott devised a simple approach to correct for this by assuming a capacitive low pass filter response, a circuit for which can be found in figure 5.1.

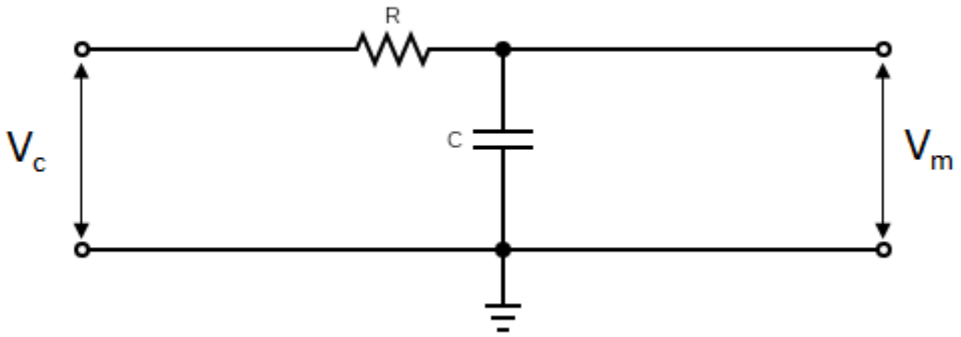

Figure 5.1: A circuit diagram illustrating an RC low pass filter. V_m is the measured voltage and V_c is the voltage corrected by the filter.

Here, the measured voltage, V_m, can be related to the corrected voltage, V_c, by

$$V_c(t) - V_m(t) = Ri(t) \tag{5.8}$$

Where $i(t) = \frac{dQ}{dt}$ and $Q(t) = CV_m(t)$.

Therefore

$$V_c(t) - V_m(t) = RC\frac{dV_m}{dt}. \tag{5.9}$$

This can then be expressed for a set of discrete data points: c_i, and m_i, corresponding to V_c and V_m. Where

$$m_i = \alpha c_i(1-\alpha)m_{i-1}, \tag{5.10}$$

given that $\alpha = \frac{\Delta t}{\tau \Delta t}$, and $\tau = RC$. As such it is possible to deduce corrected voltage values from the measured values as

$$c_i = \frac{1}{\alpha}m_i\frac{1-\alpha}{\alpha}m_{i-1}. \tag{5.11}$$

These expressions allow for the correction of V_{tip} values in the parabola, determining the value of τ by trial and error. Alternatively τ may also be included in the fitting function utilised to fit the measured Φ as a function of the measured V_{tip} as is shown in figure 5.2. This latter approach can be extended to a whole 2D SPM scan, and maps of: $\frac{dC}{dz^2}$, V_{CPD} , Φ and τ generated. In this case, maps of τ are a good test of consistency.

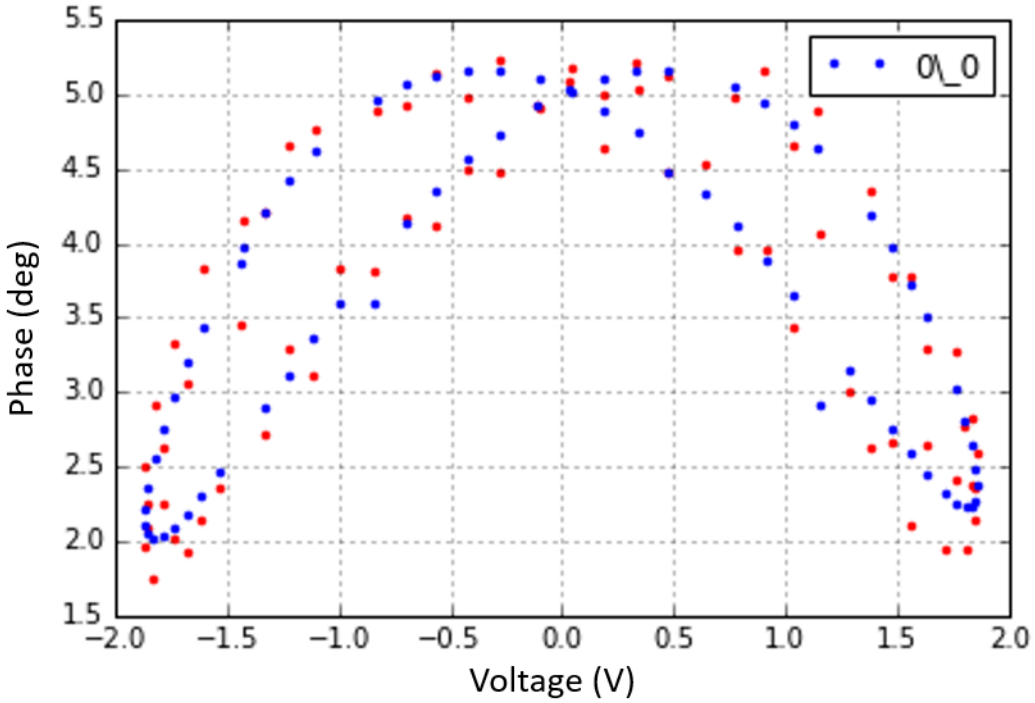

Figure 5.2: An example of the fitting for a selected rectangle of data. The recorded data points are in red, and the fitting in blue. The legend indicates the row and column location from which the fitting window starts for each data set, in this case row 0, column 0.

5.5 Experimental details

EFM-phase is carried out using the same base equipment as for AFM and SKPM measurements. The Veeco Nanoscope IIIa with basic extender module is vibration isolated on a vibration plate as well as an active self-levelling optical table. The device is located is temperature controlled room and isolated from external light sources by blackout blinds and covered windows. In this experimental set-up data can be recorded on three channels allowing topography, applied signal, and EFM-phase shift data to be recorded simultaneously. The phase is randomised at the start of each line to ensure that successive lines of do not simply repeat the bias of the previous line to minimise the occurrence of systematic effects such as vertical lines appearing in the maps of fitted parameters due to fitting of each row of data [141]. The same cantilevers and cantilever holder as utilised for SKPM measurements are also suitable here. Figure 5.3 illustrates the full set-up of our system.

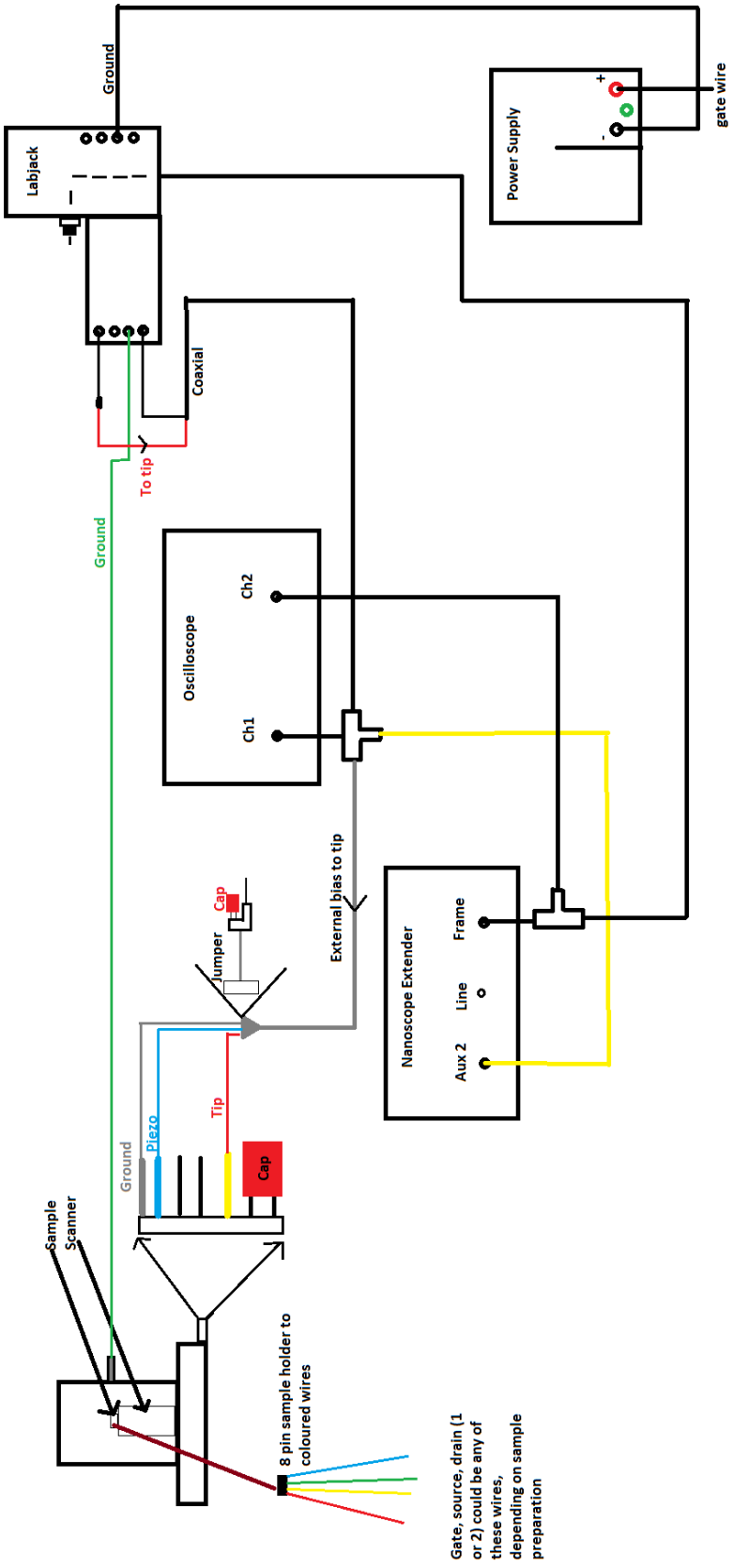

Figure 5.3: A diagram to illustrate the set-up used for EFM-Phase methods.

In order to apply an external bias to the tip, and ensure the correct triggering, alterations to the jumper configurations are made. These can be found in figure 5.4 which is adapted from the Veeco Nanoscope IIIa manual [145]. The voltage is applied to the tip by an Aglient signal generator which is connected via a co-axial cable with a specially designed connector to access the correct jumper pins.

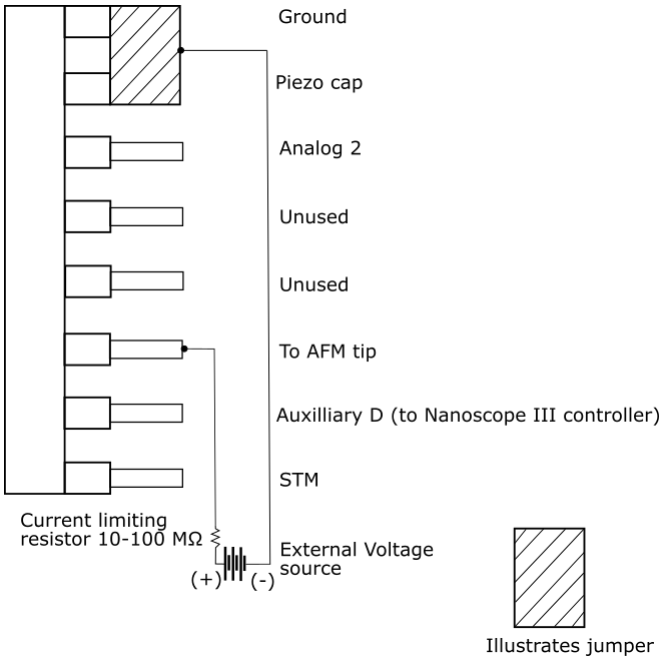

Figure 5.4: Jumper configurations for Veeco Nanoscope IIIa to apply an external bias to the tip for EFM-phase methods.

To begin a measurement an image of the region of interest is first acquired using AFM methods (i.e. no lift mode, two passes only). Once the AFM image is clear and the region of interest has no defects or areas that may cause scanning errors (such as scarring or drift), the EFM-phase measurements may begin. The tip is set to enter lift mode and the tip bias, signal frequency and time/line are set. The nanoscope software is set to record topography on channel 1, analog 2 (which is the applied bias to the tip) on channel 2, and phase on channel 3.

Although this technique and unique set up have been studied before by previous student Isam Abdullah [141], who investigated the effect of scan size, tip bias, signal waveform shape, signal frequency, and the effect of additional resistors; a certain degree of procedural learning still is required. Developing procedures for this method was challenging as no two samples appeared to respond to the same parameters. The most reliable parameter was the time/line, i.e. the time taken

for the tip to scan each line of sample, as this was purely dependent on scan speed which was generally determined to be most efficient at 0.3Hz. Obtaining a correct time/line parameter setting was crucial as this determines when the AC bias applied to the tip will be triggered. An incorrect value will result in the AC bias dropping midway through the scan as the synchronisation of tip scanning to applied bias is lost.

Another setting for the software is the amplitude of the applied bias. This must be sufficient to create a significant signal while maintaining visible changes in the phase image. Through experimental observations a suggested setting for this parameter is -2.00 V, which is practised throughout the experiments presented in this chapter. Closely tied to the amplitude of the applied bias is its frequency. This setting determines the quantity of oscillations per line of scan, in practice: 30, 60, or 120 Hz were applied dependent on sample. The applied AC bias is applied to the tip with a randomised phase for each line of scanning.

5.6 EFM-Phase imaging results

To fully understand the working mechanisms and experimental idiosyncrasies of this method, it is important to use basic and easy to interpret samples as a base line for more complex measurements. Therefore experiments began with single layer graphene on silicon (purchased from Graphenea). Once the basics have been well understood and any initial experimental difficulties addressed, it is possible to use more complex samples such as carbon nanotube field effect transistors and carbon nanotubes functionalised with proteins to obtain a true conception of EFM-phase as a means to detect electrostatic changes for sensing applications.

From the raw data produced by EFM-phase methods maps of CPD, error in CPD, recovered phase, second derivative of the capacitance, and time delay are produced. Each of these offers insight into the sample that has been scanned. The CPD map shows the local contact potential difference calculated between the tip and the sample at each point of the scan. The map of the error in the CPD can

reveal any errors in the feedback loop of the system, a homogeneous map with a small error is desirable. The recovered phase map illustrates the phase shift data recovered after data processing. The second derivative of the capacitance is the key map in these studies. As has been previously mentioned in this study, EFM-phase is expected to produce higher resolution images that SKPM due to the nature of the cantilever interaction with resolution. By taking the second derivative of the capacitance, the contributions of the cantilever to image resolution are limited to the tip apex, therefore the data from this map is expected to be the more detailed that CPD or a standard SKPM image would be. Finally the time delay map illustrates the RC time constant that is outlined in section 5.4, which allows for the correction of V_{tip} in the fitting parabola, a map of the time delay parameter is a good test of consistency within the scanned image.

5.6.1 Graphene

In order to produce a sensing mechanism, proteins must be bound to carbon nanostructures. Graphene with its flat, well ordered structure is an ideal target structure for protein binding. Large area single layer graphene, purchased from Graphenea, was chosen as work within our group was focused on using this type of substrate for protein binding [146, 84]. In figure 5.5 the raw topography, applied AC signal, and resulting phase shift are shown. The sample shows step edges in topography and phase images which may serve as a marker for data recovery. The lack of prominent features in the images implies complete coverage of graphene over the silicon, which is to be expected of a commercially produced sample over a 1 μm scan area.

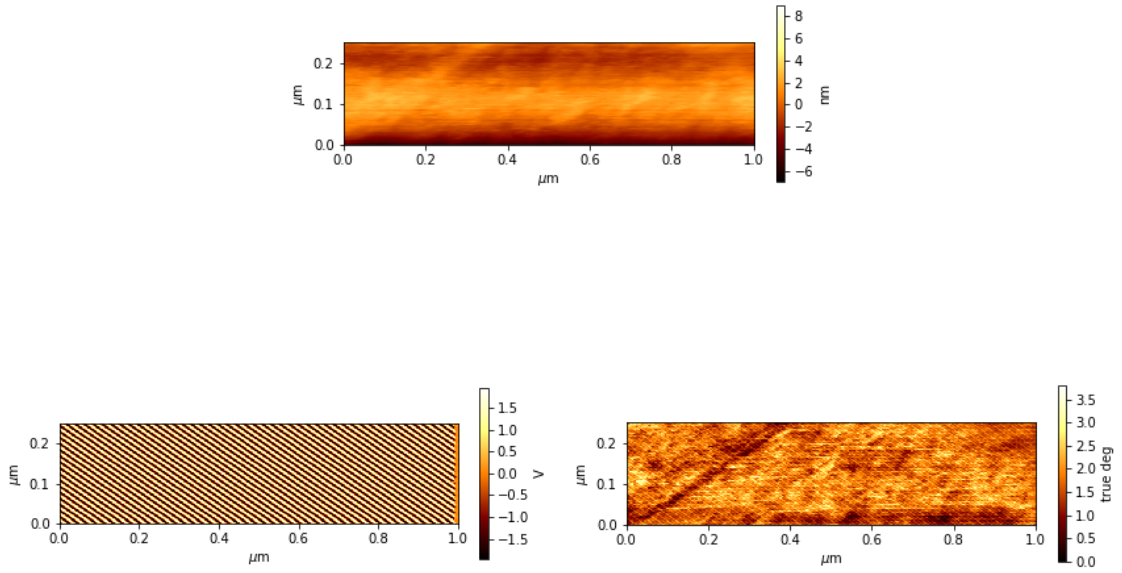

Figure 5.5: Raw EFM-phase data for Graphenea graphene on silicon, image size 1.00 μm x 0.25 μm. **(a)** Topography **(b)** Applied AC signal **(c)** Phase data with overlaid AC signal

The data is then analysed using the specially designed software. Maps of CPD, error in CPD, recovered phase, second derivative of the capacitance, and time delay are produced.

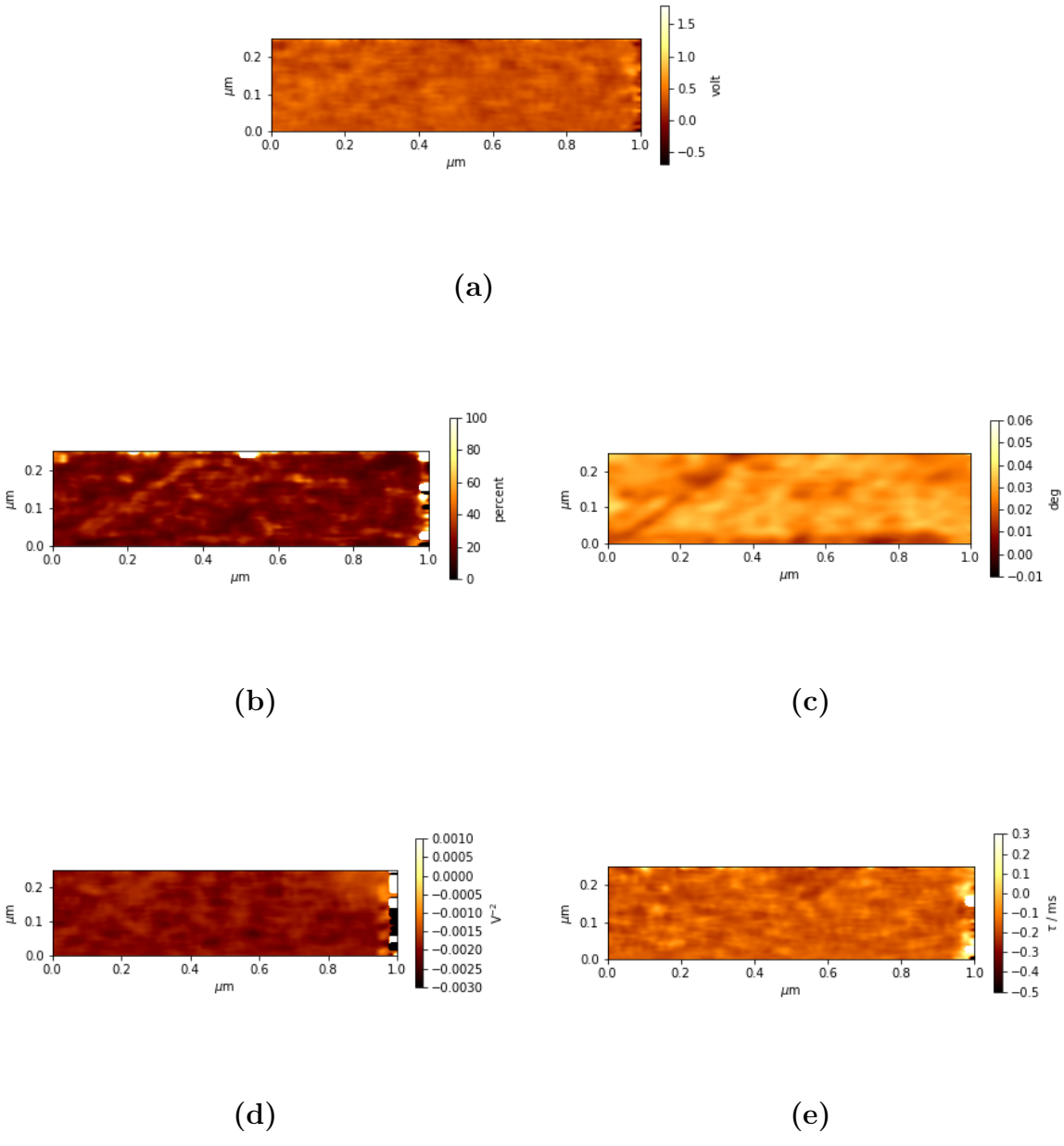

Figure 5.6: Analysed EFM-phase data for Graphenea graphene on silicon, image size: 1.00 μm x 0.25 μm **(a)** CPD **(b)** Error in CPD **(c)** Recovered phase data **(d)** Second derivative of the capacitance **(e)** Time delay

Analysing the data (shown in figure 5.6) shows full coverage of graphene (there is little contrast in the CPD to imply any background silicon is present) with well recovered phase data, however the error in the CPD is relatively large and appears to be dependent on the material coverage showing a larger error at the graphene edge. This data is promising, but in order to observe proteins using

this method, a more discreet target is needed. Therefore the study continues with carbon nanotubes.

5.6.2 Carbon nanotubes across electrodes

Before proteins are added to the carbon nanotubes it is prudent to image using clean nanotubes. A sample of a carbon nanotube FET, produced by Dr Adam Beachey, is used: where the nanotubes are attached to gold electrodes through dielectrophoresis. From the raw topography data in figure 5.7 it is clear that a significant bundle of tubes is bridging the electrode channel.

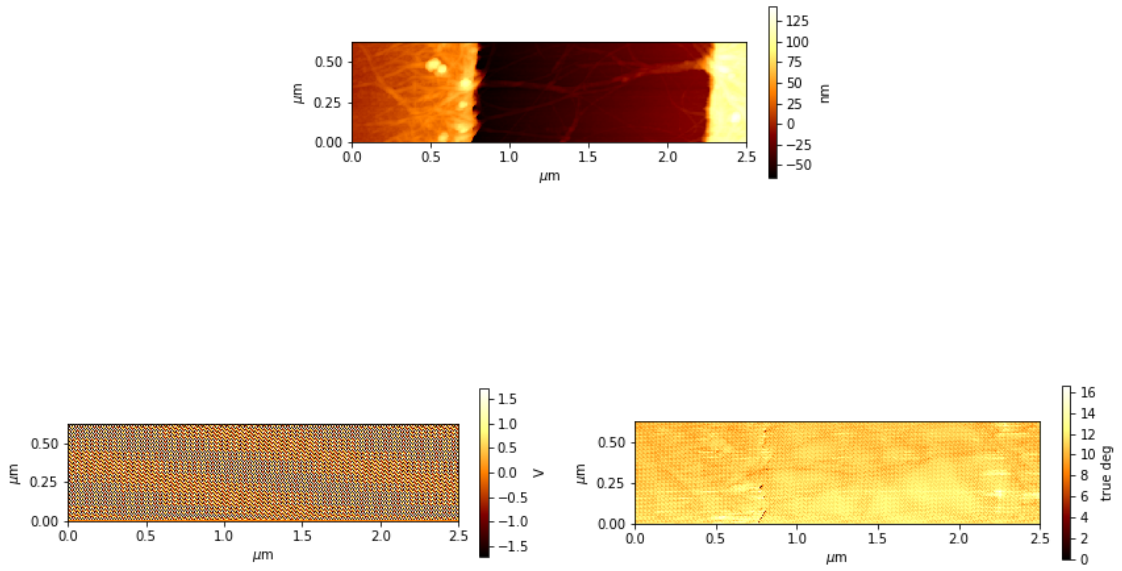

Figure 5.7: Raw EFM-phase data for carbon nanotube field-effect transistor, image size: 2.50 μm x 0.63 μm **(a)** Topography **(b)** Applied AC signal **(c)** Phase data with overlaid AC signal

From the analysed data, found in figure 5.8 it is clear that some of the nanotube bundle structure is recovered. The general shape of the bundle at its thickest parts are easily visualised, however the finer details of the bundle with single tubes are less readily shown. This implies that although the resolution is greatly increased from that of standardised SKPM, the resolution achieved with EFM-phase

will still not be enough to visualise proteins on single carbon nanotubes. It is also possible to note that the error in the CPD is greater over the electrodes, and while no scanning defects were shown in the raw data, there appears to be some manner of defective data once analysis has been completed. This is also mirrored in the map of time delay.

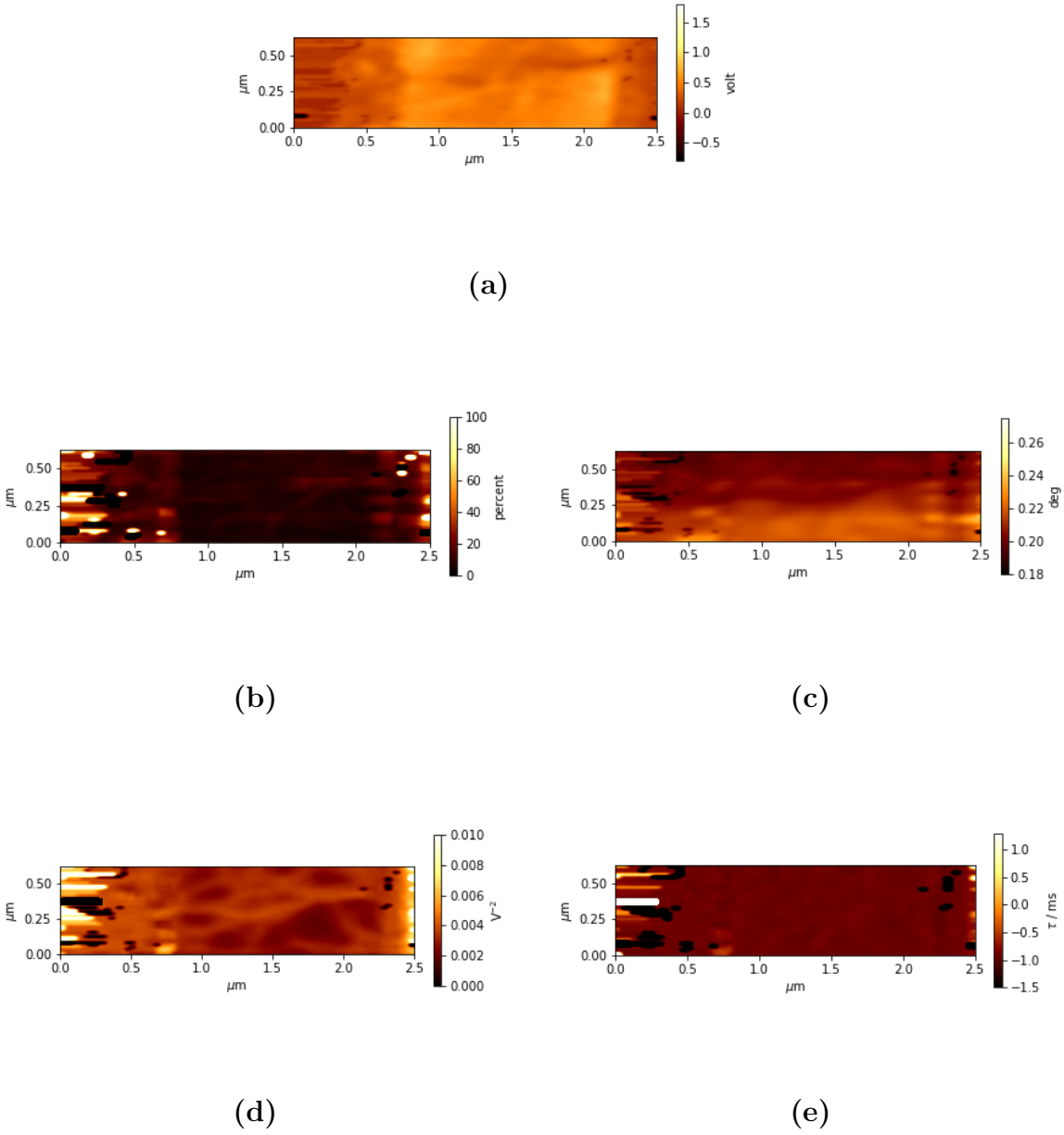

(a) **(b)** **(c)** **(d)** **(e)**

Figure 5.8: Analysed EFM-phase data for carbon nanotube field-effect transistor, image size: 2.50 μm x 0.63 μm. **(a)** CPD **(b)** Error in CPD **(c)** Recovered phase data **(d)** Second derivative of the capacitance **(e)** Time delay

5.6.3 Carbon nanotubes with dimers of short-axis cytochrome b_{562}

The EFM-phase method is now tested on proteins immobilised on carbon nanotubes. For this experiment, dimers of short-axis cytochrome were selected as they have been proven to bind well with AFM and, as they are in a dimer form, are larger than the more stable GFP. As is shown in figure 5.9 the tubes functionalised with the cytochrome are wider than bare nanotubes, it is however difficult even in the topography to visualise the proteins. It was verified using AFM methods that protein was bound to the carbon nanotubes, as this study was run in conjunction with the experimental results that can be found in section 6.3. It is important to note that the AFM topography images presented in this section were obtained using an EFM tip, i.e. Si coated in Pt-Ir, which will therefore produce topography maps with a poorer resolution when compared to images presented in section 6.3.

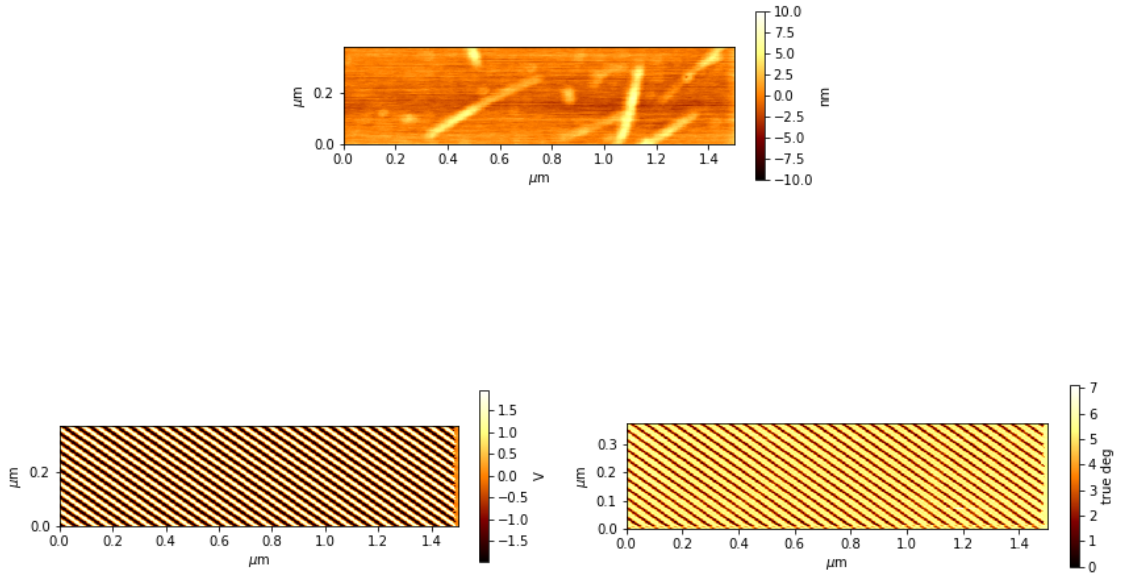

Figure 5.9: Raw EFM-phase data for carbon nanotube field-effect transistor functionalised with short-axis dimers of Cytochrome b_{562}, image size: 1.50 μm x 0.38 μm **(a)** Topography **(b)** Applied AC signal **(c)** Phase data with overlaid AC signal

Upon analysis, as shown in figure 5.10 it is clear that no protein will be

observed using this method. The outline of the tubes, as with the bare carbon nanotube FET, are observed in the analysed images however the resolution is not great enough to distinguish proteins from background tubes.

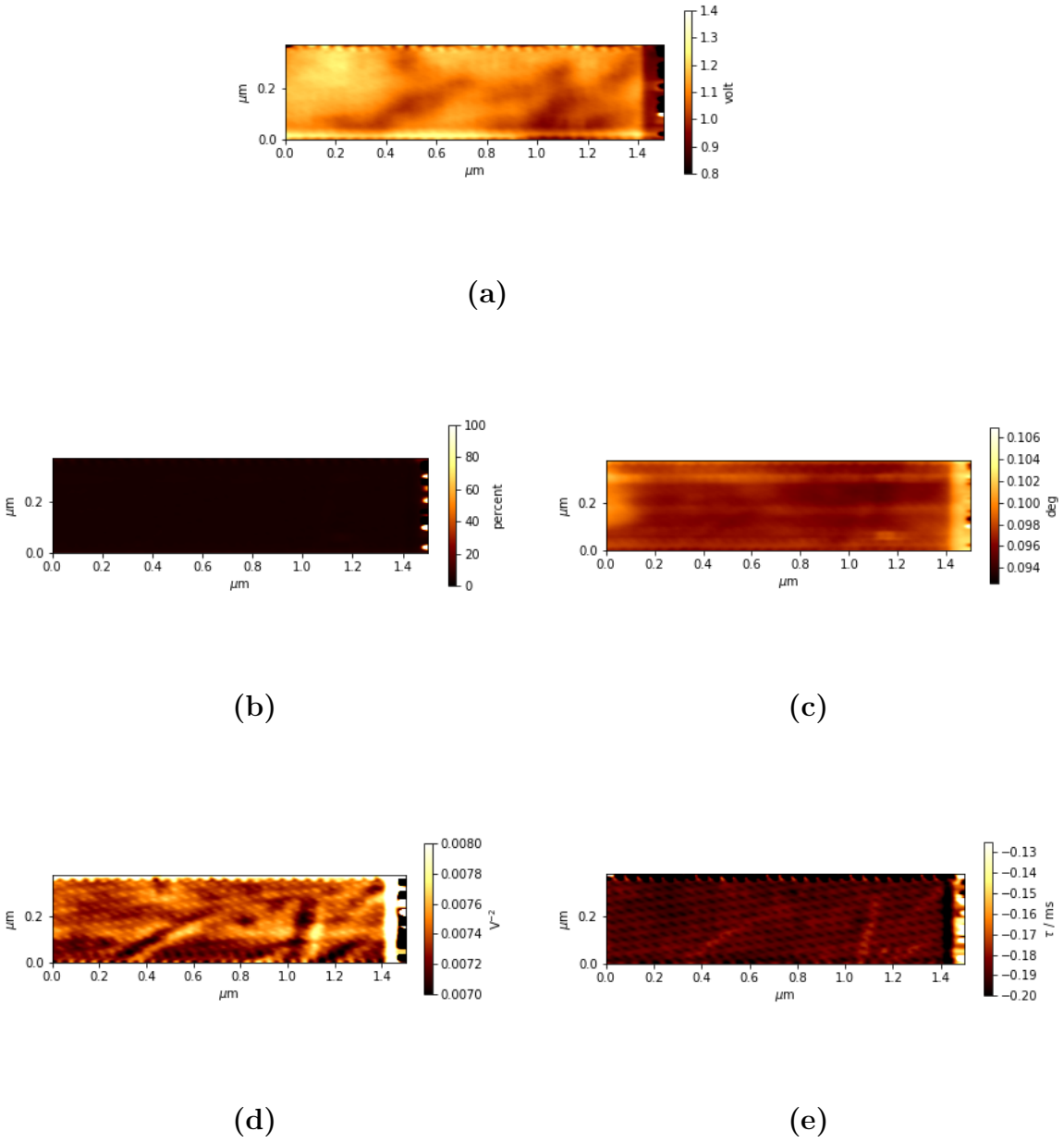

(a)

(b) **(c)**

(d) **(e)**

Figure 5.10: Analysed EFM-phase data for carbon nanotube field-effect transistor functionalised with short-axis dimers of Cytochrome b_{562}, image size: 1.50 μm x 0.38 μm **(a)** CPD **(b)** Error in CPD **(c)** Recovered phase data **(d)** Second derivative of the capacitance **(e)** Time delay

5.7 Conclusions

While this method shows some initial promise for imaging the contact potential difference of various structures with an increased resolution when compared to SKPM, ultimately there are too many variables and the method fails to be reproducible for the same sample. While greater investigation of this method is warranted, for the purview of the work presented here it was decided that a change in direction was needed. As studies were proving promising in the area of topographical analysis combined with methods to visualise proteins such as confocal microscopy and total internal fluorescence microscopy (TIRFM), it was decided that the project should continue in this topic. Although disappointing, these experiments proved to be an interesting learning process but ultimately too time consuming.

In context of recent literature on both carbon nanotubes and graphene, there have been multiple studies investigating the electrostatic properties of both. The potential uses of each of these materials are vast, including sensing applications. A particularly interesting property of carbon nanotubes that has been studied using EFM methods, is charge trapping within loops of carbon nanotubes [138]. This effectively shows that carbon nanotubes may be used as boundaries for controlling substrate changes, which is crucial when forming electronic devices. Furthermore EFM has been used to observe areas of single, bi-layer [147], and multi-layer graphene [148] which offers a clear method for defining areas of graphene deposited on a substrate. The EFM-phase method, if further developed, would offer a higher resolution method for observing these effects. It is already clear in the early results for graphene, that layers in the graphene substrate can be distinguished.

Chapter 6

Protein binding mechanics to sp^2 carbon nanostructures

6.1 Motivations

The formation of a bio-sensing device capable of achieving the sensitivity level required to detect single binding events is a feat which researchers around the globe are working to optimise. In this chapter, studies of protein binding to carbon nanostructures using various SPM methods as well as TIRFM and confocal microscopy are presented. The detection of protein binding, and the ability to distinguish the base detector protein from the desired analyte, with high accuracy will be crucial to the formation of a highly sensitive bio-sensing device.

Presented within this chapter are experiments concerned with the binding of proteins to various carbon nanostructures. The nanostructures used within these studies are single wall carbon nanotubes (SWCNT's), monolayer graphene and highly ordered pyrolitic graphite (HOPG). All proteins used in these studies have been genetically engineered to incorporate the non-natural amino acid - azido phenylalanine (azF) which acts as a linker molecule that can be covalently bound to carbon structures. In the first study presented in this chapter, the protein uses is a dimerised form of cytochrome b_{562} (Cyt b_{562}). This study is used to demon-

strate the detection in height difference when the disulphide bridge that dimerises the protein is chemically broken. The second study presented is much more comprehensive and utilises the many properties of the green fluorescent protein (GFP). Within this second study the binding mechanics of the protein to the nanostructure are investigated, as well as studies into the relationship between the carbon/protein bond and the placement of the azF linker molecule.

6.2 Protein binding to carbon nanostructures and retention of activity

To prove that proteins covalently bound to carbon nanostructures retain their activity, experiments that demonstrate an inherent feature of the protein pre and post binding were employed. To perform a proof of concept experiment such as this, the protein in question must have an easily observed feature. In the case of this experimental work, the protein GFP was utilised. The variant of the protein used was modified with an azide phenylalanine at the 204 site. GFP was selected for use in this experiment due to its fluorescent properties, which allow for easy visualisation. GFP is a well known protein and has been the focus of many studies, its properties are well documented. This section draws upon previous work of previous students from the nano-group at Cardiff university, and current research in the pharmacy and bio-sciences groups at Cardiff university [84].

In order to visualise the GFP as it is bound to the carbon nanostructures, confocal and TIRF microscopy methods are employed. Both of these methods rely upon excitation of the fluorophore, central in the protein structure, and observation of the emissions.

6.2.1 Graphene

The first of these experiments were performed on flat, single layer graphene on a silicon substrate. Confocal microscopy was employed for investigation of the bound

protein, as the silicon substrate is not transparent and as such TIRF microscopy methods are unsuitable.

In these experiments a droplet of 10 nM sfGFP 204 azF was drop cast onto the substrate such that the entire surface was covered. Two sample types were produced, the first was incubated for 10 minutes in the dark before a thorough rinse with DI water for 1 minute. The second was incubated for 10 minutes in the presence of 305 nm wavelength UV light before a thorough 1 minute rinse with DI water. The samples were then imaged using confocal microscopy methods to obtain multiple regions of interest (ROI). Each ROI was approximately 400 μm squared in size, in order to encapsulate the scale of protein binding to the graphene surface, even at such a relatively concentration of 10 nM.

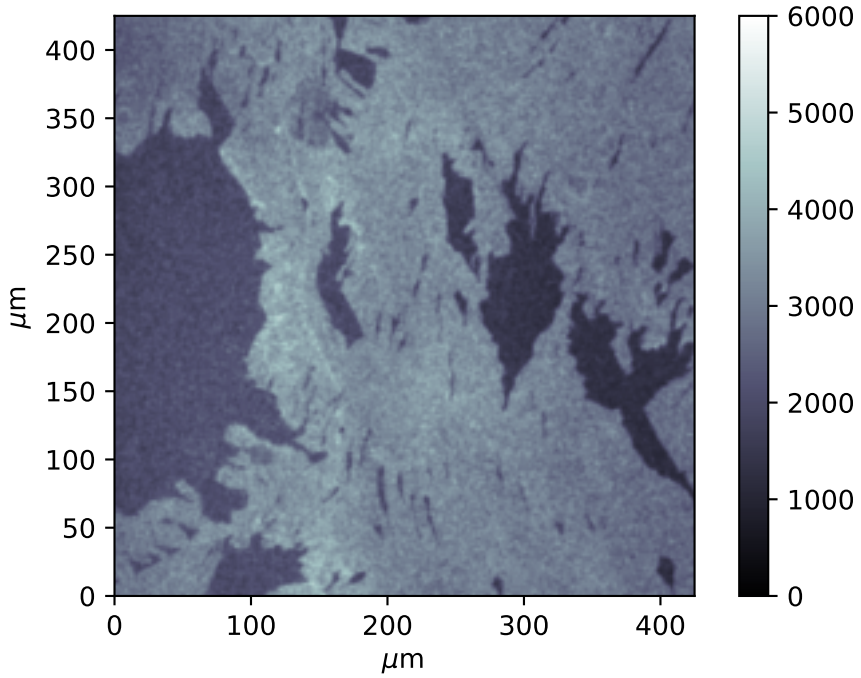

Figure 6.1: Confocal microscopy image of UV incubated sfGFP 204 azF on graphene on silicon.

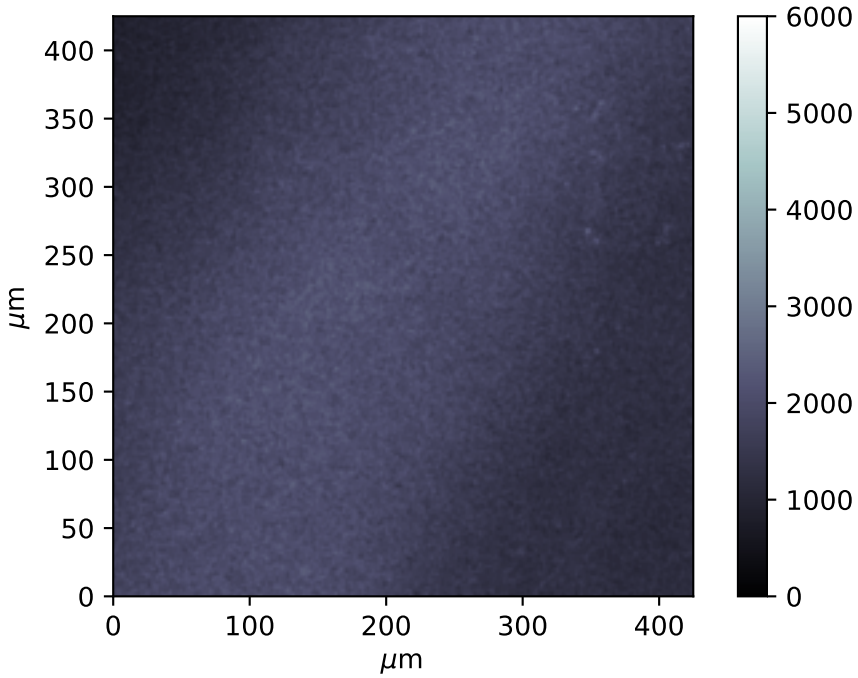

Figure 6.2: Confocal microscopy image of sfGFP 204 azF incubated in the dark on graphene on silicon.

Figure 6.1 illustrates the retention of activity after binding to the graphene, and figure 6.2 shows that binding to the graphite surface does not occur in the absence of UV activation of the photo-chemically reactive azF handle. Although arbitrary, the vertical scale used to illustrate intensity has been set to the same scale for each sample. These images were taken using a Zeiss LSM880 confocal laser scanning microscope with the assistance of the bio-imaging hub in the Cardiff school of bio-sciences. These experiments not only serve the purpose of providing proof of retained protein activity, but also offer further evidence to verify the successful attachment of the protein GFP 204 azF to the carbon nano-surface.

In figure 6.2 a relatively uniform spread of low intensity background fluorescence is observed. There are no defining features visible on the graphite surface. This effectively proves that no protein has been bound to the graphene surface. This was verified using multiple ROI taken from multiple samples, figure 6.2 is representative of this data. By contrast figure 6.1 shows the large area distribution of the graphene on the silicon surface. The areas of the sample which are not highly fluorescent are most likely the silicon substrate. This image illustrates not only the

protein attachment and retained activity, but also offers insight into the coverage of graphene on the silicon surface. The area shown in figure 6.1 was chosen to illustrate the partial coverage, other ROI showed a much fuller coverage of graphene. The graphene used in these experiments was supplied by Graphenea. This work is based upon the protein attachment approach set up by Athraa Zaki during her time in the nanogroup at Cardiff University [146].

6.2.2 Carbon nanotubes

Although it has been proven that graphene is an excellent substrate for the covalent attachment of proteins, carbon nanotubes are more readily available and offer multiple benefits including: choice of substrate, control of density, can be put down across electrodes, or have electrodes patterned over them, offer a smaller target area in which to investigate. As such the continuation of this project will focus on protein binding to carbon nanotubes. The TIRF data used within this section has been obtained and reproduced with permission by Dr David Jamieson of the pharmacy department of Cardiff University.

Using carbon nanotubes allows control over density and substrate. For the purpose of this experiment, the substrate that will be employed is a glass cover-slip. This allows for TIRF microscopy measurements to be taken of GFP 204-azF without tubes, and carbon nanotubes with sfGFP 204 azF bound covalently.

In figure 6.3, GFP 204 azF is deposited onto the cover-slip and imaged with TIRFM methods. Observing a singular frame of the TIRF image yields only background signal, however upon averaging over 20 frames the single molecules and aggregates of the GFP come into view. Through the appearance of these GFP, it is clear that the protein sample is active, as an inactive or unfolded protein would not present any fluorescence.

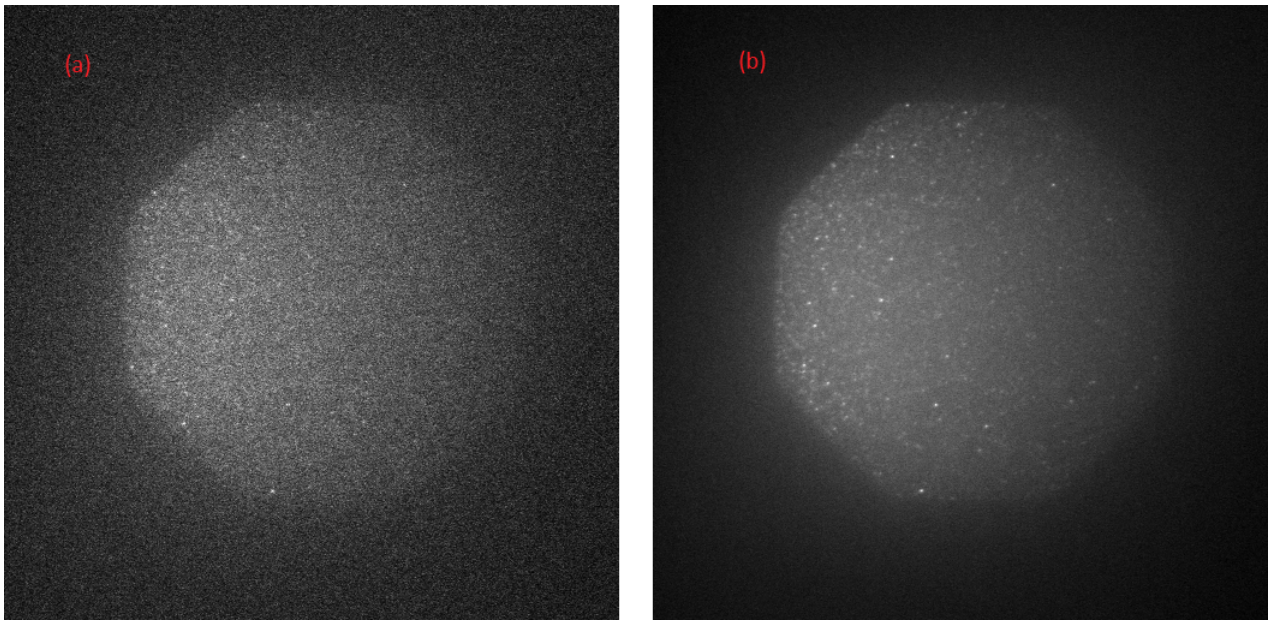

Figure 6.3: TIRF microscopy images of sfGFP 204 azF on cover-slip for (a) one frame and (b) averaged over 20 frames.

Adding the carbon nanotubes by drop cast method to the cover-slip allows the study of bound GFP, by creating a well defined structure for which to search for. If the protein retains activity upon U.V. activated binding, then defined chains or filament like patterns of GFP should be observed by the TIRF microscope. In figure 6.4 the GFP has been added to the immobilised carbon nanotubes and exposed to 305 nm wavelength light to induce binding. From a singular frame, as without nanotubes, only a background signal is obtained. However data produced by averaging over 20 frames produces an image which clearly displays the strand like pattern that was expected. This implies that the protein retains its activity after binding to carbon nanotubes. An interesting aside that has not been explored within this work is the alteration of the photo-physics of the GFP when attached to carbon nanotubes. Binding GFP to carbon nanotubes appears to prolong the lifetime of the protein before photo-bleaching occurs, as well as affecting the intensity of the fluorescence produced. Various studies into these effects are currently underway and can also be found in the PhD thesis of previous nanogroup student Adam Beachey [149].

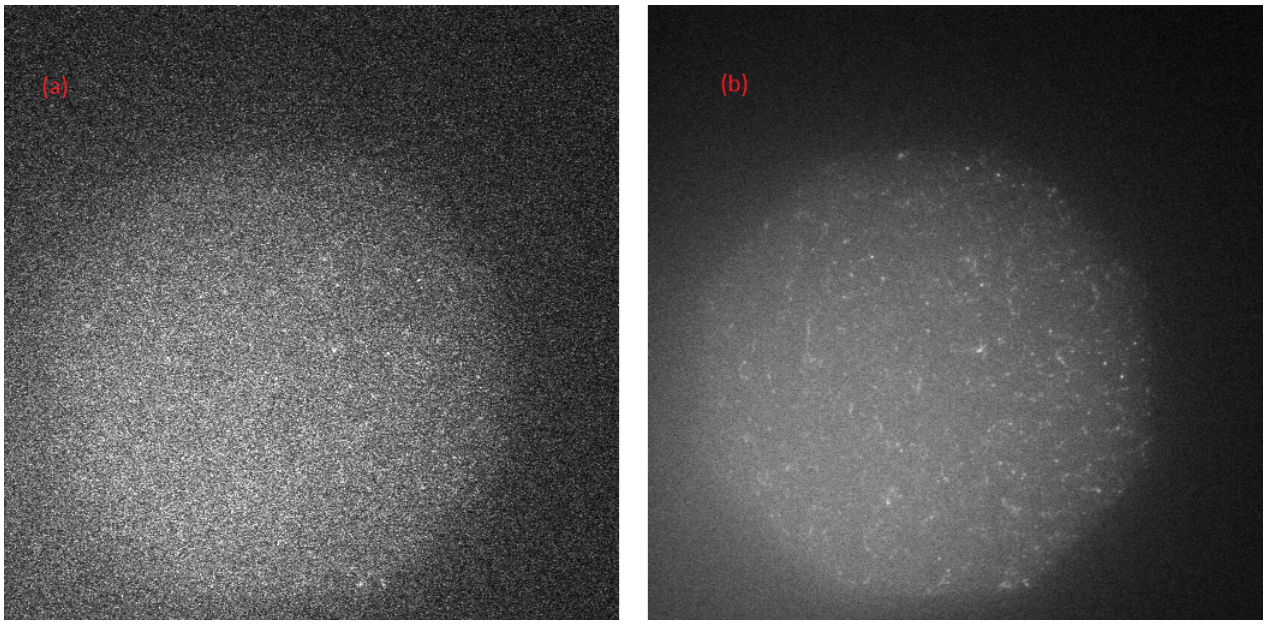

Figure 6.4: TIRF microscopy images of sfGFP 204 azF covalently bound to SWCNTs for (a) one frame and (b) averaged over 20 frames.

6.3 Atomic force microscopy as a tool to distinguish modification of attached protein

To be able to produce convincing data regarding a protein acting as a detector for an analyte, we must first be able to demonstrate that we can identify changes to the height of a protein. While AFM is not the first method one would consider for the detection of protein binding, when used in conjunction with other data collected, such as electrical measurements, it assists in building a more comprehensive study of the changes a device may go through.

In order to demonstrate the capabilities of AFM in the detection and distinction of modifications made to a protein bound to a carbon nanostructure, the protein cytochrome b_{562} in its dimerised form was utilised. The protein was bound to SWCNT's on a silicon substrate and imaged using AFM. The disulphide bridge that allows the protein to exist as a dimer was then chemically broken, resulting in two monomer protein structures. Two dimer variants were used, a long axis (LA) and a short axis (SA). The differences in the structure between the wild-type and each dimer variant can be seen in figure 6.5. More detailed information regarding

this protein can be found in section 3.5.2

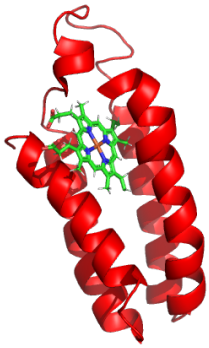

(a) Wild type cytochrome b_{562}

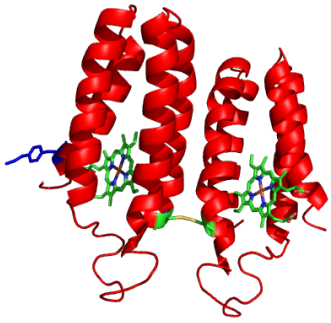

(b) Short axis dimerised cytochrome b_{562}

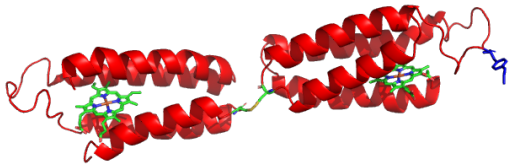

(c) Long axis dimerised cytochrome b_{562}

Figure 6.5: The molecular structure of three variants of the cytochrome b_{562} molecule (a) wild type, (b) short axis dimer and (c) long axis dimer. The azF residue in the dimerised protein forms in shown in dark blue.

In this experiment silicon substrates were used as cytochrome b_{562} is not fluorescent and silicon is a much more robust substrate. Samples were prepared by cleaving a silicon wafer covered in photo-resist into 0.5 cm^2 squares. The wafer chips were soaked in acetone for 5 minutes at 75°C to remove the photo-resist, followed by a 5 minute soak in isopropanol at the same temperature to remove any residue from the acetone. A solution of tubes was then drop cast onto the cleaned silicon chips and left to dry on a hot plate at 100°C for 5-10 minutes or until dry. The dried tube solution was briefly rinsed under flowing DI water, followed by a further rinse under flowing ethanol and finally soaked in ethanol for 1 hour. The ethanol soak removes any SDS surfactant from the tube solution that has dried onto the silicon. Once the soak is complete, the samples are given a final rinse with DI water for 30 seconds to remove any ethanol before drying under a nitrogen stream.

To attach the cytochrome variants, each silicon-SWCNT sample was taken in turn to a low humidity (<1%) glove box in which is situated an LED (λ = 305 nm) that will activate the reaction between the azF and the carbon nanostructure to allow covalent binding to occur. A droplet of 20 μl of protein solution at a concentration of 100 nM was drop cast onto the silicon surface. The samples were then illuminated using the LED or alternatively, incubated in the darkness of the glove box for 10 minutes. This was followed by a vigorous 60 second rinse under flowing DI water. The samples were then dried under nitrogen stream and imaged using AFM.

6.3.1 Cytochrome b562 long axis dimer

A study comparing the attachment of the LA Cyt dimers for both UV and dark incubation. Figure 6.6 shows the AFM surface topography for SWCNT's on a silicon substrate with proteins covalently bound using the UV light activated azF reaction. The inset of this figure shows a zoomed in area of the image in order to better demonstrate the clear addition of protein to the tubes. Figure 6.7 shows the AFM surface topography for the dark incubated LA cyt dimer, therefore there should be no attachment of protein to the SWCNT's. Again, the inset is to better visualise that no protein has bound to the tubes.

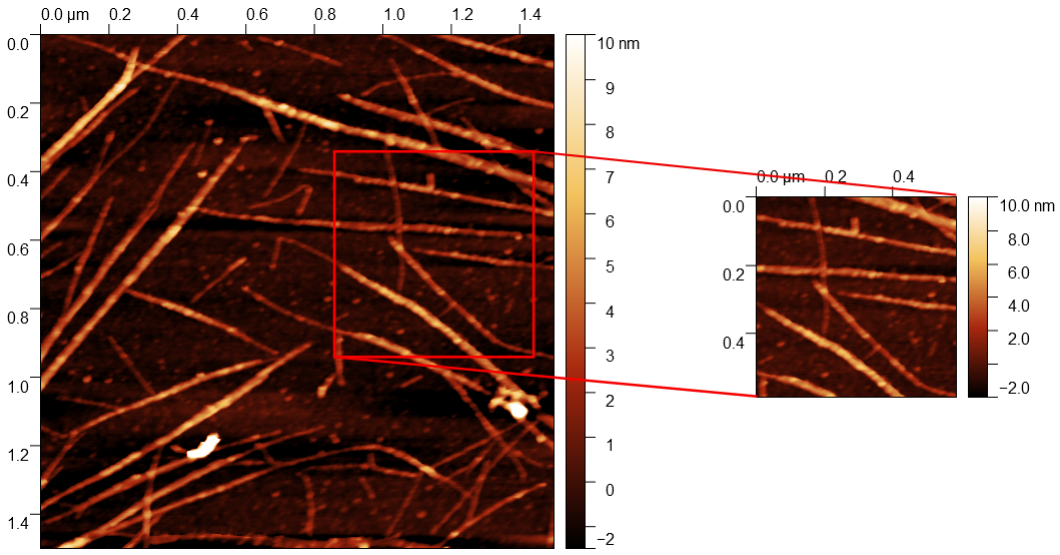

Figure 6.6: Surface topography for LA cyt b_{562} dimer covalently bound by azF to SWCNT's on silicon substrate. The inset shows a 0.5 μm x 0.5 μm zoomed in section of the image to better illustrate the addition of proteins to the tubes. Filename: 2018-02-02.009. Image size: 1.5 μm x 1.5 μm.

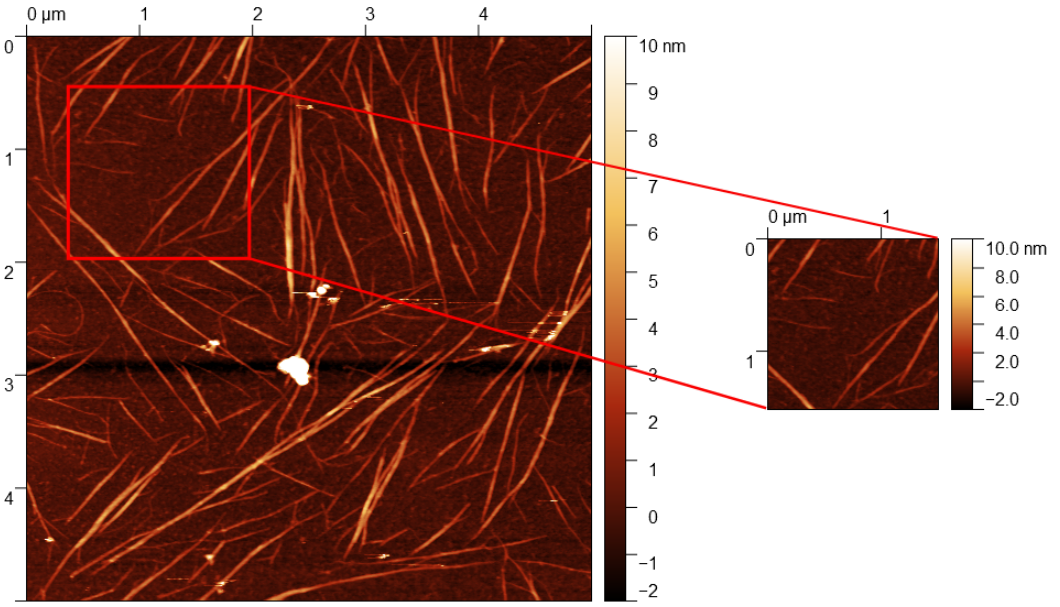

Figure 6.7: Surface topography for LA cyt b_{562} dimer, incubated in the dark. The inset shows a 1.5 μm x 1.5 μm zoomed in section of the image to better illustrate the lack of protein on the surface of the tubes. Filename: 2018-02-02.004. Image size: 5.0 μm x 5.0 μm.

In order to confirm that the protein is only attached to the SWCNT after exposure to light, height profiles were obtained from a single tube. Using the Gwyddion software (data process → distortion → straighten path) to select a single tube to straighten out, followed by the extract profiles tool in order to take profiles of the height at various positions along the SWCNT. The AFM topography of dark and UV incubated samples for the LA Cyt dimer can be found in figures 6.9a and 6.8a. To illustrate the stark difference between the samples the Y axis scale was kept the same for each height profile graph. This shows us that UV irradiation of the sample after drop-casting the protein solution results in a height increase of between 3.0 nm to 5.5 nm. In figure 6.8b, the irradiated sample, it is observed that even the baseline CNT measurement (height profile 1) reads at 2.0 nm; whereas in the non-irradiated sample shown in figure 6.9b the CNT height is between 0.7 nm and 1.2 nm. This may be due to protein crowding along the nanotube causing the AFM tip to never actually image the CNT between proteins. Due to the height difference in the surface topography between irradiated and non-irradiated samples, the upper bound of the colour bar had to be adjusted from 10.0 nm to 3.0 nm in order to visualise the CNT clearly. Each CNT was carefully selected from its respective image to ensure only single tubes were measured.

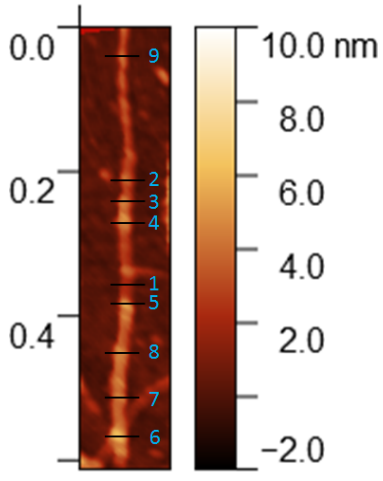

(a) A single straightened tube with height profile positions.

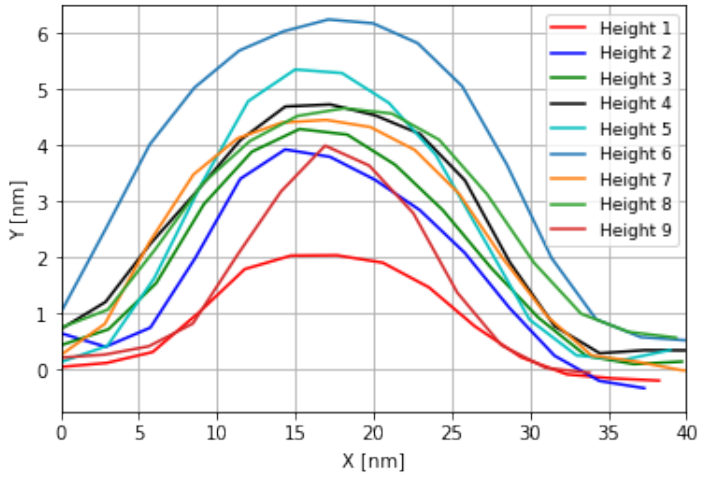

(b) Height profiles on a single SWCNT.

Figure 6.8: Height profiles for a single, straightened SWCNT and the positions at which the profiles were taken. The tube is functionalised with LA dimer Cyt after UV exposure.

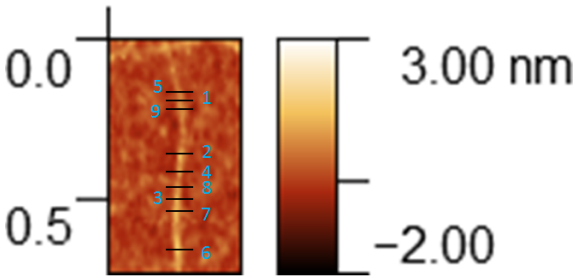

(a) A single straightened tube with height profile positions.

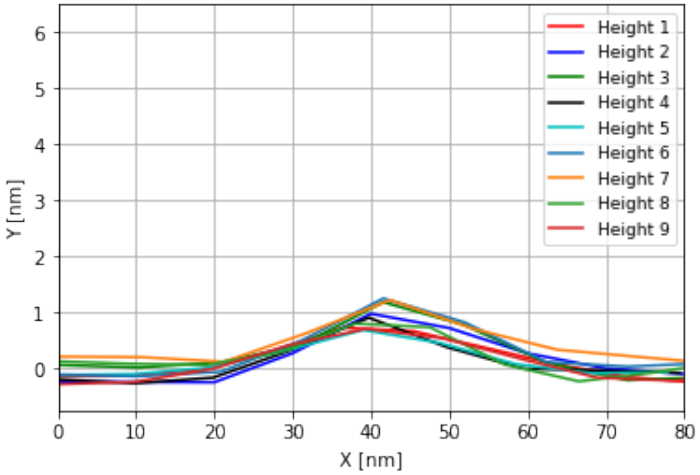

(b) Height profiles on a single SWCNT.

Figure 6.9: Height profiles for a single, straightened SWCNT and the positions at which the profiles were taken. The tube has been exposed to LA dimer Cyt without UV irradiation, so no protein is bound to the tube.

These images offer some evidence that the cytochrome dimers bind preferentially in the presence of UV irradiation. The disulphide bond that dimerises the protein is chemically broken using dithiothreitol (DTT) in order to observe the difference in height profile for monomer and dimer. A droplet of 0.5 mMol DTT was drop cast onto the sample, with enough volume to cover the entire surface in solution. After 10 minutes, the sample was rinsed in flowing DI water to remove the DTT.

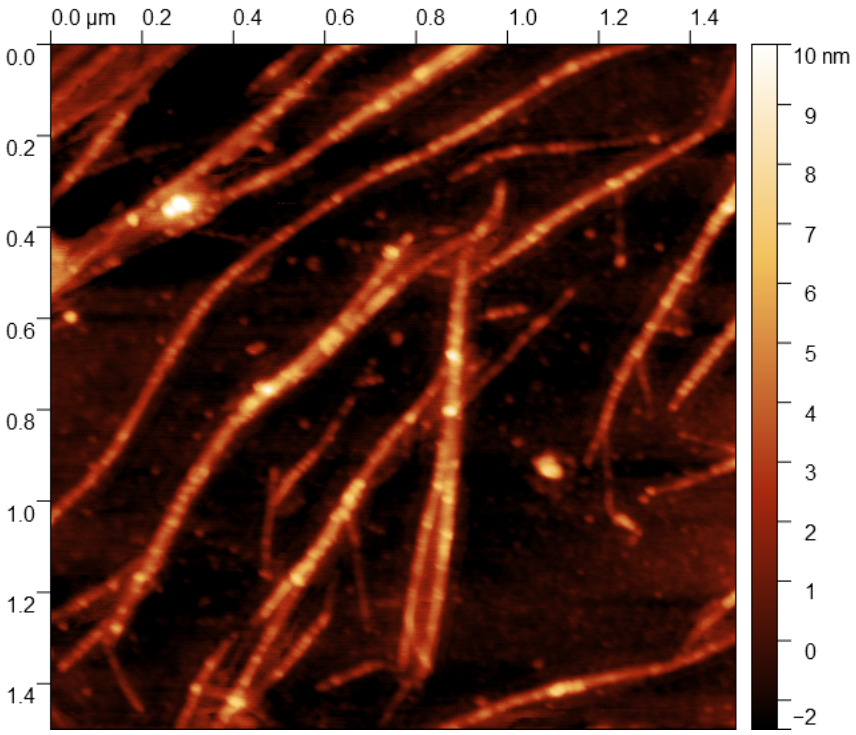

Figure 6.10: AFM surface topography of UV irradiated LA Cyt dimer after the addition of DTT to break the dimerising disulphide bond between the monomer cytochromes. Filename: 2018-02-05.001. Image size: 1.5 μm x 1.5 μm.

Upon the addition of DTT, there is a visible difference between figures 6.10 and 6.6. Though there is not a noticeable difference in visual height, the proteins on the tubes appear as less cleanly ordered and well defined. However, a visual study of the images is a poor method for distinguishing differences at the nanoscale, and so we take multiple height profile measurements over multiple AFM topographies for both pre and post DTT addition, and from these results produce a histogram of perceived protein heights.

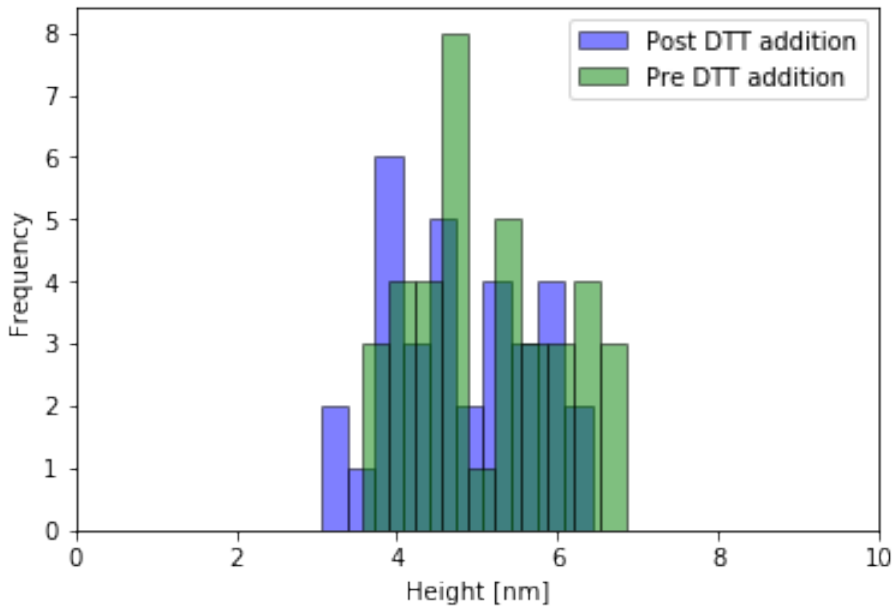

Figure 6.11: Histogram showing the height difference of long axis cytochrome b562 pre and post DTT addition

From figure 6.11 it can be observed that the measured height of the protein on the tube upon the addition of DTT is only slightly decreased with the mean height before addition of 5.13 nm compared to 4.77 nm after the DTT has been added, a decrease of only 0.36 nm. This is a somewhat unexpected result and returning to the LA dimer structure in figure 6.5c an understanding of this result may be obtained. The protein is covalently attached at two sites via the azF, at the end of each monomer structure. Once the DTT breaks the disulphide bridge between the dimer, the monomers may spring apart. It was initially expected that this strain release would cause the monomers to spring upwards and away from the tube, however this is not what we observe, the data suggests that despite the strain release the monomers remain in the same position on the tube. However, since we see no change in the observed height of the protein on the tube we may consider that both of the azF attachment sites are not in use. It could be that only one side of the dimer is binding to the tube and as the protein dries it lies flat along the SWCNT. The removal of the disulphide bond reintroduces water into the system via the DTT suspension, as the bond breaks the second unbound protein may be washed away and only the bound protein would remain, still lying flat. In this situation we would see no change in height. Another plausible situation is that the strain release is not great enough to cause any change in the protein position. If this is the case, either

one or both of the azF could be covalently bound to the SWCNT. This is however simply speculation and we are unable to produce proof for any of these ideas.

6.3.2 Cytochrome b562 short axis dimer

The investigation into cytochrome dimers continues with the short axis (SA) cyt dimer variant. As before, we first wish to establish that the SA cyt binds to the tube preferentially under UV light exposure.

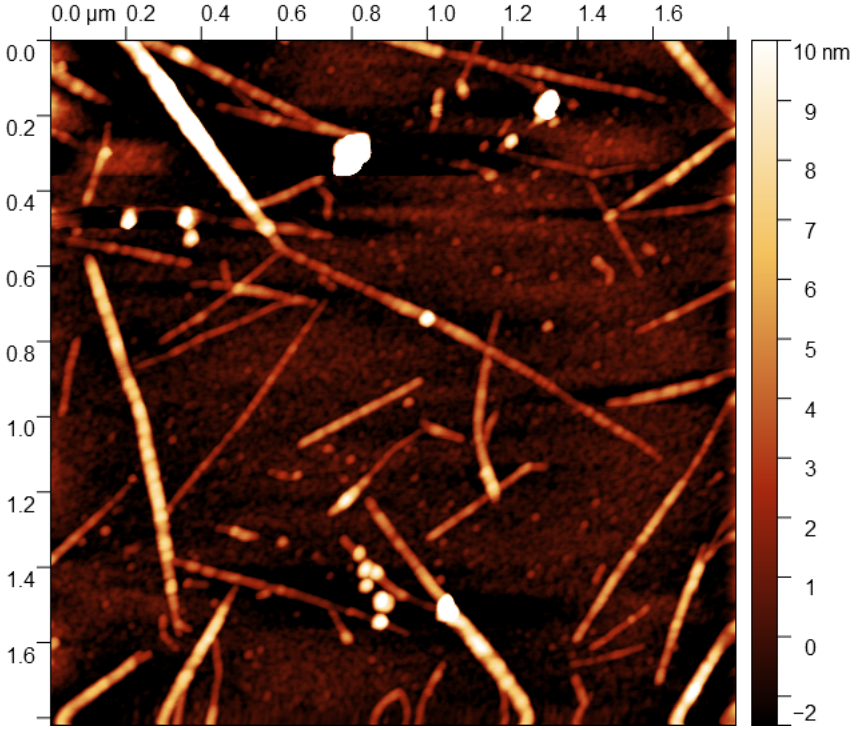

Figure 6.12: Surface topography for SA cyt b562 dimer covalently bound by azF to SWCNT's on silicon substrate. Filename: 2018-02-23.007. Image size: 1.72 μm x 1.72 μm.

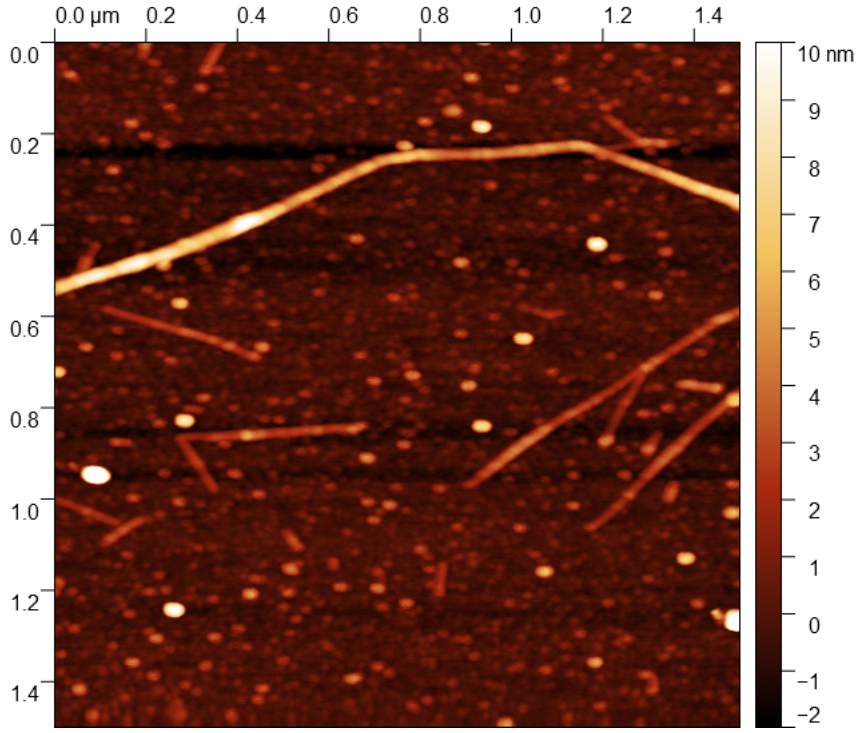

Figure 6.13: Surface topography for SA cyt b562 dimer, incubated in the dark. Filename: 2018-03-16.014. Image size: 1.5 μm x 1.5 μm.

Unlike with the LA cyt dimer, the difference between the UV irradiated and the non-irradiated sample is not as clear. Protein-like 'blobs' on are observed on the surface of the SWCNT's in both instances. Straightening out single tubes from each image and measuring the height profiles at various positions along the tube does not alleviate the concern that the proteins are also binding in the absence of the UV light source (figures 6.14 and 6.15 for UV and dark incubation respectively).

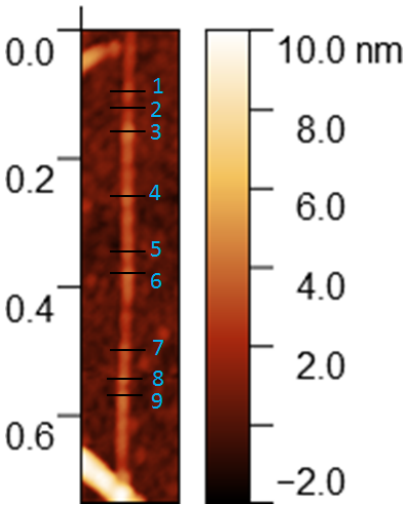

(a) A single straightened tube with height profile positions.

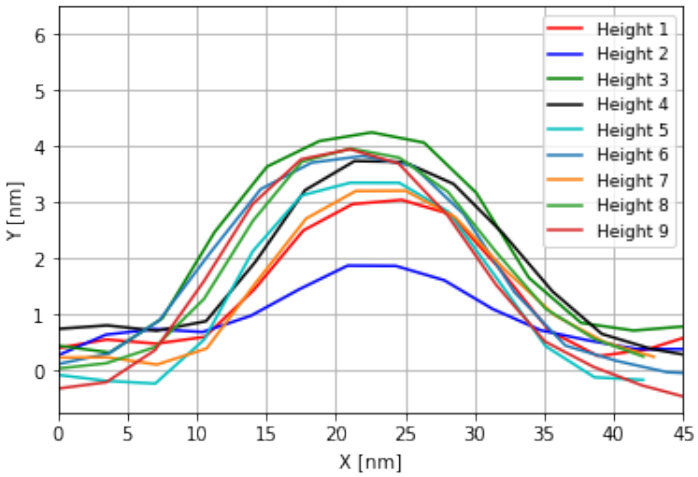

(b) Height profiles on a single SWCNT.

Figure 6.14: Height profiles for a single, straightened SWCNT and the positions at which the profiles were taken. The tube has been exposed to SA dimer Cyt under UV irradiation, and as expected protein has bound to the tube.

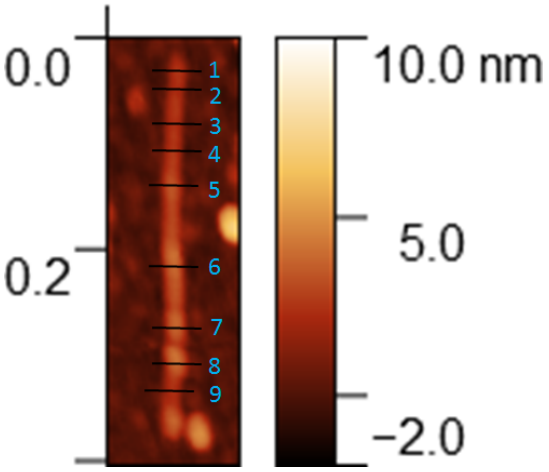

(a) A single straightened tube with height profile positions.

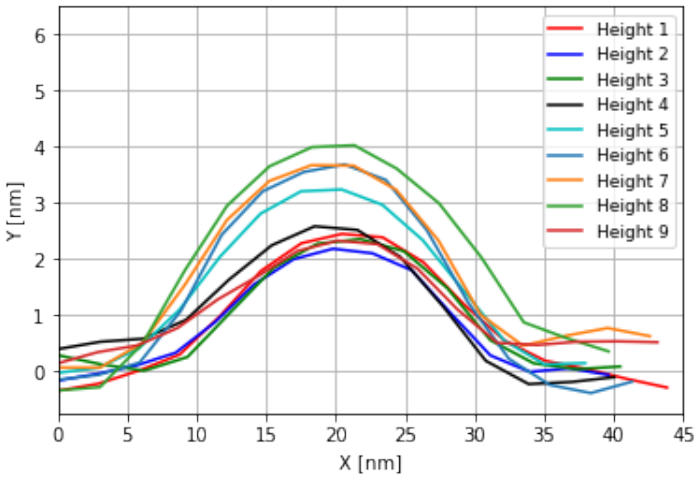

(b) Height profiles on a single SWCNT.

Figure 6.15: Height profiles for a single, straightened SWCNT and the positions at which the profiles were taken. The tube has been incubated with SA cyt dimer without UV light exposure. It is not expected for protein to bind to the tube.

Despite the fact that we observe SA Cyt dimers on the tube in the absence of UV irradiation, the study will continue with the addition of DTT to the UV exposed sample. As with the LA cyt dimer UV sample, a droplet of 0.5 mMol DTT was drop-cast onto the sample surface, sufficient to cover the entire sample. After 10

minutes the sample was rinsed in flowing DI water to remove the DTT. The results of this experiment can be visualised in figure 6.16.

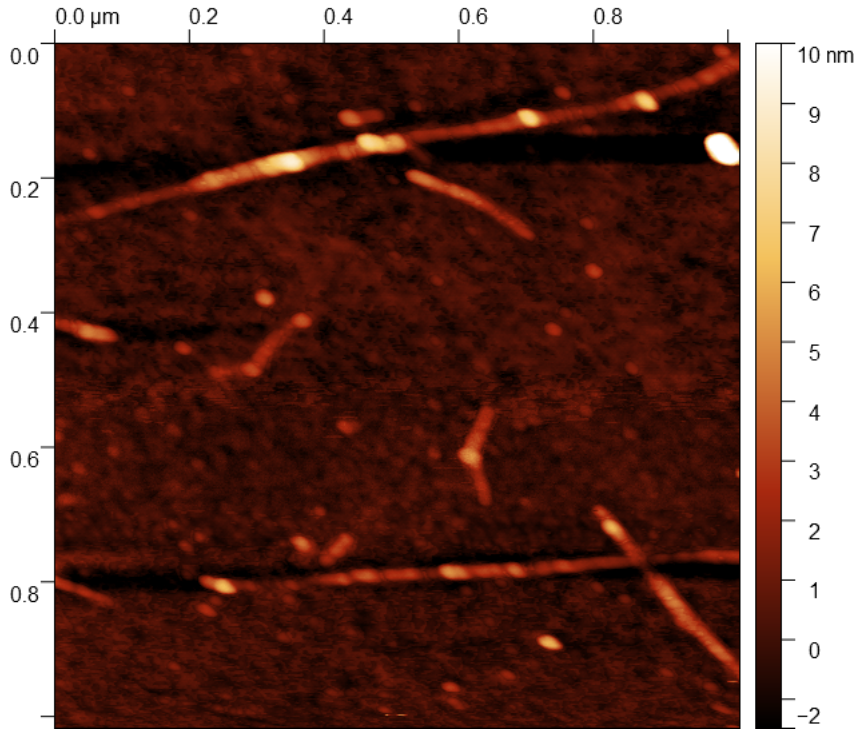

Figure 6.16: AFM surface topography of UV irradiated SA Cyt dimer after the addition of DTT to break the disulphide bond between the monomer cytochrome. Filename: 2018-02-23.020. Image size: 1.2 μm x 1.2 μm

The disulphide bond that dimerises the protein is broken and a histogram of max heights of perceived proteins to compare before and after DTT addition is produced.

Figure 6.17 allows us to observe the results of the DTT addition at a more statistical level. There is a clear difference in the height recorded by the AFM before and after DTT. Before DTT, the mean protein height is found to be 5.17 nm, and upon the addition of DTT is reduced by 2.3 nm to a mean height of 2.87 nm. This is a reduction of almost half the initial recorded height, implying that one half of the dimer pair is no longer attached to the tube. This may suggest that, in the case of the SA cyt dimer, only one of the azF is binding to the tube. In this case, one the DTT has severed the disulphide bridge, one of the monomer cytochrome proteins may be washed away in the DI rinse.

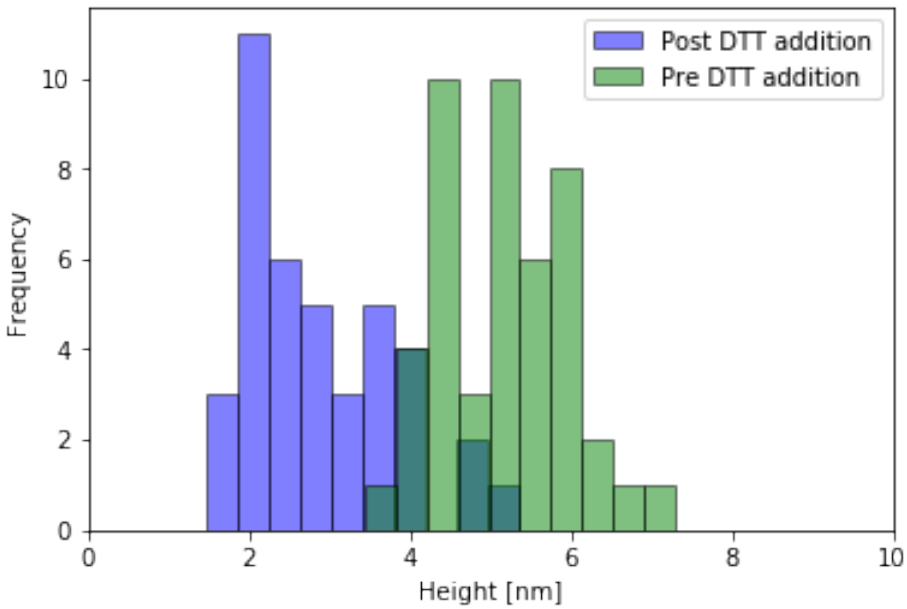

Figure 6.17: Histogram showing the height difference of short axis cytochrome b562 pre and post DTT addition

6.4 Conclusions

Dimers of cytochrome in both its long and short axis variants, provide a useful platform to investigate the usefulness of AFM methods in identifying alterations to proteins when bound to SWCNT structures. Using AFM identification of changes in the cytochrome dimers was successfully performed, namely the transformation of dimer to monomer structure, upon the addition of the chemical DTT. By taking the maximum height observed for the perceived protein structures immobilised on the tube, before and after DTT addition, a statistical analysis of protein dimers compared to the monomer form was produced.

In the case of the LA cytochrome dimer, there was little change observed upon the addition of DTT, with a reduction in mean height of only 0.36 nm. Compare this to the observed change for the SA cytochrome dimer and we find a reduction in mean height of 2.30 nm. Almost half of the pre DTT height. From a protein perspective this implies that the SA dimer experiences the loss of one of the monomers in each pair. This leads to the hypothesis that only one of the two available azF amino acids is binding to the tube in the presence of UV and as such,

once the disulphide bridge is broken, one half of the dimer pair is removed from the surface. In the case of the LA dimer, the very small reduction in height may lead us to believe that both available azF amino acids are covalently binding to the SWCNT and as such, once the disulphide bridge is removed, the protein remains statistically unchanged. The small (0.36 nm) reduction is height could potentially be attributed to the strain release of breaking apart the dimer pair allowing each monomer closer to the SWCNT.

6.5 Variation of azide phenylalanine placement in green fluorescent protein

By utilising the protein sfGFP using AFM, investigations of protein height for sfGFP variants with the photo-chemical reaction handle azF in designed positions were undertaken. Some evidence of activity retention in GFP proteins covalently bound to CNTs has already been presented through the use of TIRF microscopy, however it is also pertinent to this study that the proteins bound to the nanotubes are in the correct orientation. In the case of a detector protein, for example, the binding site for the analyte must be exposed for analyte detection.

6.5.1 sfGFP 80 azF

The first variant of GFP studied is the sfGFP with azF located at residue 80 as shown in figure 6.18. The height of the protein is taken using the Gwyddion software from topography images obtained using AFM, an example of which can be found in figure 6.19. The base of the AFM image is flattened, and any polynomial background is removed. Then, each protein covered tube is straightened and height profiles across the centre of the protein are taken. In order to make a comparison to the bare tube underneath the proteins, a profile is taken in between the bound GFP. These profiles are then plotted as can be seen in 6.20.

After AFM height analysis of the immobilised proteins it is useful to explore

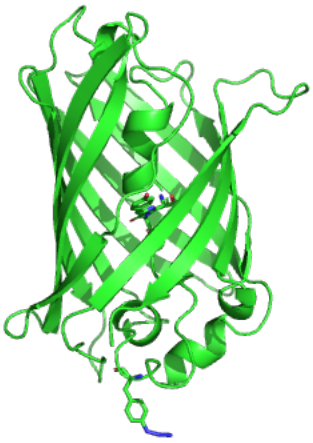

Figure 6.18: A representation of the protein variant sfGFP R80 azF. The chromophore is shown at the centre of the barrel like structure of the sfGFP and the azF is shown at residue 80

the ratio of width to length, where we define width as the dimension across the tube, and length as the dimension along the tube. In the case of sfGFP 80 azF the protein should be orientated on the nanotube such that it has the dimensions 2.4 nm by 4.2 nm. Despite the fact that the AFM tip causes a convolution of the lateral resolution of the protein [150], a ratio of length to width can offer a degree of information regarding the protein-tube configuration. A histogram of measured width and length can be found in 6.21 where the width of the protein is measured across the tube, and length is measured along the tube a visual representation of protein width/length measurement is given in figure 6.22.

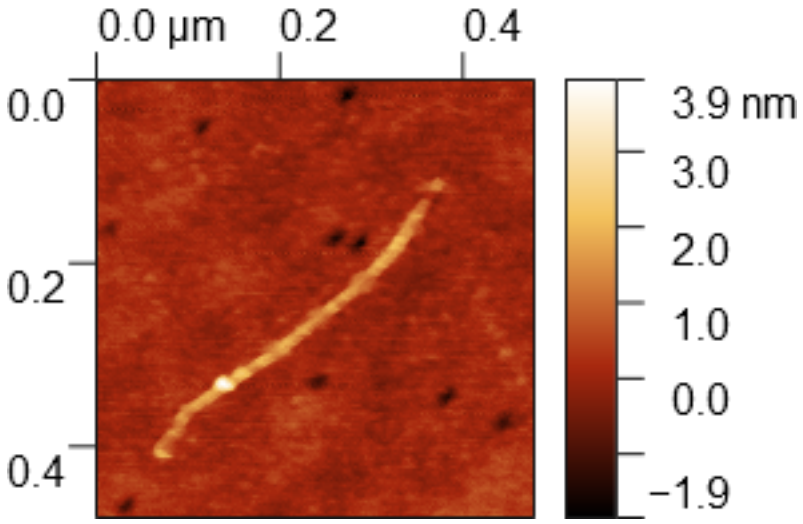

Figure 6.19: AFM topography for a sSWCNT on glass cover-slip functionalised with 100 nMol R80 sfGFP. 2018-05-17.000. Image size: 0.5 μm x 0.5 μm.

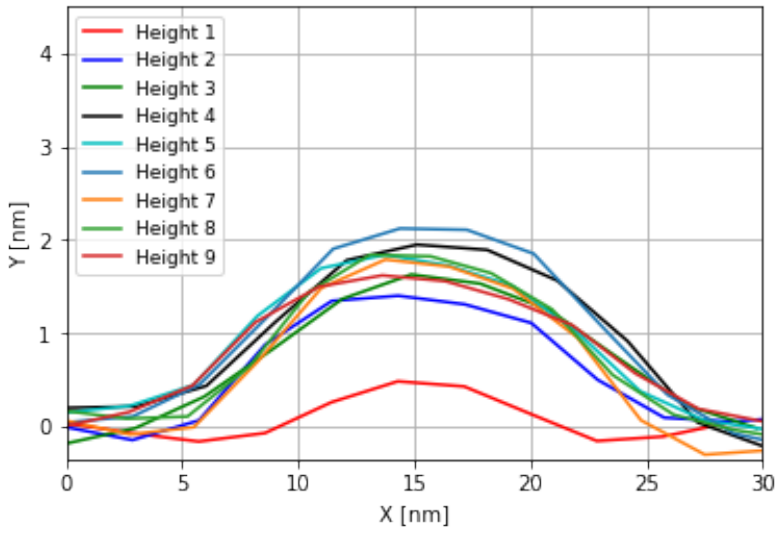

Figure 6.20: Height profiles for covalently bound sfGFP R80 azF on single wall carbon nanotubes deposited on glass cover-slip from AFM topographies.

The mean of the measured protein length is found to be 10.5 nm, whereas the mean of the measured protein width is 24.2 nm; over twice that of the length. Although lateral dimensions recorded from AFM topography are dominated by tip radius effects, this could imply that the measured dimensions agreed with the accepted dimensions of the sfGFP protein (2.4 nm by 4.8 nm). It is also worth mentioning that the spread of the data for the measured widths of the protein is much larger than the spread for the length measurements. This could indicate that this particular variant of the protein is not binding to the uppermost area of the CNT, but to the sides.

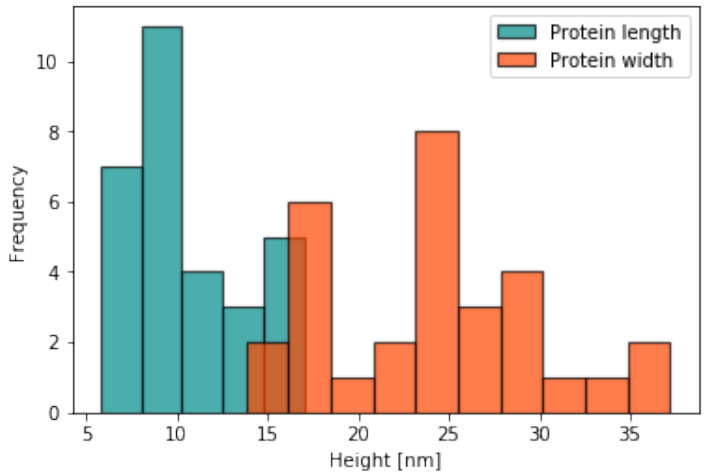

Figure 6.21: A histogram to demonstrate the ratio of length to width of sfGFP 80 azF covalently bound to single wall carbon nanotubes deposited on glass cover-slip from AFM topographies.

6.5.2 sfGFP 111 azF

The next variant of sfGFP used in this experiment is sfGFP E111 azF. In the case of this variant, the azF is located at residue 111 on the long axis of the protein. This should result in a height profiles lower than that of sfGFP R80 azF. A sample topography image for sfGFP E111 can be found in figure 6.24

By taking the heights of the protein on the tube as with the R80 azF variant, it can be observed that the sfGFP E111 azF is measured at 2-3 nm in height, where the R80 azF (which is expected to be higher) is measured at 1.5-2 nm in height. It is already well documented that a lower protein height is observed with AFM measurements. This, compounded with the fact that the protein on the tubes are dried out for scanning, may produce height measurements much lower than expected. Due to the curved nature of the carbon nanotube, it may be that the protein is not attaching to the apex of curvature of the nanotube, but is in fact attaching to the side of the nanotube. This could result in the protein flattening against the glass substrate instead of lying along the surface of the nanotube.

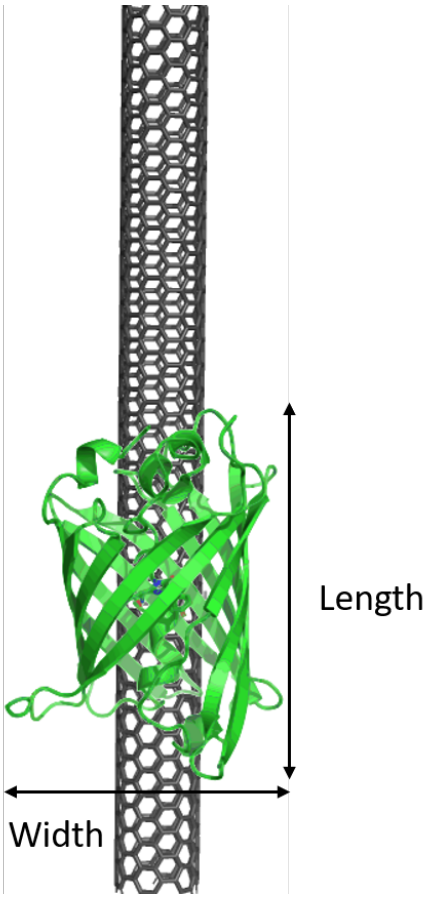

Figure 6.22: A simplistic illustration to demonstrate how protein length and width are measured with respect to the CNT.

What can be observed from figure 6.26 is a defined difference in length and width. The mean width for E111 azF is measured as 22.0 nm compared to the mean length at 12.6 nm. As with the R80 azF variant, the width of the protein is approximately double the length of the protein. This is expected for sfGFP E111 azF, but not for sfGFP R80 azF.

6.5.3 sfGFP 132 azF

The next variant, sfGFP 132 azF, is analogous to sfGFP R80 azF however the azF is now located at the opposite end of the GFP barrel as is shown in 6.27. Once again, height profiles are taken for proteins covalently bound to SWCNT's deposited onto glass cover-slips from AFM topography maps (a representative topography for the variant sfGFP 132 azF can be found in figure 6.28). The expected height for this variant is 4.2 nm as the position of the 132 residue places the azF on the short axis

Figure 6.23: A representation of the protein variant sfGFP E111 azF. The chromophore is shown at the centre of the barrel like structure of the sfGFP and the azF is shown at residue 111

of the GFP protein barrel structure. It is therefore expected that any ratio between length and width of the protein should be 1:1, as the symmetrical barrel top should be on display.

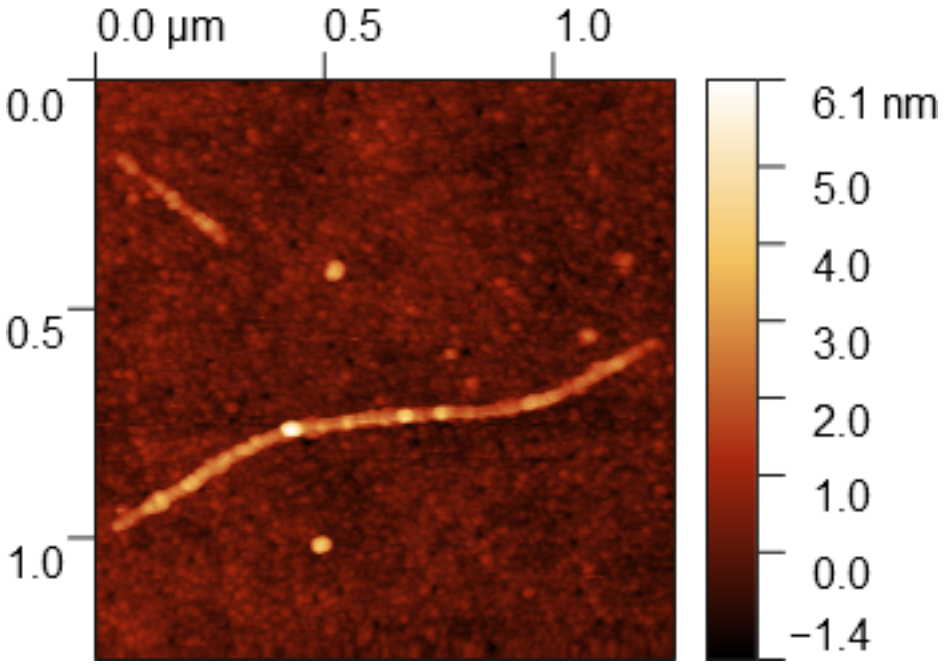

Figure 6.24: AFM topography for a sSWCNT on glass cover-slip functionalised with 100 nMol E111 sfGFP. 2018-05-17.017. Image size: 1.25 μm x 1.25 μm.

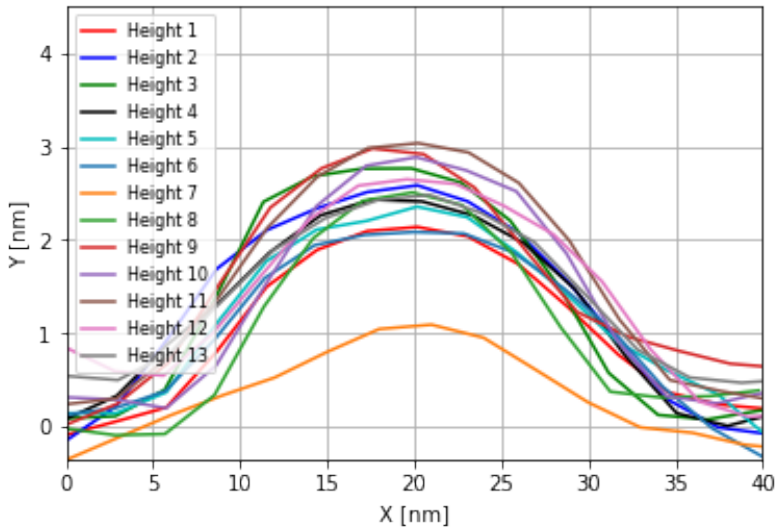

Figure 6.25: Height profiles for covalently bound sfGFP E111 azF on single wall carbon nanotubes deposited on glass cover-slip from AFM topographies.

In figure 6.29 the height profile of the bare nanotube as measured using AFM methods is shown as height profile 8, all other height profiles were taken directly over what can be perceived as proteins. Comparing the height profiles of sfGFP 132 azF to sfGFP R80azF and sfGFP E111 azF shows a larger observed protein height. In figure 6.30 it is observed that the width and length of the protein bound to the tube is very similar with the mean length of the protein calculated to

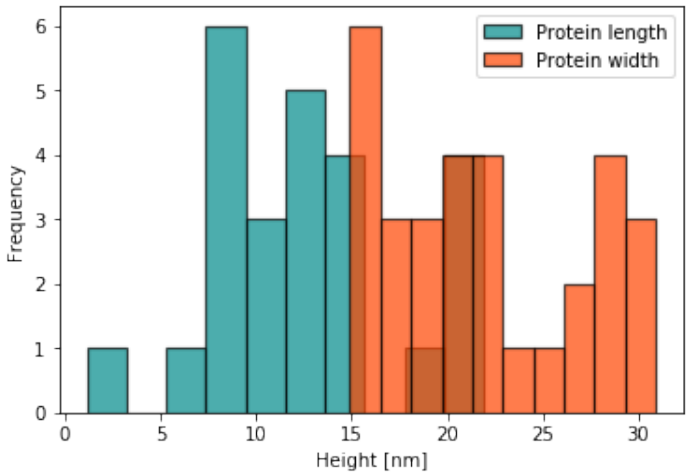

Figure 6.26: A histogram to demonstrate the ratio of length to width of sfGFP 111 azF covalently bound to single wall carbon nanotubes deposited on glass cover-slip from AFM topographies.

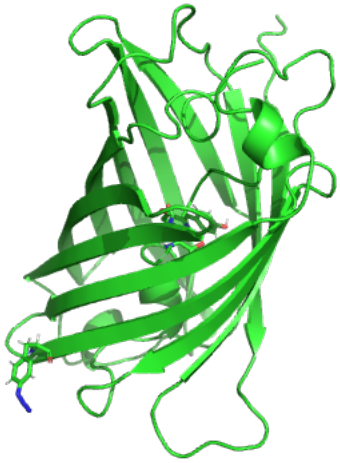

Figure 6.27: A representation of the protein variant sfGFP 132 azF. The chromophore is shown at the centre of the barrel like structure of the sfGFP and the azF is shown at residue 132

be 36.5 nm and the mean width 34.1 nm. Combining this with what is shown in the height data it is possible to infer that sfGFP 132 azF is binding directly on top of the tube and the top of the barrel is the region of the protein that is measured by AFM. This is a direct contrast to the sfGFP R80 azF, in which the azF is located at the opposite end of the barrel structure, where it was theorised from the data recovered that the protein was binding to the side of the CNT, and not on the top of the curvature.

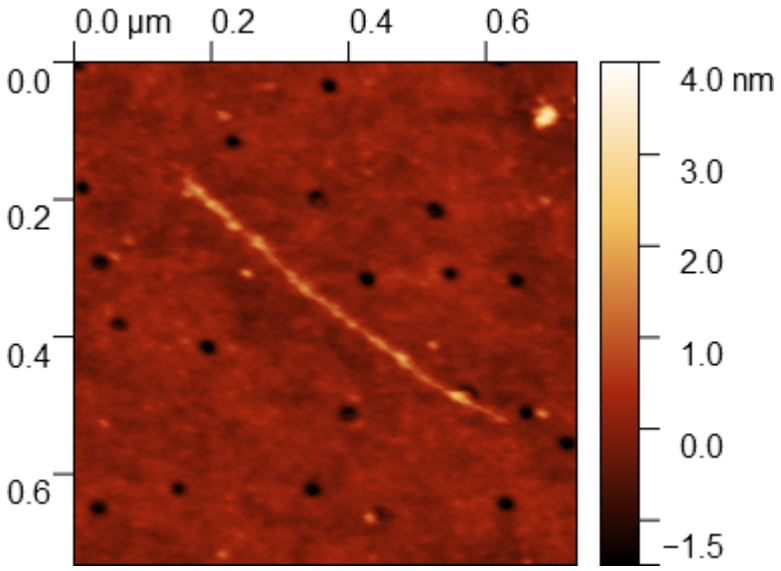

Figure 6.28: AFM topography for a sSWCNT on glass cover-slip functionalised with 100 nMol 132 sfGFP. 2018-07-12.015. Image size: 0.7 μm x 0.7 μm.

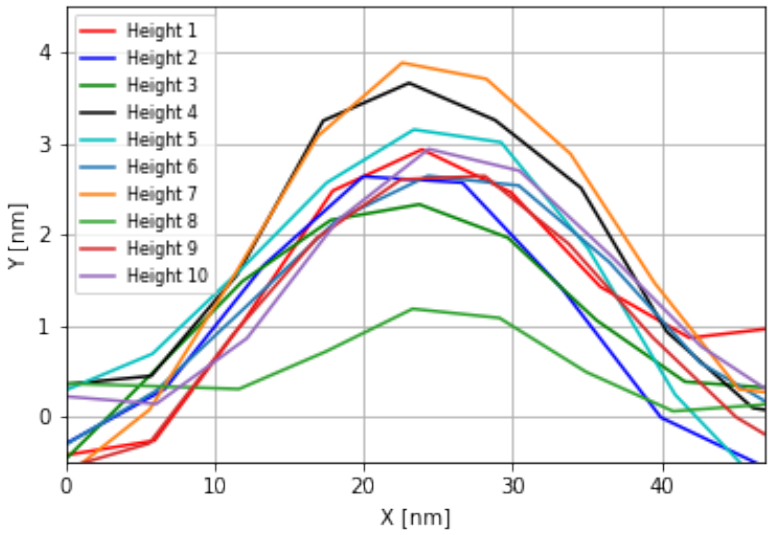

Figure 6.29: Height profiles for covalently bound sfGFP 132 azF on single wall carbon nanotubes deposited on glass cover-slip from AFM topographies.

6.5.4 sfGFP 204 azF

The final sfGFP variant is sfGFP 204 azF. This protein is analogous to the E111 azF variant as the location of the azF group is on the side of the barrel structure of the protein as can be seen in the graphic presented in figure 6.31. It is expected that the height of the protein should show as approximately 2.4 nm above the nanotube when visualised with AFM methods, however as we have experienced with each of the previous proteins imaged, the actual value recorded for protein height is

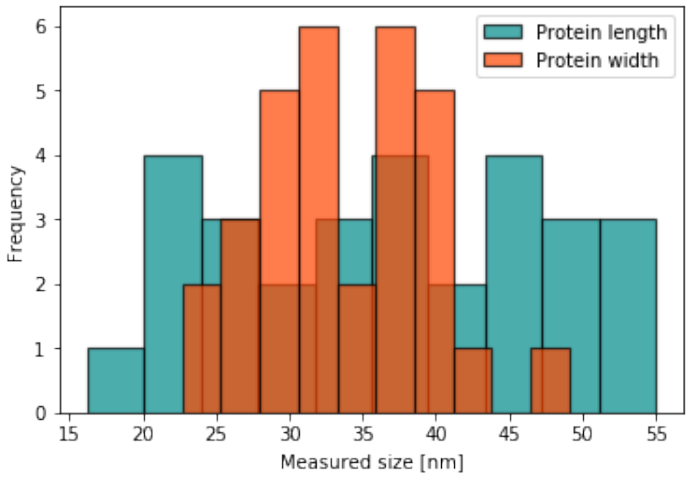

Figure 6.30: A histogram to demonstrate the ratio of length to width of sfGFP 132 azF covalently bound to single wall carbon nanotubes deposited on glass cover-slip from AFM topographies.

somewhat lower as is shown in figure 6.33 where profile 5 is the bare tube and all other profiles are perceived proteins. A representative topography for sfGFP 204 azF can be found in figure 6.32.

Figure 6.31: A representation of the protein variant sfGFP 204 azF. The chromophore is shown at the centre of the barrel like structure of the sfGFP and the azF is shown at residue 204.

By taking a comparison of length and width of the proteins bound to the CNT it is expected that one of these measurements should be observed to be double that of the other. This is due to the fact that the location of the azF implies the binding of the protein such that the length of the barrel (4.2 nm) lies either across

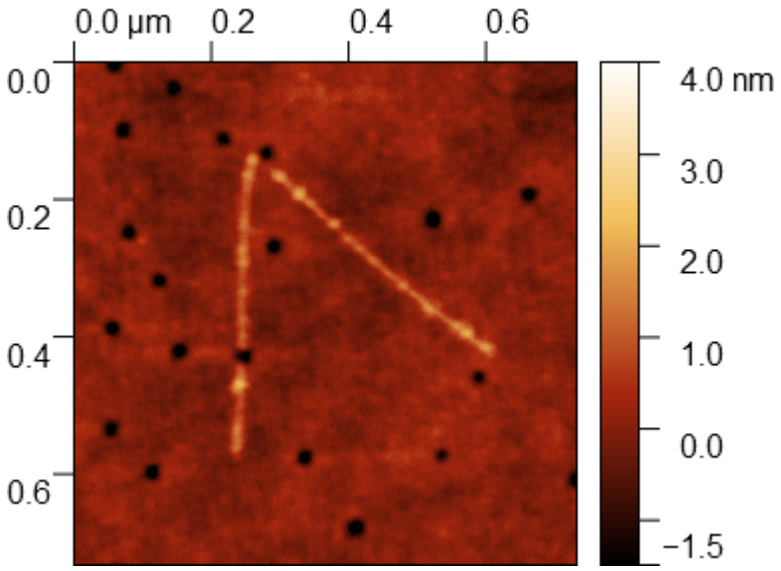

Figure 6.32: AFM topography for a sSWCNT on glass cover-slip functionalised with 100 nMol 204 sfGFP. 2018-05-13.010. Image size: 0.7 μm x 0.7 μm.

or along the tube. In figure 6.34 the recorded width of the protein is larger than the recorded length implying that the protein is lying such that the length of the barrel of the protein is across the tube and the width of the barrel is along the tube. Looking at the statistics of this data, the mean length of the protein measurements is 24.2 nm whereas the mean width is calculated to be 36.3 nm. From the overlap in the data sets and the broad spread in length, an argument could be made that a small amount of the measured proteins lie with the barrel width across the tube and the barrel length along the tube, but they would be in the minority.

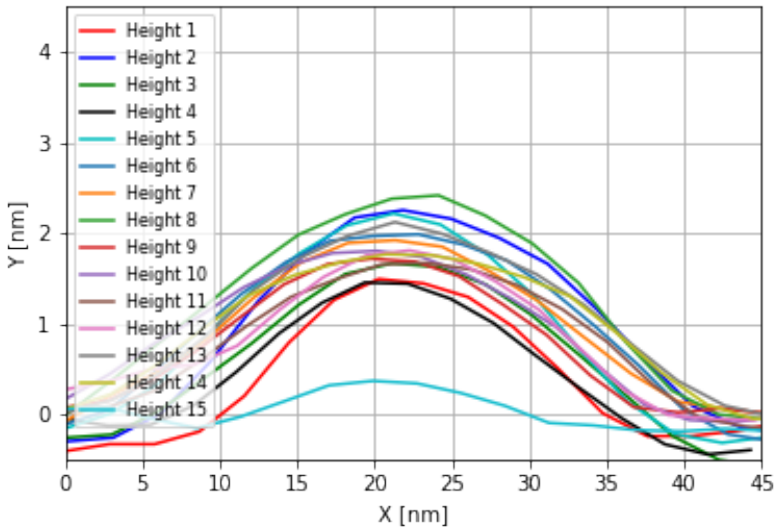

Figure 6.33: Height profiles for covalently bound sfGFP 204-azF on single wall carbon nanotubes deposited on glass cover-slip from AFM topographies.

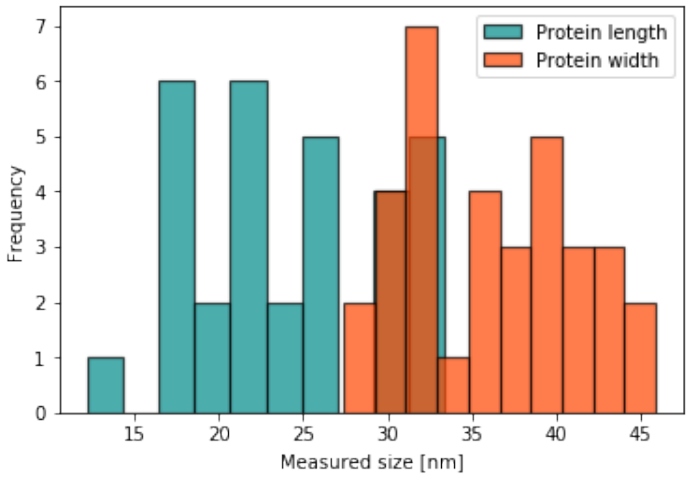

Figure 6.34: A histogram to demonstrate the ratio of length to width of sfGFP 204-azF covalently bound to single wall carbon nanotubes deposited on glass cover-slip from AFM topographies

6.5.5 Conclusions

By creating variants of the sfGFP with different azF sites it has been possible alter the orientation of binding of the protein to carbon nanotubes. This has provided a perfect platform to investigate the pros and cons of AFM methods in determining the height of the bound protein, the location of the protein in relation to the CNT, and the orientation of the protein on or around the CNT.

Using AFM methods to deduce the orientation of proteins bound to CNT's allows data to be obtained for protein height, width and length. However due to the combination of the requirement for a dry sample, the force of the tip on the soft protein and the convolution of image caused by the tip, any data collected can be inconsistent. The heights of the proteins are consistently reduced and the lengths and widths consistently increased. By comparing relative values some information about the orientation may be derived. For example: it is possible to state that the protein variant sfGFP R80azF appears to be binding to the side of the nanotube curvature, and not to the top of the CNT, unlike the analogous variant sfGFP 132azF which shows a much larger height measurement and an approximate 1:1 length to width ratio. Similarly the variants sfGFP E111azF and 204azF show similar length to width histogram characteristics. Both are observed to have a larger width than

length, with a small overlap in recorded results implying that generally the protein binds with the length of the barrel across the tube, but for a small number of protein binding events the opposite case may be true. It is impossible to be sure that this data tells the full story of the orientation of the protein binding, and it would be advisable to use alternative methods which may be more precise in conjunction with AFM data.

6.6 Beta lactamase inhibitor protein as a detector for TEM beta-lactamase

The overall goal of this project has been to create a working bio-sensing device. In order to create such a system, the analyte which is to be detected must first be decided. TEM β-lactamases are a class of proteins produced when a bacteria is resistant to beta-lactam based antibiotics, which are the most commonly used in medicine [76]. These proteins are inhibited by a class of proteins known as beta lactamase inhibitor proteins (BLIP), which bind the TEM proteins to them. By engineering an azF functionalised BLIP it is hoped a bio-sensor may be developed to detect β-lactam proteins.

The first step in this process is to observe the binding of the BLIP to carbon nanotubes using AFM methods and then measure again after TEM addition. In this case it is necessary to observe the same tube pre and post TEM addition, therefore cover-slips patterned with a grid were employed allowing a smaller search area for scanning.

The BLIP variant used within these experiments is BLIP II 41azF, as shown in figure 6.35. The position of the azF on the protein allows the active binding site of the BLIP to be easily accessible to the analyte after binding to CNT sidewall. Due to the location of the binding site it is expected that through AFM methods, the analyte protein will be observed filling in the gaps left by the BLIP. This should be proved by: a lack of significant height change (as the TEM is not binding to the top of the BLIP), and a change in profile along the tube. As has been shown in

earlier experiments, the location of the azF may also result in the binding site on the BLIP allowing the TEM analyte to bind to the side of the carbon nanotube and not along its length. However experimental results do not indicate that this is the case.

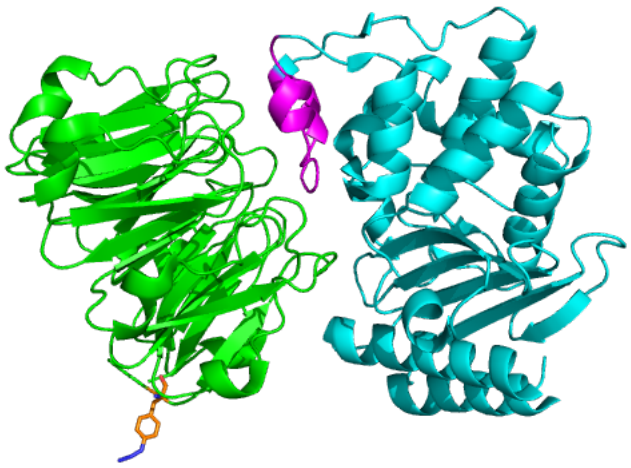

Figure 6.35: β-lactamase inhibitor protein (BLIP II) in green. The azide-phenylalanine photo-chemical reaction handle is located at residue 41, and is shown in orange and blue at the bottom of the BLIP II. In blue: the enzyme TEM-1 enzyme is shown with the active site in pink. This also illustrates the binding mechanics between the BLIP II and TEM-1.

To bind the BLIP experimentally, SWCNT's in 1% SDS solution were drop cast onto plasma cleaned gridded glass cover-slips. The droplet of CNT's was allowed to dry in air. Once dry the cover-slip was rinsed under flowing DI water and flowing ethanol, followed by a 1 hour bath in room temperature ethanol. After soaking the cover-slip was subjected to a further rinse with flowing ethanol followed by flowing DI water to remove any ethanol and finally dried in flowing N_2. After preparation of the cover-slip is complete, the sample is placed into a low humidity glove box wherein an LED of 305 nm wavelength can be located. The room is darkened and the glove-box is shielded against UV light. A droplet of 20 μl of 10 nMol BLIP II 41 azF was drop-cast onto the sample and the LED, positioned above the droplet, was switched on. The sample was illuminated for 5 minutes under the 305nm wavelength light to bind the azF to the CNT, after which time it was switched off and the sample rinsed for 30 seconds to 1 minute to rinse away any unbound protein. The sample was finally dried in flowing N_2 within the glove-box and then removed to be attached

to an AFM sample puck.

The BLIP II 41 azF sample was then scanned using AFM methods, a location on the sample was chosen to be close to one of the gridded numbers to allow the same tube to be visualised post TEM addition. A tube of above average length (≈1.3 μm) was selected for scanning, the AFM image for which can be found in figure 6.36

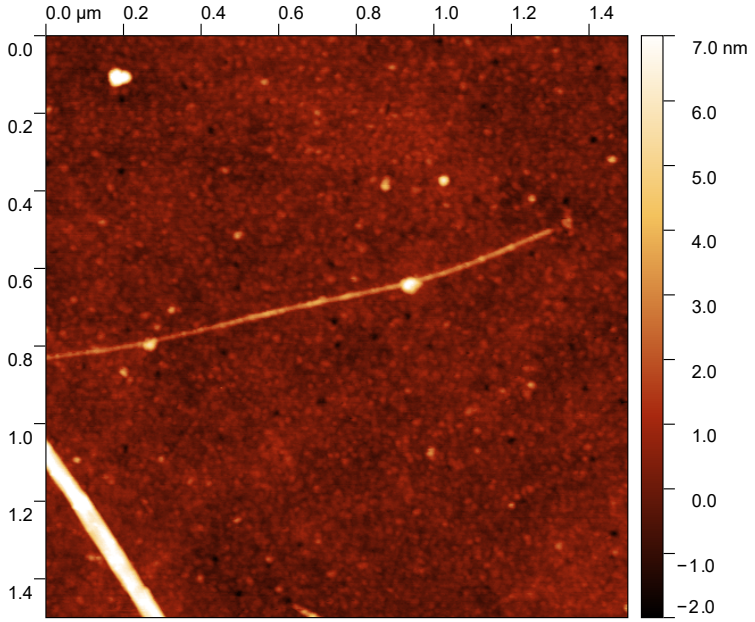

Figure 6.36: AFM topography data for BLIP II 41 azF covalently bound to SWCNTs on a gridded glass cover-slip. Image size: 1.5 μm x 1.5 μm.

By using a low concentration of the BLIP II 41 azF protein visualising the protein attached to the nanotube is possible using only the AFM image. However, it is prudent to perform height analysis to show that the presumed bound protein display an expected height difference. Figure 6.37 shows this height analysis for selected proteins along the tube in figure 6.36.

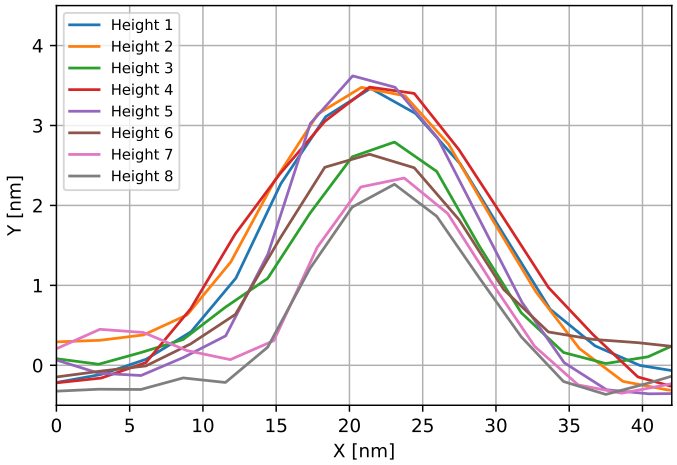

Figure 6.37: Height analysis of proteins along a carbon nanotube decorated with covalently bound BLIP II 41 azF protein

Once it has been confirmed that BLIP II 41 azF has been successfully bound, the analyte (TEM-1) was added to the sample. A 20 μl droplet of 100nMol TEM was drop-cast onto the sample in ambient conditions. The sample was left for 5 minutes to allow binding to occur and then rinsed in flowing DI water for 30 seconds to 1 minute to allow any unbound analyte to be rinsed away. A relatively high concentration of the analyte was selected to allow maximum binding to the bound BLIP, in a bio-sensing device in order to obtain the best signal a minimal amount of protein should be bound to the carbon nanotube and a high concentration of analyte should be added, however this is not always the case in medical situations and the ability to detect small amounts of analyte in a solution is crucial. This would need a much more in depth study to fine tune the bio-sensing device.

Once the TEM has been successfully added to the sample, it is re-scanned using AFM methods. The same tube is located by aligning the tip using the gridded cover-slip. It is then possible to make a direct comparison of pre and post TEM addition. The first comparison shown in figure 6.38 is of the straightened tube pre and post TEM addition, the contrast of the image is altered to better visualise the proteins bound to the CNT.

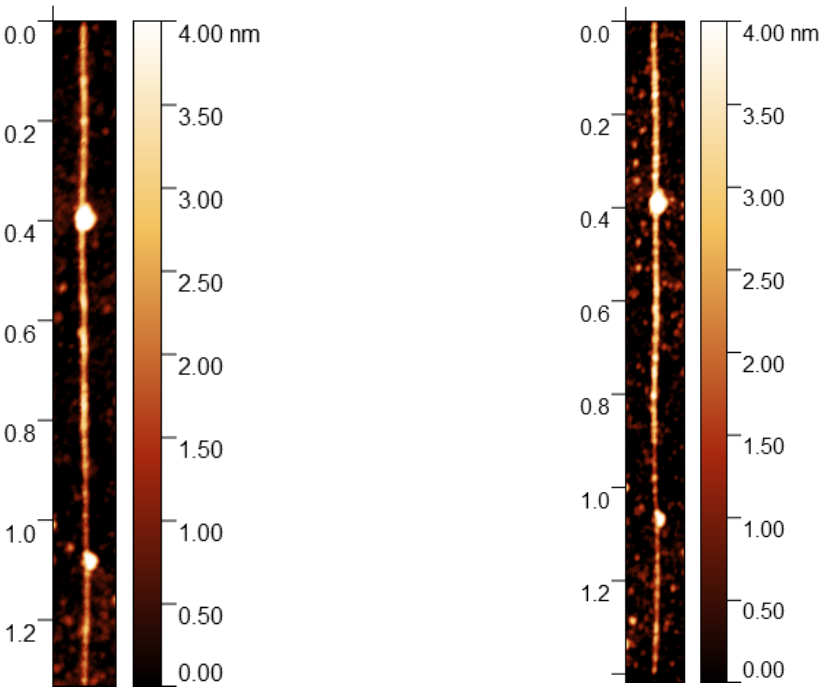

(a) BLIP II 41 azF

(b) BLIP II 41 azF + TEM-1 addition.

Figure 6.38: A comparison of the same tube decorated with BLIP II 41 azF (a) pre TEM-1 addition and (b) post TEM-1 addition taken using AFM methods and adjusted contrast to enhance visualisation of bound protein/analyte

It is clear from figure 6.38 that there is an observable difference between the pre and post TEM addition. It is possible to infer from this that attachment of the TEM-1 analyte has been achieved. Significantly more proteins are observed along the tube, and it is possible to identify proteins from the BLIP image located next to the newly added TEM-1.

After observing the changes to the surface topography, the images can be analysed to obtain height profiles to compare to pre-TEM addition. When comparing figure 6.39 to figure 6.37, there is no significant change in height observed after the addition of TEM. This is to be expected as the active binding site located on the BLIP II 41 azF would produce binding along the tube and not allow the TEM to stack on top of the BLIP.

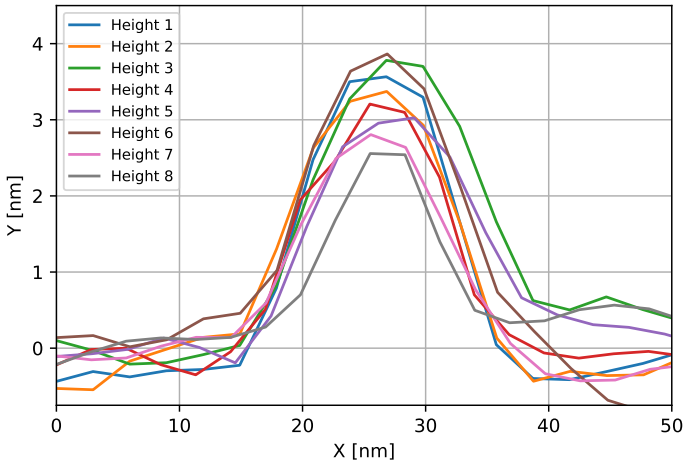

Figure 6.39: Height analysis of proteins along a carbon nanotube decorated with covalently bound BLIP II 41 azF protein and addition of TEM-1 analyte.

Finally by taking profiles along the tube pre and post TEM addition, it is possible to build up a comprehensive view of the additional proteins. The active binding site of the BLIP II 41azF variant should result in the TEM protein binding to the side of the BLIP. What can be observed is that the TEM is binding along the tube in between the gaps left by the BLIP. From this it may be possible to deduce the orientation of the BLIP along the tube. Due to the closeness of binding between the two proteins, observations made from the height profiles do not distinguish TEM-1 and BLIP II.

The tubes were separated into four segments for this analysis. This allowed for easier comparison of the profile peaks. The selections for each section of tube are shown in figure 6.40, which is the straightened tube from the post TEM-1 addition image. For each segment a line profile was taken down the centre of the tube, however as the pre and post TEM-1 addition images were imaged at different times it is difficult to align the profiles exactly. Therefore pre and post profiles are displayed on separate graphs and comparisons are made from this graphical data to determine TEM-1 binding to the BLIP II 41 azF detector protein.

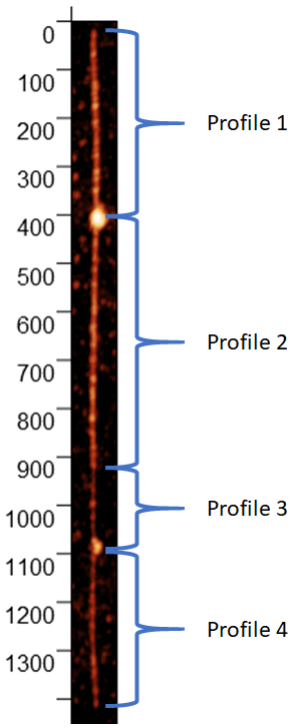

Figure 6.40: Post TEM-1 addition straightened tube highlighting the selections made for profile analysis.

The profiles for pre and post TEM-1 addition are shown side by side, with pre addition on the right, and post addition on the left in figures 6.41 - 6.44. Comparison of these profiles is a strong indication that is TEM-1 binding to the BLIP 11 41 azF protein on the CNT. In each case the average height of the tube is increased, and the number of peaks is increased also. It is clear that the ratio of protein to unfilled tube is increased after the addition of the TEM-1 analyte. We can conclude that TEM-1 binding has occurred.

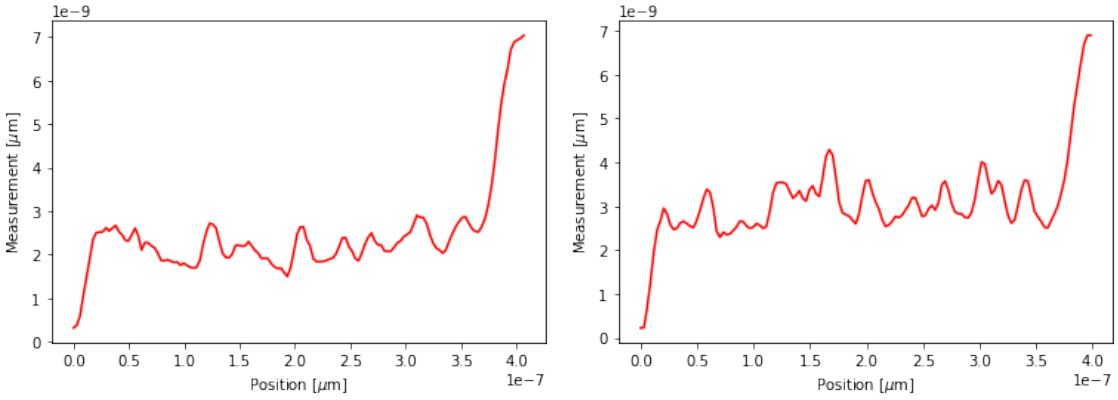

(a) BLIP II 41 azF only

(b) BLIP II 41 azF + TEM-1 addition.

Figure 6.41: Comparison line profiles taken along a BLIP II 41 azF decorated CNT pre and post TEM-1 analyte addition for the section selected as profile 1

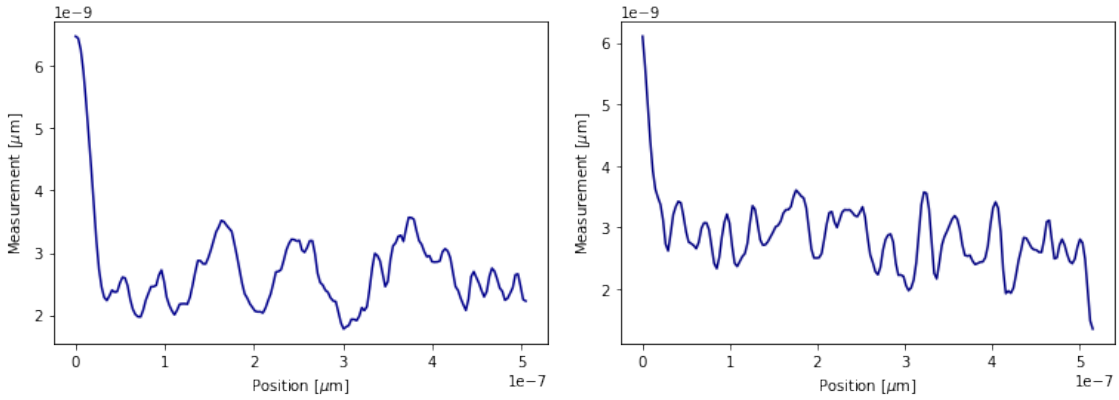

(a) BLIP II 41 azF only (b) BLIP II 41 azF + TEM-1 addition.

Figure 6.42: Comparison line profiles taken along a BLIP II 41 azF decorated CNT pre and post TEM-1 analyte addition for the section selected as profile 2

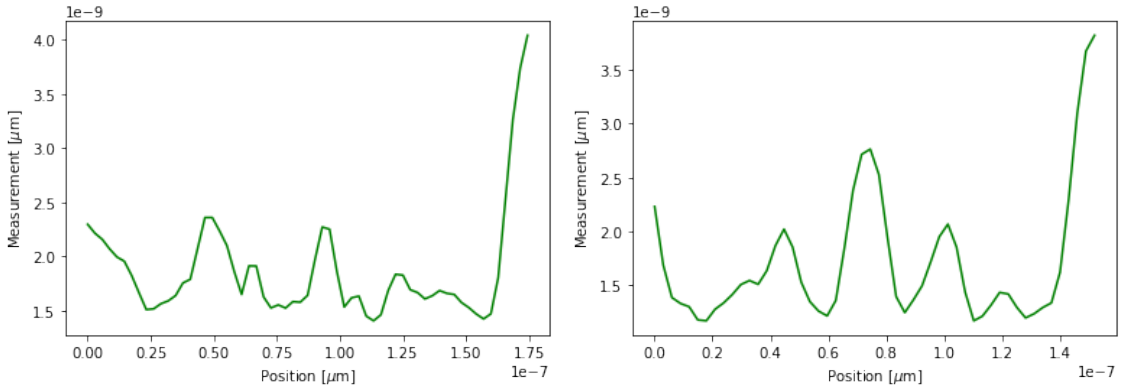

(a) BLIP II 41 azF only (b) BLIP II 41 azF + TEM-1 addition.

Figure 6.43: Comparison line profiles taken along a BLIP II 41 azF decorated CNT pre and post TEM-1 analyte addition for the section selected as profile 3

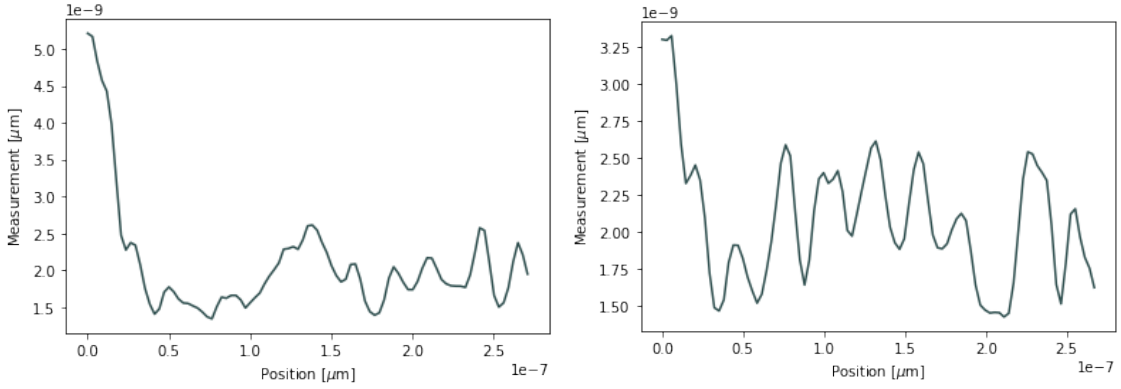

(a) BLIP II 41 azF only (b) BLIP II 41 azF + TEM-1 addition.

Figure 6.44: Comparison line profiles taken along a BLIP II 41 azF decorated CNT pre and post TEM-1 analyte addition for the section selected as profile 4

6.6.1 Electrical measurements of first stage prototype TEM-1 bio-sensors

At the end of the project, an electrical measurement test of a prototype sensing device was attempted. This work was performed in conjunction with Queen Mary University London (QMUL), who created the base component of the device: carbon nanotubes suspended across an electrode array. Unfortunately, due to time constraints only one visit from the QMUL group was possible to perform the experiments in Cardiff.

Electrode arrays were developed by Xinzhao Xu and Dr Mark Freeley of QMUL, with swCNTs bridging the nano-gap between the electrodes to form CNT FET devices. Four electrode arrays were prepared in total, with five electrode pairs per sample. Two of these arrays were designed for AFM characterisation where semiconducting swCNTs dispersed in SDS were immobilised between the electrodes using dielectrophoresis. The height of the nanotubes for these samples was measured to be approximately 10-30 nm, a measured height profile can be found in figure 6.45b. An AFM image of one of these devices is shown in figure 6.45a.

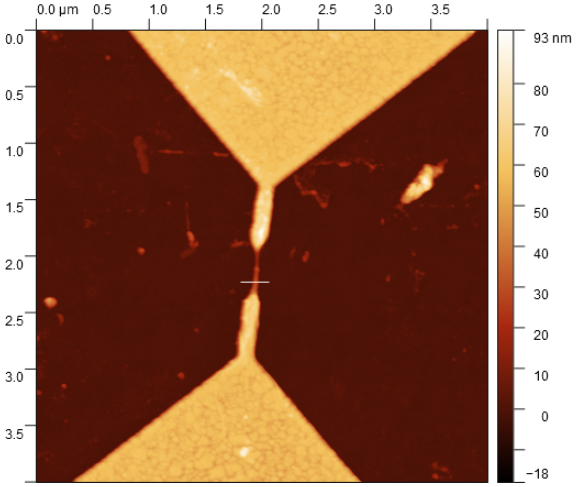

(a) AFM topography, image size: 4.0 μm x 4.0 μm.

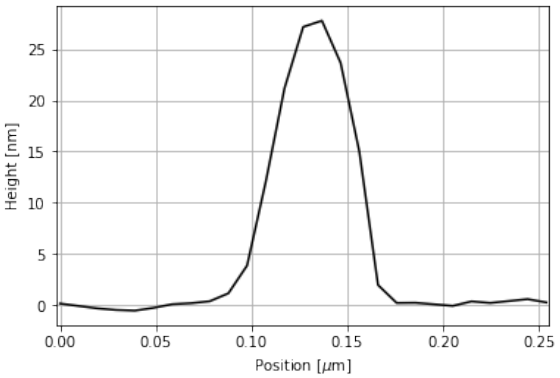

(b) Height profile

Figure 6.45: AFM topography of a CNT FET device before protein addition. The white line denotes the location of the profile taken across the suspended CNT bundle. A height of 27.8 nm was recorded for this CNT bundle.

The second set of samples were designed for electrical measurements and

unfortunately it was not possible for the semiconducting swCNTs dispersed in SDS to be immobilised between these electrodes as the application of an AC electric field between the electrodes causes the electrodes to peel off in the SDS solution. Instead, pure single chirality (6, 5) swCNTs wrapped with DNA were immobilised between the electrodes. The DNA is decomposed by annealing the samples at 200 °C for 6 hours. This should allow enough degradation of the DNA to occur to leave space on the CNT for a photo induced reaction. The 2018 paper by Xinzhao Xu [151] contains further information regarding the electrode formation, and further experiments using this device architecture.

I-V measurements were performed on the devices mounted on a model 210 MicroManipulator probe station using a Keithley 2401 SourceMeter. A measurement was taken prior to the attachment of the BLIP protein to determine viable electrodes and establish a baseline reading, this is shown in figure 6.46a. The electrode arrays were then transferred to a nitrogen filled low humidity glovebox where the BLIP II 41 azF protein (10 nM concentration) was covalently bound to the CNTs. Once the binding process was completed and the device had been rinsed thoroughly in flowing DI water and dried under a N_2 stream, the electrodes were removed from the humidity-controlled environment and taken back to the probe station. The I-V measurement of the viable electrodes were repeated. Primarily this established signal retention to ensure that the CNTs had not been damaged or destroyed during the binding process but also established a new baseline for analyte detection. This is shown in figure 6.46b where a weak change in I-V profile compared to the pristine CNTs is observed.

A real-time measurement of the change in current through the device was attempted on the pristine CNT devices (figure 6.47a and during addition of the TEM analyte (1 μM concentration) to probe any changes in current due to attachment to the BLIP II (figure 6.47b).

It was observed that measurements obtained for the pristine CNT devices were unstable and upon the addition of the analyte protein no clear change was observed. Clearly, these results are inconclusive. Further measurements would require more care to be taken in establishing a stable, noise-reduced current prior to

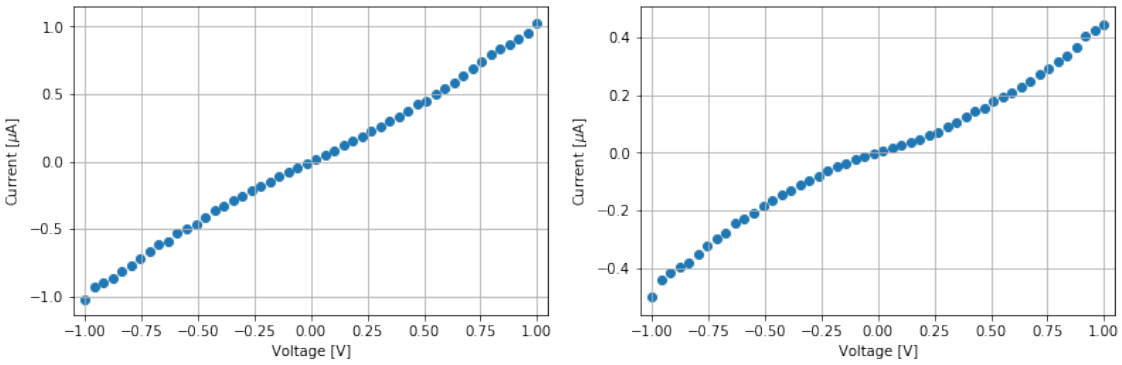

(a) Before protein addition. (b) Post addition of BLIP II 41 azF.

Figure 6.46: Current Voltage characteristics for the CNT FET device pre and post BLIP II 41 azF addition.

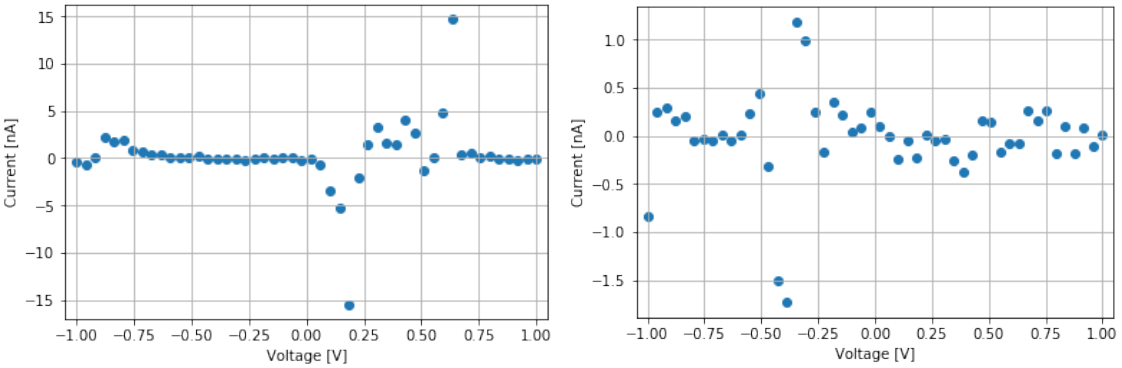

(a) Before protein addition. (b) Post TEM addition.

Figure 6.47: Real time current voltage response measurements to determine changes in device characteristics. (a) shows the response for a pristine CNT FET device, (b) shows the response during addition of TEM analyte to a BLIP II 41 azF decorated CNT FET device. The responses allow observation of changes in device characteristics upon protein - analyte binding in comparison to a pristine CNT FET device.

the addition of the TEM-1 analyte, in order to distinguish changes to the current caused by addition of liquid and the attachment of the TEM to the BLIP. It would be desirable to eliminate the removal of the sample from the humidity-controlled environment, which would require the probe station to be integrated with the nitrogen filled glove-box. Currently this is not possible.

Chapter 7

Conclusions

7.1 Conclusions

The goal of this project has been to create a functional carbon nanostructure based bio-sensing device utilising protein-protein interactions as a detection method for the analyte TEM-1 β-lactamase (TEM-1). The project began by utilising SPM methods to explore the electrostatics of OFET devices. The base of our prospective device was intended to be a FET type of device, therefore the exploration of OFET devices using SPM methods served not only as an effective method to learn key techniques but also as a way to study and develop the base component of our future device.

The study of the DNTT OFET devices, in conjunction with Dr Chang-Hyun Kim, produced interesting new methods for the parameterisation of organic thin films. By taking potential profiles from SKPM data to calculate voltage drop across the electrode-channel interface and across the channel of the devices alongside the transfer characteristics, it was possible to separate effects of contact resistance and the channel and to calculate the channel mobility directly from a single device. The mobility of the film calculated via this method was compared with values calculated solely from transfer characteristics. This showed that the values calculated from only transfer characteristics yielded significantly lower mobilities than the

potentiometric results backed values. Furthermore this study explored the relationship between device structure and defect formation in the thin film. AFM images of channel material showed that TC device structures developed large dendritic grains forming lamellar edges, growing well into a cohesive film. BC and BC-SAM device structures however formed small defects where the much smaller grains failed to coalesce. This study adds further evidence to the superior nature of TC device structures for OFET devices. Furthermore the measurements illustrate clearly the benefits offered by SKPM in characterising the effect of contact resistance on device performance without testing the IV characteristics of hundreds of identical devices.

The experimental experience gained from working with the DNTT devices was then applied to more complex OSC:polymer thin film transistors. Two variants of thin film blends were used, each with a pristine and doped sample. However the experimental methods that worked so well for the DNTT devices did not yield results for these samples. Therefore a new approach to analysis of SKPM potential maps was devised. By taking the magnitude of the gradient of the potential with respect to neighbouring points on the potential image, a map of the electrostatics of the surface can be formed. Areas of high potential gradient imply a highly resistive region. This allowed for a more detailed surface map to be obtained that was present in AFM topography images. From this data is was made clear that for the second OSC:polymer blend, the mixing of the materials was less uniform than for the first blend. Grain boundaries were clearly visible exhibiting a large potential gradients at the boundaries, these effects were also observed at the electrode channel interface.

After the investigations using SKPM methods it was determined that in order to obtain the resolution required for a bio-sensing detection, a new method would need to be devised. By applying an AC bias to the tip during lift mode scanning, the contributions of the cantilever to scanning resolution are restricted to the tip apex implying a much improved scanning resolution. However, in practice this method proved to be too unpredictable experimentally, and data analysis too time consuming to be of use to this study. Therefore electrical measurements using a probe station were chosen to be the method of detection for the proposed bio-sensing device.

Taking the skills from AFM and SKPM, protein binding to carbon nanostructures was investigated. The first step in the study was to confirm retention of protein activity. This was performed using confocal microscopy for large area graphene, and TIRF microscopy for carbon nanotubes using GFP as it is easy to visualise activity in the form of fluorescence. Once the activity was confirmed, the study progressed to AFM methods of protein height changes and the effect of azF placement about the protein structure. What was discovered was that AFM methods are very useful in determining changes to protein height. This was performed by splitting a dimer form of cytochrome into two monomers and observing the change. Using AFM it was also possible to confirm differences in protein positioning on the surface of the carbon nanotube. However, due to tip convolutions this is less reliable than height changes.

In order to attain the goal of a bio-sensing device, a protein and analyte were studied. By binding the protein BLIP II to CNTs and observing the height profiles before and after the addition of the TEM-1 analyte, it was possible to present a significant difference in protein coverage of the swCNT. This implies that the BLIP II protein is active, and that the analyte is binding to the BLIP II along the nanotube in between gaps left by the BLIP. This was the first step towards a bio-sensing device, with the next step being a prototype device to test using a probe station to observe any electrical changes.

A prototype device was developed by QMUL: an array of CNTs bridging electrodes. By observing the electrical changes in the device before and after BLIP II addition and the further changes in real time, after analyte addition, it was hoped that a bio-sensing device would be created. However, the results of these experiments were inconclusive at this time, and further work on this project is currently underway.

7.2 Future work

Although this work made a lot of progress towards the end goal of the project to develop a bio-sensing device, there is still much more work to be done. By continuing studies into EFM-phase methods and analysis of results obtained from this could prove very helpful in the identification of protein binding combining the visual confirmation of AFM with the data obtained using SKPM or current-voltage measurements. EFM-phase is a very interesting technique for not only protein interactions but other potentiometric changes at the nanoscale level that SKPM is not sensitive enough to pick up. Before EFM-phase is a viable method the collection of data needs to be standardised such that the scanning parameters can be quickly and effectively set, as currently this is one of the main areas where the technique loses time effectiveness. The second area that needs development is the analysis. At present, due to the non-standardised nature of each scan, the parameters for analysis need to be set on a case by case basis: again time is lost perfecting each parameter.

Further studies may also include reproducing and optimising the prototype devices provided by QMUL, perhaps by isolating single proteins by using DNA wrapped nanotubes to restrict binding to a periodic region of bare CNT. It is hoped that this design will prove successful with the BLIP-TEM system, and eventually be developed across multiple protein-analyte detection's.

Bibliography

[1] Irina V. Zaporotskova et al. "Carbon nanotubes: Sensor properties. A review". In: *Modern Electronic Materials* 2.4 (2016), pp. 95–105. ISSN: 2452-1779. DOI: https://doi.org/10.1016/j.moem.2017.02.002. URL: http://www.sciencedirect.com/science/article/pii/S2452177917300178.

[2] Mohammed Al-Talib and Isla Leslie. "Speeding up laboratory test reporting in Medical Emergency and Cardiac Arrest calls: a quality improvement project". In: *BMJ quality improvement reports* 6.1 (2017). DOI: 10.1136/bmjquality.u213103.w5207.

[3] Jeffrey Kirsch et al. "Biosensor technology: recent advances in threat agent detection and medicine". In: *Chem. Soc. Rev.* 42.22 (2013), pp. 8733–8768. DOI: 10.1039/C3CS60141B. URL: http://dx.doi.org/10.1039/C3CS60141B.

[4] Wenzhao Jia et al. "Electrochemical Tattoo Biosensors for Real-Time Noninvasive Lactate Monitoring in Human Perspiration". In: *Anal. Chem.* 85.14 (2013), pp. 6553–6560. DOI: 10.1021/ac401573r. URL: https://doi.org/10.1021/ac401573r.

[5] Kathleen E Mach, Pak Kin Wong, and Joseph C Liao. "Advances and challenges in biosensor-based diagnosis of infectious diseases". In: *Expert review of molecular diagnostics* 14.2 (2014), pp. 225–244. DOI: 10.1586/14737159.2014.888313.

[6] Stuart B Levy and Bonnie Marshall. "Antibacterial resistance worldwide: causes, challenges and responses". In: *Nature Medicine* 10 (2004). DOI: 10.1038/nm1145. URL: https://doi.org/10.1038/nm1145.

[7] John F. Prescott. "The resistance tsunami, antimicrobial stewardship, and the golden age of microbiology". In: *Veterinary Microbiology* 171.3 (2014), pp. 273–278. DOI: https://doi.org/10.1016/j.vetmic.2014.02.035. URL: http://www.sciencedirect.com/science/article/pii/S0378113514001254.

[8] Julian Davies and Dorothy Davies. "Origins and Evolution of Antibiotic Resistance". In: *Microbiology and Molecular Biology Reviews* 74.3 (2010), pp. 417–433. DOI: 10.2307/26057703. URL: https://mmbr.asm.org/content/74/3/417.

[9] Stuart B. Levy. "The Challenge of Antibiotic Resistance". In: *Scientific American* 278.3 (1998), pp. 46–53. DOI: 10.1128/MMBR.00016-10. URL: http://www.jstor.org/stable/26057703.

[10] Claas Kirchhelle. "Pharming animals: a global history of antibiotics in food production (1935-2017)". In: *Palgrave Communications* 4.1 (2018). DOI: 10.1057/s41599-018-0152-2. URL: https://doi.org/10.1057/s41599-018-0152-2.

[11] David M. Livermore and Neil Woodford. "The β-lactamase threat in Enterobacteriaceae, Pseudomonas and Acinetobacter". In: *Trends in Microbiology* 14.9 (2006), pp. 413–420. ISSN: 0966-842X. DOI: https://doi.org/10.1016/j.tim.2006.07.008. URL: http://www.sciencedirect.com/science/article/pii/S0966842X06001818.

[12] Karen Bush and Jed F Fisher. "Epidemiological expansion, structural studies, and clinical challenges of new β-lactamases from gram-negative bacteria." In: *Annual review of microbiology.* 65 (2011), pp. 455–478. ISSN: 0066-4227.

[13] C Damblon et al. "The catalytic mechanism of beta-lactamases: NMR titration of an active-site lysine residue of the TEM-1 enzyme." In: *Proceedings of the National Academy of Sciences of the United States of America* 93 (5 1996), pp. 1747–1752. URL: https://www.ncbi.nlm.nih.gov/pubmed/8700829.

[14] Yian-Biao Zhang et al. "Functionalized Carbon Nanotubes for Detecting Viral Proteins". In: *Nano Letters* 7.10 (2007), pp. 3086–3091. DOI: 10.1021/

nl0715721. eprint: https://doi.org/10.1021/nl0715721. URL: https://doi.org/10.1021/nl0715721.

[15] B. L. Allen, P. D. Kichambare, and A. Star. "Carbon Nanotube Field-Effect-Transistor-Based Biosensors". In: *Advanced Materials* 19.11 (2007), pp. 1439–1451. DOI: 10.1002/adma.200602043. eprint: https://onlinelibrary.wiley.com/doi/pdf/10.1002/adma.200602043. URL: https://onlinelibrary.wiley.com/doi/abs/10.1002/adma.200602043.

[16] G. Binnig, C. F. Quate, and Ch. Gerber. "Atomic Force Microscope". In: *Phys. Rev. Lett.* 56 (9 Mar. 1986), pp. 930–933. DOI: 10.1103/PhysRevLett.56.930. URL: http://link.aps.org/doi/10.1103/PhysRevLett.56.930.

[17] Wenjie Mai. *Fundamental Theory of Atomic Force Microscopy*. URL: http://www.nanoscience.gatech.edu/zlwang/research/afm.html.

[18] Yashvant. *Opensource Handbook of Nanoscience and Nanotechnology*. URL: https://en.wikibooks.org/wiki/Nanotechnology/AFM#/media/File:AFMsetup.jpg.

[19] Nanoscience Instruments. *Atomic Force Microscopy*. URL: https://www.nanoscience.com/techniques/atomic-force-microscopy/.

[20] Anja Boisen, Ole Hansen, and Siebe Bouwstra. "AFM probes with directly fabricated tips". In: *Journal of Micromechanics and Microengineering* 6.1 (1996), pp. 58–62. DOI: 10.1088/0960-1317/6/1/012. URL: https://doi.org/10.1088%2F0960-1317%2F6%2F1%2F012.

[21] T. R. Albrecht et al. "Microfabrication of cantilever styli for the atomic force microscope". In: *Journal of Vacuum Science & Technology A* 8.4 (1990), pp. 3386–3396. DOI: 10.1116/1.576520. URL: https://doi.org/10.1116/1.576520.

[22] Sergei N. Magonov and Myung-Hwan Whangbo. *Surface Analysis with STM and AFM : Experimental and Theoretical Aspects of Image Analysis*. Wiley-VCH, 1996. ISBN: 9783527293131. URL: http://search.ebscohost.com/login.aspx?direct=true&AuthType=cookie,ip,shib,uid&db=nlebk&AN=246676&site=ehost-live&scope=site&authtype=shib&custid=s8000044.

[23] Peter Eaton and Paul West. *Atomic Force Microscopy*. Oxford University Press, 2010. ISBN: 978-0-19-957045-4.

[24] Ricardio García and Rubén Pérez. "Dynamic atomic force microscopy methods". In: *Surface Science Reports* 47.6 (2002), pp. 197–301. DOI: https://doi.org/10.1016/S0167-5729(02)00077-8. URL: http://www.sciencedirect.com/science/article/pii/S0167572902000778.

[25] Yagun Zhao et al. "Phase image contrast mechanism in intermittent contact atomic force microscopy". In: *Journal of Applied Physics* 108.9 (2010), p. 094311. DOI: 10.1063/1.3503478. eprint: https://doi.org/10.1063/1.3503478. URL: https://doi.org/10.1063/1.3503478.

[26] Park Systems. *Electrostatic Force Microscopy (EFM)*. URL: http://www.parkafm.com/index.php/park-spm-modes/93-dielectric-piezoelectric/228-electric-force-microscopy-efm.

[27] Electrotechnical Insitute Wroclaw. *The description of Surface Potential/Kelvin Probe AFM*. URL: http://www.iel.wroc.pl/zmmp/badania/serv_AFM_gal_8_EN.html.

[28] Wilhelm Melitz et al. "Kelvin probe force microscopy and its application". In: *Surface Science Reports* 66.1 (2011), pp. 1–27. DOI: https://doi.org/10.1016/j.surfrep.2010.10.001. URL: http://www.sciencedirect.com/science/article/pii/S0167572910000841.

[29] Bruker. *PeakForce Kelvin Probe Microscopy*. URL: https://www.bruker.com/fileadmin/user_upload/8-PDF-Docs/SurfaceAnalysis/AFM/ApplicationNotes/AN140-RevA1-PeakForce_KPFM-AppNote.pdf.

[30] Nanotechnology Solutions Partner. *Scanning Kelvin Probe Microscopy (SKPM)*. URL: http://www.parkafm.com/images/spmmodes/dielectric/7_Scanning-Kelvin-Probe-Microscopy-(SKPM).pdf.

[31] J. Colchero, A. Gil, and A. M. Baró. "Resolution enhancement and improved data interpretation in electrostatic force microscopy". In: *Phys. Rev. B* 64 (24 2001), p. 245403. DOI: 10.1103/PhysRevB.64.245403. URL: http://link.aps.org/doi/10.1103/PhysRevB.64.245403.

[32] B. Bhushan and H. Fuchs. *Applied Scanning Probe Methods II: Scanning Probe Microscopy Techniques*. Germany: Springer-Verlag Berlin Heidelberg, 2006.

[33] C. H. Lei et al. "Conductivity of Macromolecular Networks Measured by Electrostatic Force Microscopy". In: *Appl. Phys. Lett.* 83 (3 2003), pp. 482–484. DOI: 10.1063/1.1592888. URL: http://scitation.aip.org/content/aip/journal/apl/83/3/10.1063/1.1592888.

[34] M. Minsky. "Memoir on inventing the confocal scanning microscope". In: *Scanning* 10.4 (1988), pp. 128–138. DOI: 10.1002/sca.4950100403. eprint: https://onlinelibrary.wiley.com/doi/pdf/10.1002/sca.4950100403. URL: https://onlinelibrary.wiley.com/doi/abs/10.1002/sca.4950100403.

[35] Michael J Sanderson et al. "Fluorescence microscopy". In: *Cold Spring Harbor protocols* 2014.10 (2014). DOI: 10.1101/pdb.top071795. URL: https://www.ncbi.nlm.nih.gov/pubmed/25275114.

[36] James B. Pawley. *Handbook of Biological Confocal Microscopy*. Springer, 2010. ISBN: 978-0-387-25921-5. DOI: https://doi.org/10.1007/978-0-387-45524-2.

[37] The Institue of Molecular Bioscience of The University of Queensland. *Confocal Microscopes*. URL: https://imb.uq.edu.au/facilities/microscopy/hardware-software/confocal-microscopes.

[38] Jeremy M. Berg, John L. Tymoczko, and Lubert Stryer. *Biochemistry*. W. H. Freeman and Company. ISBN: 978-1-4292-7635-1.

[39] Dipika V Patel and Charles NJ McGhee. "Contemporary in vivo confocal microscopy of the living human cornea using white light and laser scanning techniques: a major review". In: *Clinical & Experimental Ophthalmology* 35.1 (2007), pp. 71–88. DOI: 10.1111/j.1442-9071.2007.01423.x. eprint: https://onlinelibrary.wiley.com/doi/pdf/10.1111/j.1442-9071.2007.01423.x. URL: https://onlinelibrary.wiley.com/doi/abs/10.1111/j.1442-9071.2007.01423.x.

[40] D. Axelrod. "Cell-substrate contacts illuminated by total internal reflection fluorescence." In: 89.1 (1981), pp. 141–145. DOI: 10.1083/jcb.89.1.141. URL: http://jcb.rupress.org/content/89/1/141.

[41] Herbert Schneckenburger. "Total internal reflection fluorescence microscopy: technical innovations and novel applications". In: *Current Opinion in Biotechnology* 16.1 (2005), pp. 13–18. DOI: https://doi.org/10.1016/j.copbio.2004.12.004. URL: http://www.sciencedirect.com/science/article/pii/S0958166904001697.

[42] Z. Dechun. "Chemical and photophysical properties of materials for OLEDs". In: *Organic Light-Emitting Diodes (OLEDs), Materials Devices, and Applications* (2013), pp. 114–142. DOI: https://doi.org/10.1533/9780857098948.1.114. URL: http://www.sciencedirect.com/science/article/pii/B978085709425450004X.

[43] J. T. Wallmark and L. G. Carlstedt. *Field-Effect Transistors in Integrated Circuits*. The Macmillan Press LTD, 1971.

[44] Edward S. Yang. *Fundamentals of Semiconductor Devices*. McGraw-Hill Book Company, 1978. ISBN: 0-07-072236-6.

[45] Technische Universität Dresden. *Electrical conductivity in doped organic semiconductors*. 2019. URL: www.sciencedaily.com/releases/2019/01/190129124401.htm.

[46] S. Abroug, F. Saadallah, and N. Yacoubi. "Optical and thermal properties of doped semiconductor". In: *The European Physical Journal Special Topics* 153 (2008), pp. 29–32. DOI: 10.1140/epjst/e2008-00386-7. URL: https://doi.org/10.1140/epjst/e2008-00386-7.

[47] Robert F. Pierret. *Volume I: Semiconductor Fundamentals Second Edition*. USA: Addison-Wesley Publishing Company Inc., 1987. ISBN: 0-201-12295-2.

[48] HyperPhysics. *The Doping of Semiconductors*. URL: http://hyperphysics.phy-astr.gsu.edu/hbase/Solids/dope.html.

[49] Sima Dimitrijev. *Principles of Semiconductor Devices*. Oxford University Press, 2006. ISBN: 978-0-19-989634-9.

[50] *Integrated circuits, photodiodes and organic field effect transistors Robert McIntire and Pierre Donnell, editors.* Environmental Research Advances. New York: Nova Science Publishers, 2009. ISBN: 1-61761-868-3.

[51] M. Halik et al. "Polymer Gate Dielectrics and Conducting-Polymer Contacts-for High-Performance Organic Thin-Film Transistors". In: *Advanced Materials* 14.23 (2002), pp. 1717–1722. DOI: 10.1002/1521-4095(20021203)14:23<1717::AID-ADMA1717>3.0.CO;2-G. eprint: https://onlinelibrary.wiley.com/doi/pdf/10.1002/1521-4095%2820021203%2914%3A23%3C1717%3A%3AAID-ADMA1717%3E3.0.CO%3B2-G. URL: https://onlinelibrary.wiley.com/doi/abs/10.1002/1521-4095%2820021203%2914%3A23%3C1717%3A%3AAID-ADMA1717%3E3.0.CO%3B2-G.

[52] Jana Zaumseil and Henning Sirringhaus. "Electron and Ambipolar Transport in Organic Field-Effect Transistors". In: *Chemical Reviews* 107.4 (2007). PMID: 17378616, pp. 1296–1323. DOI: 10.1021/cr0501543. eprint: https://doi.org/10.1021/cr0501543. URL: https://doi.org/10.1021/cr0501543.

[53] Sung Ho Kim et al. "Carbon Nanotube and Graphene Hybrid Thin Film for Transparent Electrodes and Field Effect Transistors". In: *Advanced Materials* 26.25 (2014), pp. 4247–4252. DOI: 10.1002/adma.201400463. eprint: https://onlinelibrary.wiley.com/doi/pdf/10.1002/adma.201400463. URL: https://onlinelibrary.wiley.com/doi/abs/10.1002/adma.201400463.

[54] Paul Richman. *Characteristics and Operation of MOS Field-Effect Devices.* McGraw-Hill Book Company, 1967.

[55] Christopher R. Newman et al. "Introduction to Organic Thin Film Transistors and Design of n-Channel Organic Semiconductors". In: *Chemistry of Materials* 16.23 (2004), pp. 4436–4451. DOI: 10.1021/cm049391x. URL: https://doi.org/10.1021/cm049391x.

[56] Gilles Horowitz et al. "The Concept of "Threshold Voltage" in Organic Field-Effect Transistors". In: *Advanced Materials* 10.12 (1998), pp. 923–927. DOI: 10.1002/(SICI)1521-4095(199808)10:12<923::AID-ADMA923>3.0.CO;2-W. URL: https://onlinelibrary.wiley.com/doi/abs/10.1002/

%28SICI%291521-4095%28199808%2910%3A12%3C923%3A%3AAID-ADMA923%3E3.0.CO%3B2-W.

[57] Lay-Lay Chua et al. "High-stability ultrathin spin-on benzocyclobutene gate dielectric for polymer field-effect transistors". In: *Applied Physics Letters* 84.17 (2004), pp. 3400–3402. DOI: 10.1063/1.1710716. eprint: https://doi.org/10.1063/1.1710716. URL: https://doi.org/10.1063/1.1710716.

[58] D. J. Frank et al. "Device scaling limits of Si MOSFETs and their application dependencies". In: *Proceedings of the IEEE* 89.3 (2001), pp. 259–288. ISSN: 0018-9219. DOI: 10.1109/5.915374.

[59] Dieter K. Schroder. *Semicondcutor Material and Device Characterization, second edition*. John Wiley & Sons, Inc, 1998. ISBN: 0-471-24139-3.

[60] Jr. Leonce J. Sevin. *Field-Effect Transistors*. Texas Instruments Inc., 1965. ISBN: 978-0070563551.

[61] T. Minari and C. Liu. "Origin of large contact resistance in organic field-effect transistors". In: *2013 IEEE International Interconnect Technology Conference - IITC* (2013), pp. 1–3. DOI: 10.1109/IITC.2013.6615588.

[62] S. D. Wang, Y. Yan, and K. Tsukagoshi. "Understanding contact behavior in organic thin film transistors". In: *Applied Physics Letters* 97.6 (2010), p. 063307. DOI: 10.1063/1.3479531. URL: https://doi.org/10.1063/1.3479531.

[63] Chuan Liu, Yong Xu, and Yong-Young Noh. "Contact engineering in organic field-effect transistors". In: *Materials Today* 18.2 (2015), pp. 79–96. ISSN: 1369-7021. DOI: https://doi.org/10.1016/j.mattod.2014.08.037. URL: http://www.sciencedirect.com/science/article/pii/S1369702114003204.

[64] C. H. Kim, Y. Bonnassieux, and G. Horowitz. "Charge Distribution and Contact Resistance Model for Coplanar Organic Field-Effect Transistors". In: *IEEE Transactions on Electron Devices* 60.1 (2013), pp. 280–287. ISSN: 0018-9383. DOI: 10.1109/TED.2012.2226887.

[65] Chang-Hyun Kim et al. "Potentiometric Parameterization of Dinaphtho[2,3-b:2',3'-f]thieno[3,2-b]thiophene Field-Effect Transistors with a Varying Degree of Nonidealities". In: *Advanced Electronic Materials* 4.7 (2018), p. 1700514. DOI: 10.1002/aelm.201700514. eprint: https://onlinelibrary.wiley.com/doi/pdf/10.1002/aelm.201700514. URL: https://onlinelibrary.wiley.com/doi/abs/10.1002/aelm.201700514.

[66] R. H. Pain. *Mechanisms of Protein Folding*. Oxford University Press, 1994. ISBN: 0-19-963396-7.

[67] Max Perutz. *Protein Structure: new approaches to disease and therapy*. New York: Freeman & Co., 1994. ISBN: 0-7167-7022-9.

[68] A. M. Lesk. *Protein Architecture: A Practical Approach*. Oxford University Press, 1991. ISBN: 0-19-963054-2.

[69] Gregory A Petsko and Dagmar Ringe. *Protein Structure and Function*. Oxford University Press, 2009. ISBN: 978-0-19-955684-7.

[70] Nicholas C. Price and Jacqueline Nairn. *Exploring Proteins*. Oxford University Press, 2009. ISBN: 978-0-19-920570-7.

[71] Roger Y. Tsien. "The Green Fluorescent Protein". In: *Annual Review of Biochemistry* 67.1 (1998). PMID: 9759496, pp. 509–544. DOI: 10.1146/annurev.biochem.67.1.509. eprint: https://doi.org/10.1146/annurev.biochem.67.1.509. URL: https://doi.org/10.1146/annurev.biochem.67.1.509.

[72] Osamu Shimomura, Frank H. Johnson, and Yo Saiga. "Extraction, Purification and Properties of Aequorin, a Bioluminescent Protein from the Luminous Hydromedusan, Aequorea". In: *Journal of Cellular and Comparative Physiology* 59.3 (1962), pp. 223–239. DOI: 10.1002/jcp.1030590302. eprint: https://onlinelibrary.wiley.com/doi/pdf/10.1002/jcp.1030590302. URL: https://onlinelibrary.wiley.com/doi/abs/10.1002/jcp.1030590302.

[73] Jean-Denis. Pédelac et al. "Engineering and characterization of a superfolder green fluorescent protein". In: *Nature Biotechnology* 24 (2006), pp. 79–88. DOI: 10.1038/nbt1172. URL: https://doi.org/10.1038/nbt1172.

[74] Fabio Arnesano et al. “The Solution Structure of Oxidized Escherichia coli Cytochrome b562,” in: *Biochemistry* 38.27 (1999). PMID: 10393541, pp. 8657–8670. DOI: 10.1021/bi982785f. eprint: https://doi.org/10.1021/bi982785f. URL: https://doi.org/10.1021/bi982785f.

[75] Kesaku. Hamada, Paul H. Bethge, and Scott F. Mathews. “Refined Structure of Cytochromeb_{562} from Escherichia coli at 1.4ÅResolution”. In: *J. Mol. Biol.* 247.5 (1995), pp. 947–962. DOI: https://doi.org/10.1006/jmbi.1995.0192. URL: http://www.sciencedirect.com/science/article/pii/S0022283685701921.

[76] Maghar S. Manhas and Ajay K. Bose. *beta-LACTAMS: Natural and Synthetic*. John Wiley & Sons, 1971. ISBN: 0-471-56700-0.

[77] Nicholas G. Brown, Dar-Chone Chow, and Timothy Palzkill. “BLIP-II Is a Highly Potent Inhibitor of Klebsiella pneumoniae Carbapenemase (KPC-2)”. In: 57.7 (2013), pp. 3398–3401. DOI: 10.1128/AAC.00215-13.

[78] J L Doran et al. “Isolation and characterization of a beta-lactamase-inhibitory protein from Streptomyces clavuligerus and cloning and analysis of the corresponding gene.” In: *Journal of bacteriology : JB.* 172.9 (), pp. 4909–4918. ISSN: 0021-9193.

[79] D Lim et al. “Crystal structure and kinetic analysis of beta-lactamase inhibitor protein-II in complex with TEM-1 beta-lactamase.” In: *Nature structural biology.* 8.10 (2001), pp. 848–852. ISSN: 1072-8368.

[80] Michael Gretes et al. “Insights into positive and negative requirements for protein-protein interactions by crystallographic analysis of the beta-lactamase inhibitory proteins BLIP, BLIP-I, and BLP.” In: *Journal of molecular biology.* 389.2 (), pp. 289–305. ISSN: 0022-2836.

[81] Nicholas G Brown et al. “Analysis of the binding forces driving the tight interactions between beta-lactamase inhibitory protein-II (BLIP-II) and class A beta-lactamases.” In: *Journal of biological chemistry.* 286.37 (), pp. 32723–32735. ISSN: 0021-9258.

[82] N G Brown and T Palzkill. "Identification and characterization of beta-lactamase inhibitor protein-II (BLIP-II) interactions with beta-lactamases using phage display." In: *Protein engineering, design and selection : PEDS.* 23.6 (), pp. 469–478. ISSN: 1741-0126.

[83] N G Brown et al. "Identification of the β-Lactamase Inhibitor Protein-II (BLIP-II) Interface Residues Essential for Binding Affinity and Specificity for Class A β-Lactamases". In: *The Journal of Biological Chemistry* 288 (24 2013), pp. 17156–17166. DOI: 10.1074/jbc.M113.463521. URL: http://www.jbc.org/content/288/24/17156.full.

[84] Athraa J. Zaki et al. "Defined covalent assembly of protein molecules on graphene using a genetically encoded photochemical reaction handle". In: *RSC Adv.* 8 (11 2018), pp. 5768–5775. DOI: 10.1039/C7RA11166E. URL: http://dx.doi.org/10.1039/C7RA11166E.

[85] Jin Han and Chao Gao. "Functionalization of carbon nanotubes and other nanocarbons by azide chemistry". In: *Nano-Micro Letters* 2.3 (2010), pp. 213–226.

[86] Jaehyeung Park and Mingdi Yan. "Covalent Functionalization of Graphene with Reactive Intermediates". In: *Accounts of Chemical Research* 46.1 (2013), pp. 181–189. DOI: 10.1021/ar300172h. eprint: https://doi.org/10.1021/ar300172h. URL: https://doi.org/10.1021/ar300172h.

[87] Vasilios Georgakilas et al. "Functionalization of Graphene: Covalent and Non-Covalent Approaches, Derivatives and Applications". In: *Chemical Reviews* 112.11 (2012), pp. 6156–6214. DOI: 10.1021/cr3000412. eprint: https://doi.org/10.1021/cr3000412. URL: https://doi.org/10.1021/cr3000412.

[88] Andrew M. Hartley. "Using a reprogrammed genetic code code to modulate protein activity by novel post-translational control". PhD thesis. Cardiff University, 2014.

[89] L. C. F. Blackman and Alfred Rene Jean Paul Ubbelohde. "Stress recrystallization of graphite". In: *Proceedings of the Royal Society of London. Series A. Mathematical and Physical Sciences* 266.1324 (1962), pp. 20–32. DOI:

10.1098/rspa.1962.0044. URL: https://royalsocietypublishing.org/doi/abs/10.1098/rspa.1962.0044.

[90] Advanced Integrated Scanning Tools for Nanotechnology. *HOPG*. URL: http://nanoprobes.aist-nt.com/apps/HOPG%5C%20info.htm (visited on 02/12/2019).

[91] K. S. Novoselov et al. "Electric Field Effect in Atomically Thin Carbon Films". In: 306.5696 (2004), pp. 666–669. DOI: 10.1126/science.1102896. URL: http://science.sciencemag.org/content/306/5696/666.

[92] A. H. Castro Neto et al. "The electronic properties of graphene". In: *Rev. Mod. Phys.* 81 (1 2009), pp. 109–162. DOI: 10.1103/RevModPhys.81.109. URL: https://link.aps.org/doi/10.1103/RevModPhys.81.109.

[93] Wendler Florian, Knorr Andreas, and Malic Ermin. "Ultrafast carrier dynamics in Landau-quantized graphene". In: *Nanophotonics* 4.3 (2015), pp. 224–249. ISSN: 2192-8614. DOI: doi:10.1515/nanoph-2015-0018. URL: https://www.ingentaconnect.com/content/doaj/21928614/2015/00000004/00000003/art00001.

[94] Khalid Saeed Ibrahim. "Carbon nanotubes-properties and applications: a review". In: *Carbon letters* 3.3 (2013). DOI: 10.5714/CL.2013.14.3.131. URL: http://dx.doi.org/10.5714/CL.2013.14.3.131.

[95] N. Saifuddin, A. Z. Raziah, and A. R. Junizah. "Carbon Nanotubes: A Review on Structure and Their Interaction with Proteins". In: *Journal of Chemistry* 2013 (2013). DOI: 10.1155/2013/676815. URL: http://dx.doi.org/10.1155/2013/676815.

[96] Peng Lin and Feng Yan. "Organic Thin-Film Transistors for Chemical and Biological Sensing". In: *Advanced Materials* 24.1 (2012), pp. 34–51. DOI: 10.1002/adma.201103334. eprint: https://onlinelibrary.wiley.com/doi/pdf/10.1002/adma.201103334. URL: https://onlinelibrary.wiley.com/doi/abs/10.1002/adma.201103334.

[97] Jeffrey T. Mabeck and George G. Malliaras. "Chemical and biological sensors based on organic thin-film transistors". In: *Analytical and Bioanalytical Chemistry* 384.2 (2006), pp. 343–353. ISSN: 1618-2650. DOI: 10.1007/

s00216-005-3390-2. URL: https://doi.org/10.1007/s00216-005-3390-2.

[98] Luisa Torsi et al. "Organic field-effect transistor sensors: a tutorial review". In: *Chem. Soc. Rev.* 42 (22 2013), pp. 8612–8628. DOI: 10.1039/C3CS60127G. URL: http://dx.doi.org/10.1039/C3CS60127G.

[99] Ting Lei et al. "High-Performance Air-Stable Organic Field-Effect Transistors: Isoindigo-Based Conjugated Polymers". In: *Journal of the American Chemical Society* 133.16 (2011). PMID: 21466199, pp. 6099–6101. DOI: 10.1021/ja111066r. eprint: https://doi.org/10.1021/ja111066r. URL: https://doi.org/10.1021/ja111066r.

[100] H. E. Katz et al. "A soluble and air-stable organic semiconductor with high electron mobility". In: *Nature* 404 (2000), pp. 478–481. DOI: 10.1038/35006603. URL: https://doi.org/10.1038/35006603.

[101] Antonio Facchetti. "Ï€-Conjugated Polymers for Organic Electronics and Photovoltaic Cell Applications". In: *Chemistry of Materials* 23.3 (2011), pp. 733–758. DOI: 10.1021/cm102419z. eprint: https://doi.org/10.1021/cm102419z. URL: https://doi.org/10.1021/cm102419z.

[102] Beng S. Ong et al. "High-Performance Semiconducting Polythiophenes for Organic Thin-Film Transistors". In: *Journal of the American Chemical Society* 126.11 (2004). PMID: 15025437, pp. 3378–3379. DOI: 10.1021/ja039772w. eprint: https://doi.org/10.1021/ja039772w. URL: https://doi.org/10.1021/ja039772w.

[103] Lay-Lay Chua et al. "General observation of n-type field-effect behaviour in organic semiconductors". In: *Nature* 434 (2005), pp. 194–199. DOI: 10.1038/nature03376. URL: https://doi.org/10.1038/nature03376.

[104] Iain McCulloch et al. "Semiconducting Thienothiophene Copolymers: Design, Synthesis, Morphology, and Performance in Thin-Film Organic Transistors". In: *Advanced Materials* 21 (2009), pp. 1091–1109. DOI: 10.1002/adma.200801650. eprint: https://onlinelibrary.wiley.com/doi/pdf/10.1002/adma.200801650. URL: https://onlinelibrary.wiley.com/doi/abs/10.1002/adma.200801650.

[105] T. J. Richards and H. Sirringhaus. "Analysis of the contact resistance in staggered, top-gate organic field effect transistors". In: *Journal of Applied Physics* 102.9 (2007), p. 094510. DOI: 10.1063/1.28042288. eprint: https://doi.org/10.1063/1.2804288. URL: https://doi.org/10.1063/1.2804288.

[106] C. H. Kim, Y. Bonnassieux, and G. Horowitz. "Fundamental Benefits of the Staggered Geometry for Organic Field-Effect Transistors". In: *IEEE Electron Device Letters* 32.9 (2011), pp. 1302–1304. ISSN: 0741-3106. DOI: 10.1109/LED.2011.2160249.

[107] Howard E. Katz. "Recent Advances in Semiconductor Performance and Printing Processes for Organic Transistor-Based Electronics". In: *Chemistry of Materials* 16.23 (2004), pp. 4748–4756. DOI: 10.1021/cm049781j. URL: https://doi.org/10.1021/cm049781j.

[108] Kanan P. Puntambekar, Paul V. Pesavento, and C. Daniel Frisbie. "Surface potential profiling and contact resistance measurements on operating pentacene thin-film transistors by Kelvin probe force microscopy". In: *Applied Physics Letters* 83.26 (2003), pp. 5539–5541. DOI: 10.1063/1.1637443. URL: https://doi.org/10.1063/1.1637443.

[109] Ute Zschieschang et al. "Dinaptho[2,3-b:2',3'-f]thieno[3,2-b]thiophene (DNTT) thin-film transistors with improved performance and stability". In: *Organic Electronics* 12 (8 2011), pp. 1370–1375. DOI: https://doi.org/10.1016/j.orgel.2011.04.018. URL: http://www.sciencedirect.com/science/article/pii/S1566119911001583.

[110] Yun-Shiuan Li et al. "Single-layer organic-inorganic-hybrid thin-film encapsulation for organic solar cells". In: *Journal of Physics D: Applied Physics* 46 (43 2013), p. 435502. DOI: doi:10.1088/0022-3727/46/43/435502. URL: http://stacks.iop.org/0022-3727/46/i=43/a=435502.

[111] C. Kim, Y. Bonnassieux, and G. Horowitz. "Compact DC Modeling of Organic Field-Effect Transistors: Review and Perspectives". In: *IEEE Transactions on Electron Devices* 61.2 (2014), pp. 278–287. ISSN: 1557-9646. DOI: 10.1109/TED.2013.2281054.

[112] Zachary A. Lamport et al. “Tutorial: Organic field-effect transistors: Materials, structure and operation”. In: *Journal of Applied Physics* 124.7 (2018), p. 071101. DOI: 10.1063/1.5042255. URL: https://doi.org/10.1063/1.5042255.

[113] Francesco Musumeci and Gerald H Pollack. “Influence of water on the work function of certain metals.” In: *Chemical physics letters* 536 (2012), pp. 65–67. DOI: 10.1016/j.cplett.2012.03.094.

[114] Chunzeng Li. *probe questions for EFM/KPFM*. URL: http://nanoscaleworld.bruker-axs.com/nanoscaleworld/forums/t/430.aspx.

[115] W.M.H. Sachtler, G.J.H. Dorgelo, and A.A. Holscher. “The work function of gold”. In: *Surface Science* 5.2 (1966), pp. 221–229. DOI: https://doi.org/10.1016/0039-6028(66)90083-5. URL: http://www.sciencedirect.com/science/article/pii/0039602866900835.

[116] Paul A. Anderson. “Work Function of Gold”. In: *Phys. Rev.* 115 (3 1959), pp. 553–554. DOI: 10.1103/PhysRev.115.553. URL: https://link.aps.org/doi/10.1103/PhysRev.115.553.

[117] Robert Hofmockel et al. “High-mobility organic thin-film transistors based on a small-molecule semiconductor deposited in vacuum and by solution shearing”. In: *Organic Electronics* 14.12 (2013), pp. 3213–3221. ISSN: 1566-1199. DOI: https://doi.org/10.1016/j.orgel.2013.09.003. URL: http://www.sciencedirect.com/science/article/pii/S1566119913003923.

[118] Sigma Aldrich. *Organic Field Effect Transistors Based on DNTT and Related Organic Semiconductors*. URL: https://www.sigmaaldrich.com/materials-science/organic-electronics/dntt-based-organic-semiconductors.html.

[119] Do Kyung Hwang et al. “Solvent and polymer matrix effects on TIPS-pentacene/polymer blend organic field-effect transistors”. In: *J. Mater. Chem.* 22.12 (2012), pp. 5531–5537. DOI: 10.1039/C2JM16487F. URL: http://dx.doi.org/10.1039/C2JM16487F.

[120] C.D. Dimitrakopoulos and P.R.L. Malenfant. "Organic Thin Film Transistors for Large Area Electronics". In: *Advanced Materials* 14.2 (2002), pp. 99–117. DOI: 10.1002/1521-4095(20020116)14:2<99::AID-ADMA99>3.0.CO;2-9. URL: https://onlinelibrary.wiley.com/doi/abs/10.1002/1521-4095%5C%2820020116%5C%2914%5C%3A2%5C%3C99%5C%3A%5C%3AAID-ADMA99%5C%3E3.0.CO%5C%3B2-9.

[121] Sankar Subramanian et al. "Chromophore Fluorination Enhances Crystallization and Stability of Soluble Anthradithiophene Semiconductors". In: *Journal of the American Chemical Society* 130.9 (2008), pp. 2706–2707. DOI: 10.1021/ja073235k. eprint: https://doi.org/10.1021/ja073235k. URL: https://doi.org/10.1021/ja073235k.

[122] Aaron B. Naden, Joachim Loos, and Donald A. MacLaren. "Structure-function relations in diF-TES-ADT blend organic field effect transistors studied by scanning probe microscopy". In: *J. Mater. Chem. C* 2.2 (2014), pp. 245–255. DOI: 10.1039/C3TC31783H. URL: http://dx.doi.org/10.1039/C3TC31783H.

[123] Richard Hamilton et al. "High-Performance Polymer-Small Molecule Blend Organic Transistors". In: *Advanced Materials* 21.10-11 (2009), pp. 1166–1171. DOI: 10.1002/adma.200801725. eprint: https://onlinelibrary.wiley.com/doi/pdf/10.1002/adma.200801725. URL: https://onlinelibrary.wiley.com/doi/abs/10.1002/adma.200801725.

[124] *dif-TES ADT molecule: Molecular composition from Sigma Aldrich*. https://www.sigmaaldrich.com/catalog/product/aldrich/754099.

[125] *PTAA: Molecular composition from Sigma Aldrich*. https://www.sigmaaldrich.com/catalog/product/aldrich/702471.

[126] Alexandra F. Paterson et al. "Small Molecule/Polymer Blend Organic Transistors with Hole Mobility Exceeding 13 cm2 V-1 s-1". In: *Advanced Materials* 28.35 (2016), pp. 7791–7798. DOI: 10.1002/adma.201601075. eprint: https://onlinelibrary.wiley.com/doi/pdf/10.1002/adma.201601075. URL: https://onlinelibrary.wiley.com/doi/abs/10.1002/adma.201601075.

[127] Xinran Zhang et al. “Molecular origin of high field-effect mobility in an indiacenodithiophene-benzothiadiazole copolymer”. In: *Nature Communications* 4 (2238 2013), pp. 1–9. DOI: 10.1038/ncomms3238. URL: https://doi.org/10.1038/ncomms3238.

[128] Stuart G. Higgins et al. “Indacenodithiophene–benzothiadiazole organic field-effect transistors with gravure-printed semiconductor and dielectric on plastic”. In: *MRS Communications* 5.4 (2015), pp. 599–603. DOI: 10.1557/mrc.2015.66.

[129] *C_8-BTBT: Molecular composition from Sigma Aldrich.* https://www.sigmaaldrich.com/catalog/product/aldrich/747092.

[130] Julianna Panidi et al. “Remarkable Enhancement of the Hole Mobility in Several Organic Small-Molecules, Polymers, and Small-Molecule:Polymer Blend Transistors by Simple Admixing of the Lewis Acid p-Dopant B(C6F5)3”. In: *Advanced Science* 5.1 (2018), p. 1700290. DOI: 10.1002/advs.201700290. URL: https://onlinelibrary.wiley.com/doi/abs/10.1002/advs.201700290.

[131] Jeremy Smith et al. “Solution-processed organic transistors based on semiconducting blends”. In: *J. Mater. Chem.* 20.13 (2010), pp. 2562–2574. DOI: 10.1039/B921674J. URL: http://dx.doi.org/10.1039/B921674J.

[132] Jeremy Smith et al. “Solution-Processed Small Molecule-Polymer Blend Organic Thin-Film Transistors with Hole Mobility Greater than 5 cm2/Vs”. In: *Advanced Materials* 24.18 (2012), pp. 2441–2446. DOI: 10.1002/adma.201200088. URL: https://onlinelibrary.wiley.com/doi/abs/10.1002/adma.201200088.

[133] Simon Hunter and Thomas D. Anthopoulos. “Observation of Unusual, Highly Conductive Grain Boundaries in High-Mobility Phase Separated Organic Semiconducting Blend Films Probed by Lateral-Transport Conductive-AFM”. In: *Advanced Materials* 25.31 (2013), pp. 4320–4326. DOI: 10.1002/adma.201300020. URL: https://onlinelibrary.wiley.com/doi/abs/10.1002/adma.201300020.

[134] *Tris(pentafluorophenyl)borane (BCF): Molecular composition from Sigma Aldrich.* https://www.sigmaaldrich.com/catalog/product/aldrich/442593.

[135] Travis E. Oliphant. *Guide to NumPy*. USA: CreateSpace Independent Publishing Platform, 2015. ISBN: 9781517300074.

[136] H. G Ong and J Wang. *Physical and Chemical Properties of Carbon Nanotubes*. IntechOpen, 2013. ISBN: 978-953-51-1002-6. DOI: 10.5772/46029.

[137] Thierry Mélin, Mariusz Zdrojek, and David Brunel. *Electrostatic Force Microscopy and Kelvin Force Microscopy as a Probe of the Electrostatic and Electronic Properties of Carbon Nanotubes*. Springer Berlin Heidelberg, 2010. ISBN: 978-3-642-03534-0. DOI: 10.1007/978-3-642-03535-7_4.

[138] Thomas Sand Jespersen and Jesper Nygård. "Charge Trapping in Carbon Nanotube Loops Demonstrated by Electrostatic Force Microscopy". In: *Nano Letters* 5.9 (2005), pp. 1838–1841. DOI: 10.1021/nl0505997. eprint: https://doi.org/10.1021/nl0505997. URL: https://doi.org/10.1021/nl0505997.

[139] C. Gómez-Navarro et al. "Contactless experiments on individual DNA molecules show no evidence or molecular wire behavior". In: *Proceedings of the National Academy of Sciences* 99.13 (2002), pp. 8484–8487. ISSN: 0027-8424. DOI: 10.1073/pnas.122610899. eprint: https://www.pnas.org/content/99/13/8484.full.pdf. URL: https://www.pnas.org/content/99/13/8484.

[140] S Gómez-Moñivas et al. "Tip-shape effects on electrostatic force microscopy resolution". In: *Nanotechnology* 12.4 (2001), pp. 496–499. DOI: 10.1088/0957-4484/12/4/323. URL: https://doi.org/10.1088%2F0957-4484%2F12%2F4%2F323.

[141] Isam Abdullah. "Nanoscale Properties of Molecular and Oxide Based Thin Film Devices Measured by SPM". PhD thesis. Cardiff University, 2016.

[142] John David Jackson. *Classical Electrodynamics*. John Wiley & sons, Inc., 1962. ISBN: 0-471-43131-1.

[143] Ricardo Garćia and Rubén Pérez. "Dynamic atomic force microscopy methods". In: *Surface Science Reports* 47.6 (2002), pp. 197–301. ISSN: 0167-5729. DOI: https://doi.org/10.1016/S0167-5729(02)00077-8. URL: http://www.sciencedirect.com/science/article/pii/S0167572902000778.

[144] X.H. Qiu et al. "Electrostatic characteristics of nanostructures investigated using electric force microscopy". In: *Journal of Solid State Chemistry* 181.7 (2008), pp. 1670–1677. ISSN: 0022-4596. DOI: https://doi.org/10.1016/j.jssc.2008.06.036. URL: http://www.sciencedirect.com/science/article/pii/S0022459608003344.

[145] *Dimension 3100 Manual: NanoScope Software Version 5.* 2004.

[146] Athraa Zaki. "Conductivity studies of single protein molecules". PhD thesis. Cardiff University, 2016.

[147] Krzysztof Gajewski et al. "Microscale surface potential gradient disturbances observed in bilayer graphene". In: *Applied Surface Science* 510 (2020), p. 145504. ISSN: 0169-4332. DOI: https://doi.org/10.1016/j.apsusc.2020.145504. URL: http://www.sciencedirect.com/science/article/pii/S0169433220302609.

[148] Tim Burnett, Rositza Yakimova, and Olga Kazakova. "Mapping of Local Electrical Properties in Epitaxial Graphene Using Electrostatic Force Microscopy". In: *Nano Letters* 11.6 (2011), pp. 2324–2328. DOI: 10.1021/nl200581g. eprint: https://doi.org/10.1021/nl200581g. URL: https://doi.org/10.1021/nl200581g.

[149] Adam Beachey. "Electron transfer in protein-carbon nanotube hybrid structures". PhD thesis. Cardiff University, 2018.

[150] A.T. Winzer et al. "Correcting for AFM tip induced topography convolutions in protein–DNA samples". In: *Ultramicroscopy* 121 (2012), pp. 8–15. DOI: https://doi.org/10.1016/j.ultramic.2012.07.002. URL: http://www.sciencedirect.com/science/article/pii/S0304399112001726.

[151] Xinzhao Xu et al. "Reconfigurable Carbon Nanotube Multiplexed Sensing Devices". In: *Nano Letters* 18.7 (2018), pp. 4130–4135. DOI: 10.1021/acs.

nanolett.8b00856. URL: https://doi.org/10.1021/acs.nanolett.8b00856.